# A Numerical and Climatological Investigation of Deep Convective Cloud Patterns in South Florida

Jeffery T. McQueen and Roger A. Pielke


Atmospheric Science
PAPER NO.
389

US ISSN 0067-0340

DEPARTMENT OF ATMOSPHERIC SCIENCE
COLORADO STATE UNIVERSITY
FORT COLLINS, COLORADO

# A NUMERICAL AND CLIMATOLOGICAL INVESTIGATION OF DEEP CONVECTIVE CLOUD PATTERNS IN SOUTH FLORIDA

by

Jeffery T. McQueen
and
Roger A. Pielke

Research supported by the
National Aeronautics and Space Administration
under grant
NAG 5-359

Department of Atmospheric Science
Colorado State University
Fort Collins, Colorado 80523

July 1985

Atmospheric Science Paper No. 389

ABSTRACT

Climatological characteristics of thunderstorm activity over South Florida are presented by processing and compositing digital visible and infrared satellite imagery collected during the summer of 1983. To describe the physical processes associated with the occurrence and patterning of the satellite observed deep convection, averaged quantitites of numerous synoptic variables were calculated for days which made up the satellite composites. A three-dimensional mesoscale model is also utilized to investigate the physical processes associated with the deep convection patterns over South Florida. The model incorporates the interaction between the sea breeze forcings and the synoptic flow as well as the effects of variations in the ground surface characteristics.

The satellite composite results demonstrated that the deep cumulonimbus activity over South Florida on synoptically undisturbed days during the summer is strongly focused in specific geographic regions of the peninsula. Moisture availability on the synoptic scale was found to be the most important control on the percentage of afternoon deep convective cloud activity. Also, strongly correlated with the amount of afternoon deep convective cloudiness over the peninsula was the morning (0800 EST) deep cumulus activity over water.

The specific locations of thunderstorm activity were mainly found near maximums in sea breeze and local scale convergence of low-level moisture and wind. The patterns of these sea breeze fields are controlled by the different types of ground surface, and by the speed and direction of the synoptic flow.

## ACKNOWLEDGMENTS

The suggestions of Richard H. Johnson and Douglas Fox, members of the first author's M.S. Committee, are greatly appreciated. Mr. John Weaver, Mr. Robert Green and Mrs. Marjorie Klitch are thanked for showing how to create satellite image composites.

Dr. Robert Kessler, Mordecay Segal, Ray Arritt and Jenn-Luen Song assisted with the numerical model and their support is appreciated. Dave Randall's help with the ground station computing and drafting facilities is gratefully acknowledged. The National Weather Service Office at Camp Springs, Maryland, and Ruskin AFB are thanked for providing hard copy satellite imagery.

Drafting was skillfully prepared by Judie Sorbie. Liz Lambert painstakingly typed the draft. The editorial preparation of this work was very capably managed by Sara Rumley.

The numerical model was run using the CYBER 205 computer which was supported by the Institute for Computational Studies at Colorado State University.

This research was sponsored by the National Aeronautics and Space Administration, Grant NAG 5-359.

TABLE OF CONTENTS

LIST OF TABLES

LIST OF FIGURES

# CHAPTER 1

# INTRODUCTION

The manner in which synoptic and mesoscale forcings interact with convection is being recognized as an area which is still only partially understood. South Florida is an excellent laboratory to study this problem since the mesoscale and synoptic scale forcings are usually similar throughout the summer and cumulus convection is widespread. Cooper et al. (1982) have postulated that the main physical processes which lead to thunderstorms over the South Florida peninsula are:

1) The synoptic setting including the synoptic flow and thermodynamic structure.
2) The peninsula scale forcing represented by the sea breeze and outflow from Lake Okeechobee.
3) The localized mesoscale forcings in the peninsula convergence zones.
4) Convective scale convergence caused by convective outflow.

In South Florida, Cunning et al. (1982) also noted that the interactions between developing convection and the boundary layer induce or maintain cumulus scale processes. On the local scale, Gannon (1978) and McCumber (1980) have shown the importance of vegetation and soil type in creating surface heat and moisture fluxes favorable for convective development.

This study will evaluate the importance of these physical processes in contributing to the thunderstorm activity over South Florida. In order to do this, a climatology of the deep convective cloud patterns for different low level synoptic flow categories will be presented through the use of satellite image composites. Also results from a three-dimensional numerical mesoscale model will be presented. The numerical model physics incorporates a parameterization of vegetation and soil type feedbacks as well as a sophisticated planetary boundary layer representation. Therefore, by comparing the model results to the satellite composites, an estimate of the importance of the sea breeze and ground surface forcing in controlling the spatial and temporal variations in thunderstorm activity can be given. A correlation of large-scale thermodynamic and dynamic variables with convective cloud activity will also be accomplished. Complementary use of all these results will help determine some of the important scale interactions which force the observed patterns in convective activity.

Byers and Rodebush (1948) were among the first to call attention to a relationship between sea breeze and convective patterns over Florida. Day (1953) and Gentry and Moore (1954) noted the importance of the synoptic flow interacting with the sea breeze to create areas of convergence.

Frank et al. (1967) completed the first radar-derived climatology over Florida. They stratified the radar data by 5000 ft. winds. Data were categorized into five wind categories which were north, east, south, and west winds greater than 6 kts, and light and variable winds less than 6 kts. Results showed that the spatial and temporal

variations of the radar patterns were strongly dependent on the synoptic flow and the sea breeze convergence. In their climatologies, however, the intensity of the radar signal was not included. Smith (1970) also used radar data to create a climatology stratified by the winds at Appalachicola, Florida. His results showed the importance of the concave and convex curved coastlines on radar echo activity.

Blanchard and Lopez (1984) completed a climatology of convection over South Florida using Miami radar data collected during three summers. Their work incorporated radar echo intensity information into the final composite results. Data were categorized by similarities in radar echo patterns rather than by the low-level synoptic flow. Four basic convective pattern types were observed from their data which were found to be controlled to a large degree by the synoptic flow which was in turn controlled by the position of the Atlantic high pressure ridge.

Maier et al. (1984) used data from lightning direction finder stations located in southern Florida. With this data, the diurnal variations in lightning activity at different parts of the peninsula were observed. The data were not stratified into a synoptic categorization while creating the composites. The results showed good agreement between lightning frequency and rainfall amount with the highest amounts over land occurring between 1400 and 1700 EST.

Much statistical work was also accomplished in which certain large-scale variables were correlated with some measure of convective activity. Frank and Smith (1968) correlated the afternoon percent radar echo coverage with certain large-scale variables obtained from the morning soundings and synoptic maps over Florida. The only

significantly correlated parameter at the 0.05 level was mid-tropospheric relative humidity.

Burpee (1979) found little correlation between late morning divergence on the peninsula scale and area averaged rainfall. He found, rather, that the magnitude and timing of the convective response to the sea breeze forcing during the afternoon was very sensitive to the moisture amount and somewhat sensitive to the thermal stability.

Lopez et al. (1984), while looking at individual radar echoes during days which were neither synoptically disturbed nor suppressed, found that as the wind speed decreased and the wind direction became more southerly, the convective activity during the day increased.

These results were supported by Burpee and Lahiff (1984) while comparing the area averaged rainfall variations with large-scale winds on synoptically undisturbed days. These authors also found low and mid tropospheric relative humidity to be the best correlated atmospheric parameter with rainfall.

Numerical modelling studies have been done extensively since the early 1970's to simulate sea breeze convergence and convective cloud patterns over Florida. Pielke (1974) utilized a dry, hydrostatic mesoscale model to study the sea breeze circulation over South Florida. He concluded that on synoptically undisturbed days, the sea breeze convergence zones were the primary control on the general location of the cloud patterns. The position of the sea breeze was in turn controlled by the synoptic flow. The importance of Lake Okeechobee in producing a lake breeze circulation which interacted with the sea breeze was also noted from the model results.

Cotton et al. (1976) used a three-dimensional dry mesoscale sea breeze model to obtain sea breeze perturbed soundings which were used to initialize a one-dimensional cloud model. The sea breeze was found to warm the lower and middle troposphere, develop a shallow super-adiabatic layer near the surface, and moisten the lower troposphere. This perturbed sounding initialized a one-dimensional cloud model and gave a favorable environment for cumulus clouds. The mesoscale model also predicted a higher planetary boundary layer height, large surface fluxes of momentum, heat and moisture, changes in the vertical shear of the horizontal wind in low levels, and an intense, horizontal convergence region of heat, moisture, momentum and cloud material. These later alterations to the synoptic scale by the sea breeze would likely have dramatic effects on convective initiation but quantitative conclusions could not be made with the one-dimensional cloud model.

Pielke and Mahrer (1978), utilizing the Pielke model with the additions of a surface energy budget and radiation parameterization, showed that some of the model predicted mesoscale convergence regions were not covered by precipitating clouds. This indicated that there were other controls on the convection besides the sea breeze forcing. Gannon (1978) and McCumber (1980) modified Pielke's model to include the effect on the sea breeze of the soil and vegetation in Florida and the variation of incoming solar radiation due to clouds. They found all these factors to be important in determining the location and intensity of the model predicted sea breeze convergence zones.

Utilizing a sophisticated three-dimensional cloud model, Tripoli and Cotton (1980) ran experiments to explore some of the factors which accounted for the variations of intensity of individual deep

convective clouds over Florida. The authors concluded that the storm kinetic energy evolves to a magnitude that is primarily controlled by the magnitude of the mesoscale convergence. This implied that the intensity of deep precipitating convection is mainly due to the amount of moist static energy supplied to the storm by mesoscale convergence.

While some of the modeling studies have shown that deep convecton is related to the intensity of the mesoscale convergence zones, Cooper et al. (1982) revealed that deep convection later in the day cannot be fully supported by the sea breeze convergence. They showed that the peninsula scale forcing decreased rapidly after 1330 EST as the importance of the convective upward transports continued to increase past 1500. They explained this result to the increasing role convective scale convergence has as more convective storms develop in the afternoon. A case study of a cloud merger over Florida by Cunning et al. (1982) illustrated how outflow from thunderstorms interacts to produce an enhanced band of strong convergence and new convection.

The current study reported in this report utilizes a satellite image climatology, a three-dimensional mesoscale numerical model and results from a regression analysis to describe the convective cloud patterns over South Florida and to determine the importance of scale interactions in forcing the observed patterns. This is the first attempt to complete a satellite climatology over this study area. The satellite data used provides high spatial and temporal resolution of cloudiness. By processing the satellite images it is also possible to isolate the patterns of one particular cloud type (in this study, deep convective clouds) and eliminate other cloud types (low clouds and

cirrus). The composites will also be stratified by more synoptic flow categories than were used in previous climatologies.

Previously, the results from numerical models were compared to only case study observations. This report will give the results of the model comparisons with the satellite image composites. Therefore, the importance of the sea breeze forcings on convective cloud patterns over south Florida on a climatological basis can be implied.

The goals of this study can be summarized as follows:

- To describe and define the important large-scale controls on the development and intensity of convective clouds. This will be done through a regressional analysis.
- To evaluate the importance of the synoptic flow on controlling the large-scale thermodynamic environment over South Florida.
- To describe the convective cloud patterns exhibited in the satellite image composites for each synoptic flow category and also to indicate areas of preferred convective activity.
- To estimate the climatologically expected contributions to the cumulus cloud convection as a result of the sea breeze and local scale forcings due to ground surface variations. This will be determined by evaluating the extent of agreement between the numerical model results and the cloud climatology.
- To determine the usefulness of combining the results of a dry, hydrostatic mesoscale model and a cloud climatology for applications in day-to-day forecasting of convection during the summer over South Florida.

Chapter 2 outlines the procedures used to process the data. Chapter 3 describes the mesoscale model used and gives the data to

initialize the model for each synoptic flow class. Chapter 4 contains the description of the large-scale evironment for each synoptic category and also highlights the results of the regression analysis. The cloud climatology and model results are given in Chapter 5. Chapter 6 summarizes the major conclusions and discusses the implications for using the results of this study as a guide to daily forecasting.

# CHAPTER 2

# DATA DESCRIPTION AND PROCESSING

## 2.1 The Satellite Data

The satellite data used to make the composite images were collected from the east Geostationary Operational Environmental Satellite (GOES) by the Colorado State University, Department of Atmospheric Science's Direct Readout Satellite Earth Station (DRSES). The data were received and stored on magnetic tape in digital form for 39 days during the summer of 1983 (June 1-August 31) for a broad rectangular area of the eastern United States from Connecticut to just south of Florida. Figure 2.1 shows the areal coverage of the raw data.

Data were collected for days which were forecast that morning to be synoptically undisturbed for either of the two study areas: the Chesapeake Bay and South Florida. Time constraints allowed for the study of only one area at a time and this work concentrated on the South Florida study area. South Florida was chosen first since it was thought that the relative simplicity of the coastline as compared to the Chesapeake Bay would permit a more straightforward analysis and explanation for the observed cloudiness pattern. Also the numerical model to be used in this study had been previously run extensively and successfully for South Florida; therefore, more confidence could be placed in the model results if run for this region. In addition, the summer of 1983 was very dry over the Chesapeake Bay region for most of

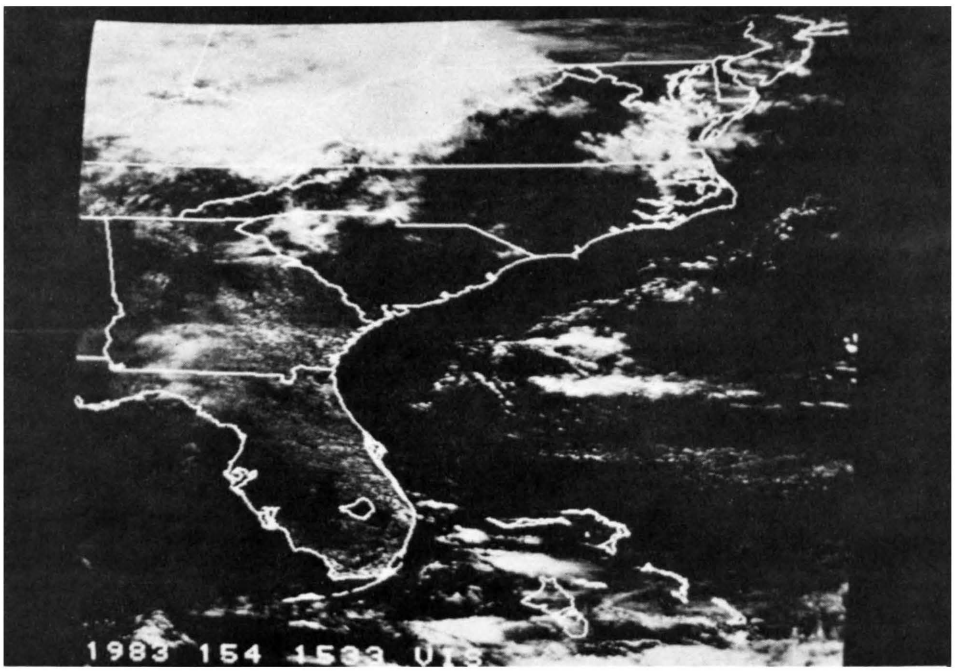


Fig. 2.1. Example of the original raw satellite data collected during the summer, 1983. This example is for June 2, 1983, at 8 a.m. EST.

the summer period so that there were few days with non-frontal related deep cumulonimbus convection.

The forecasts of undisturbed synoptic conditions were made by utilizing satellite data and the National Meteorological Center (NMC) output to locate synoptic disturbances near the study areas and to estimate their effect on the sea breeze circulation for that day. After the collection program ended, hard-copy satellite images were obtained for the study areas. These data were received from the laserfax receivers at the National Weather Service Forecast office at Camp Springs, Maryland, and Ruskin AFB, Florida. The satellite images were used to post verify the forecasts made. Only days with a pronounced diurnal variation in the cloud patterns were used in creating the composites. Out of the 39 days collected, 6 days were concluded to be synoptically disturbed in the post-analysis of South Florida, while 2 other days maintained diurnally forced deep convection until late in the day when offshore cloudiness associated with an upper-level trough moved near the shore. About 10 days which were scheduled for collection could not be archived due to hardware problems associated with the facilities.

Data was collected every other hour from 1300 GMT (8 EST) to 2300 GMT (18 EST) for a total of six hours per day. Visible image data were archived at ½-mile resolution while the infrared images were collected at 8-mile resolution (resolutions valid at the Equator; at the Florida latitude resolutions would be about 10% less).

The satellite images were processed on the Comtal Vision One/20 Image Processing System in the Department of Atmospheric Science. The

final processed images were transformed to and averaged on the Vax 11/780 computer.

The collected raw images were first sectorized into one image which centered on and included only the South Florida area and near offshore waters. Then the sectorized images were visually renavigated to a standard position by comparing the landmarks (i.e., lakes, coastlines, rivers). This was done on the Comtal system by creating a graphic with the South Florida geographic features on it and roaming each visible image on the Comtal to match with the graphics outline of South Florida. The infrared images were translated the same distance as the corresponding visible image.

In order to avoid contamination from the ground surface in the composites and to focus on the patterning of one type of cloud, the images were then reclassified. The reclassification process followed to some extent the techniques described by Weaver and Kelly (1982) and Klitch et al. (1985), as well as the bispectral method described by Reynolds et al. (1978) which extracts information from both the IR and visible images to create one reclassified image. Three types of reclassifications were used:

- Deep convection
- Developing cumulus
- All clouds except deep convection (low cloud).

Deep convection reclassified images were used in creating composite images which are presented in Chapter 5. The data for the last two reclassifications were used for the statistical analysis in Chapter 4.

For the deep convection classifications, both cloud top temperatures (Ct) from the infrared and the brightness count from the

visible images were used. The Ct threshold used to define deep convective clouds was determined from the 12 GMT (7 EST) sounding data for days when satellite data was collected and diurnal convection dominated. From these soundings, the level of free convection was found using the early afternoon surface conditions. For all those soundings, parcels could rise to at least the -38°C level. This was chosen as the threshold Ct which corresponds to a brightness count on the IR image of 185 (IR brightness ranges from 0 to 255).

A cloud which satisfied the above condition also must have had a visible image brightness count of greater than a certain value to be classified. The visible image brightness threshold was varied with time of day to account for the changing sun angle. Table 2.1 lists the visible brightness count threshold used for each time. Variation of sun angle with day of year during the summer was neglected.

This bispectral method allows for the omission of cold but visibly dark cloud tops like cirrus in the classification of deep convection. Before an image was classified, the adequacy of the thresholds to properly locate deep convection was visually checked on the Comtal system. Slight variations were made in the IR brightness thresholds if the initial classification was not fully representative. The variations in the threshold brightness count ranged between ±7 brightness counts from 185.

For developing cumulus clouds, the brightness counts were defined by a visible threshold of greater than a certain value depending on time of day and an IR brightness count less than 120 (warmer than -7°C). The visible image thresholds for the developing cumulus classification were the same as those used for deep convection shown

Table 2.1. Visible image brightness count threshold used in creating all IR reclassified images. Threshold varies with time of day to include the effect of varying solar zenith angle on the visible image brightness. The 1400 EST threshold was the base for which the other thresholds were corrected to.

| Time of Day (EST) | Visible Image Brightness Count Threshold | |
|---|---|---|
| | Developing Cumulus and Deep Convective Clouds | Low Cloud |
| 8 | 36 | 21 |
| 10 | 43 | 24 |
| 12 | 46 | 25 |
| 14 | 45 | 25 |
| 16 | 40 | 23 |
| 18 | 26 | 15 |

in Table 2.1. By employing these conditions, the developing cumulus clouds would be ones having lower, warmer tops while also appearing bright on the visible image. It was expected that these clouds would show where convection was initiated. Some possible errors were introduced in this classification after strong convection was generated. Sometimes the edges of deep convective clouds were classified in the developing cumulus range, although, of course, these areas could be new shallow cumulus development growing on the edge of deeper clouds. This feature was small through 12 EST but became more significant as more cumulonimbus clouds became present from 14 to 18 EST.

The third type of classification was determined from the visible image only and was used to represent all clouds except deep convection. A pixel in an image was classified if the visible image brightness was less than a certain value which also depended on time of day. These brightness count thresholds are also given in Table 2.1. This type of classification will be referred to hereafter as the low cloud classification.

The low and deep convective cloud classifications were combined into one three-shaded image for each raw satellite image. All clouds which were defined to be low clouds by the classification were given an intermediate brightness value while all classified deep convective clouds were identified with the maximum brightness of 255. Therefore, when the three-shaded image was displayed, low clouds appeared grey, deep convective clouds were white, while the ground and water were black. This allowed for a considerable storage saving as two classifications were stored on one image and each classification could still be easily distinguished.

After the clouds were reclassified for an image, the number of pixels over the South Florida land area and over the surrounding waters covered by each of the three types of classifications were obtained by utilizing the classifier command on the Comtal system. Figure 2.2 shows the area over land and the area over water for which the above procedure was applied. The number of pixels that each reclassification covered was normalized by the number of pixels over the land and over the water. Thus, the percent area over water was obtained giving six quantitative variables to describe the percent cloudiness over the study area.

The reprocessed images were then used to make the composite images. First, all pixels which were classified to the particular cloud type which was to be composited were found. These pixels were temporarily given the maximum brightness count of 255 (which appears as white when displayed) and then included in the running average for that pixel. If the pixel was not reclassified to the type of cloud that the averaging program was searching for, then the pixel was temporarily given a zero value (which appears black when displayed) and then included in the running average. Therefore, after an IR composite was complete, a pixel would appear white (i.e., a value of 255) when displayed only if the particular cloud type had been present at that pixel location for all the images which went into making the composite. The brightness counts on the composite image could then be related to a probability of finding a particular cloud type in an area. This procedure was used in creating all the IR reclassified composites.

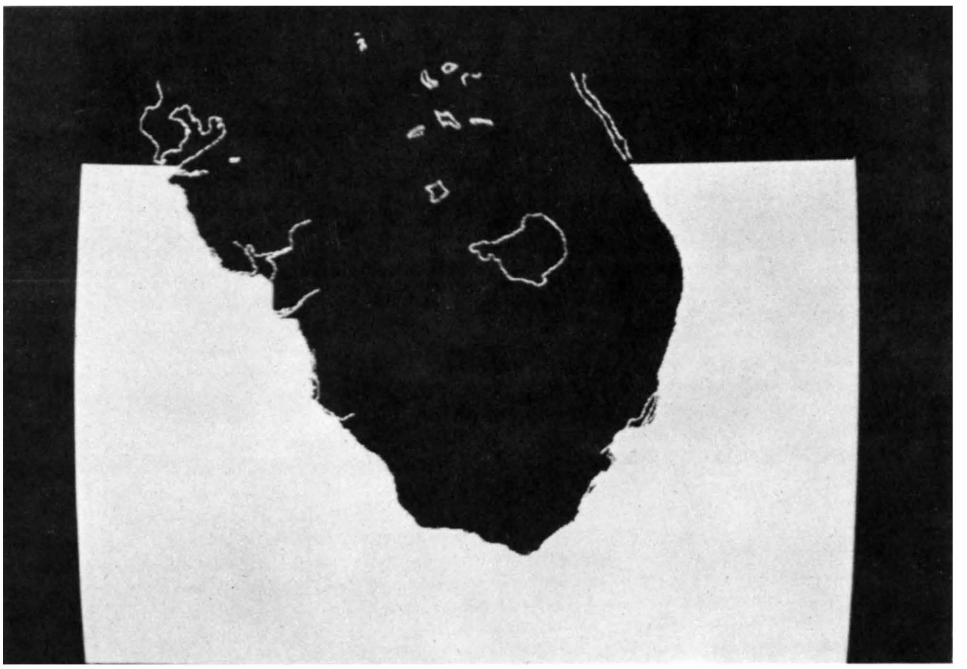

Fig. 2.2. Picture taken from the Comtal image processing system showing the areas used to obtain the percent cloudiness over land and water for South Florida. The shaded area shows the area over water. The black area inside the Florida outline shows the land area.

The visible image composite was just a simple pixel-by-pixel average of the raw data brightness counts. Therefore, no readjustment of a pixel's brightness was ever made during processing or averaging, as was done for the IR reclassified composites. The visible image composites, then, included the visible brightness for all types of clouds without trying to determine the pattern of one cloud type, as was accomplished with the reclassified composites.

## 2.2 The Rawinsonde Data

The morning sounding data was collected for West Palm Beach and Key West, Florida, from the Bureau of Reclamation archives for each day when satellite data was collected. Key West was used in processing when available; otherwise Palm Beach was utilized.

Betts (1974) looked at vertical profiles of equivalent potential temperature ($\theta_e$), saturated equivalent potential temperature ($\theta_{es}$), and the difference between the two ($\theta_{es}-\theta_e$) to obtain a graphical representation of the temperature and moisture profiles of a tropical environment for varying degrees of convection. This method was also used here to note the difference in thermodynamic environments between the different synoptic flow categories. These synoptic categories will be defined in the next section. Before averaging the sounding data, $\theta_{es}$ was calculated at each level ($\theta_e$ was provided as part of the output by the Bureau of Reclamation) from

$$\theta_{es} = \theta \exp\left(\frac{L_c q_s}{c_p T}\right) \tag{2.1}$$

where $\theta$ is potential temperature, $L_c$ is the latent heat of condensation, $q_s$ is the saturated specific humidity, $c_p$ is specific

heat at a constant pressure, and T is the temperature at the level at which $\theta_{es}$ is to be calculated.

$\theta_e$ and $\theta_{es}$ as well as the variables needed to initialize the mesoscale model (z, $\theta$, q, u, v) were interpolated to every 20 mb above the surface pressure for each sounding. Then all variables were averaged within each synoptic class at the interpolated pressure levels. Standard deviations and variances were calculated for each level in the averaged sounding when more than two soundings were available for a synoptic class. Vertical profiles of these averaged quantities for each synoptic class were then plotted. The averaged variables needed to initialize the model were reinterpolated to the model levels.

For a more quantitative description of the thermodynamic environment for each collect day, several other variables were calculated from each sounding. The following variables were calculated from the sounding data:

1. The magnitude of convective instability ($\overline{\Delta\theta_e}$).
2. The depth of convective instability ($\Delta P$).
3. The magnitude of moisture deficiency ($\overline{\theta_{es} - \theta_e}$).
4. The lifted index at 500 mb.

The first three variables were used by Pielke et al. (1977) to study the relationship between rainfall amounts over South Florida and the large-scale environment. For each collect day, $\Delta P$ was determined by first plotting $\theta_e$ and $\theta_{es}$ from the morning sounding. $\Delta P$ was the depth of the layer where

$$\frac{\partial \theta_e}{\partial z} < 0.$$

In South Florida this layer typically extended from the surface to the middle troposphere. Mean values of the gradient of equivalent potential temperature, $\overline{\Delta\theta_e}$, and of the difference between saturated and equivalent potential temperature $\overline{\theta_{es} - \theta_e}$ were found using

$$\overline{\Delta\theta_e} = (\int_{P_{sfc}}^{P_{sfc}-\Delta p} \delta\theta_e \times dP)/\Delta P \tag{2.2}$$

$$\overline{\theta_{es} - \theta_e} = (\int_{P_{sfc}}^{P_{sfc}-\Delta P} (\theta_{es} - \theta_e)dP)/\Delta P \tag{2.3}$$

where $$\delta\theta_e = (\theta_e(P) - \theta_e(P+dP)) \tag{2.4}$$

Physically, $\Delta P$ measures how deep the convective instability was. $\overline{\Delta\theta_e}$, and the lifted index provide a quantitative measure of the convective instability of the large-scale environment. The average, $\overline{\theta_{es} - \theta_e}$, relates how moist the troposphere was through the depth of convective instability. Each of these variables describes quantitatively the average large-scale thermodynamic environment. The plots of the vertical profiles of the mean soundings and their standard deviations provide a more qualitative viewpoint of this environment, but with vertical structure. This information is used in Section 4.2 as part of the statistical data with which to correlate these synoptic scale measures with the intensity and coverage of the satellite observed convective cloud activity that occurred during the case study days.

## 2.3 Synoptic Classification of Collect Days

A review of previous meteorological data compositing studies over South Florida was given in the previous chapter. Several of these studies used synoptic scale parameters to stratify the original data

into classes and then composite the data for these classes. For Florida, from these studies, it was found that the low-level synoptic flow was a primary mechanism for controlling the location of the sea breeze convergence zone and its associated convective activity. Case studies of satellite data over the area from Pielke (1973), numerical modeling studies by Pielke (1974) and statistical results by Burpee (1979), Burpee and Lahiff (1984) and Pielke et al. (1977) have also all confirmed the importance of the low-level synoptic flow in forming the sea breeze convective patterns. For this study, the low-level geostrophic flow field was used to categorize each synoptically undisturbed collect day.

The mean geostrophic wind speed and direction over South Florida was computed subjectively from the NMC surface maps for the summer of 1983. The geostrophic wind speed was calculated from

$$V_g \cong \frac{1}{\rho f} \frac{\delta P}{\delta n} \tag{2.5}$$

where $\rho$ is a mean surface density derived using a surface standard atmospheric value of 1.2 kg/m$^3$, $f$ is the Coriolis parameter for 26° N ($f = 6.6 \times 10^{-5}$ s$^{-1}$), while $(\delta p/\delta n)$ is the pressure gradient across southern Florida. The geostrophic wind direction, of course, was taken to be parallel to the isobars over the study area. Often due to curvature of the isobars and varying pressure gradients over Florida, more than one geostrophic wind was calculated for the area and the average of the calculated geostrophic winds was used to define the synoptic category for that day.

The days were then categorized as follows:

- Strong wind days if $V_g > 3.5$ m/s
- Light wind days if $1 \text{ m/s} \leqq V_g \leqq 3.5$ m/s
- Very light and variable wind days if $V_g < 1$ m/s

Typically this latter category occurred when high pressure was centered over the study region.

The days were further categorized by surface geostrophic wind direction as defined in Table 2.2. The number of collect days for each category are also listed. All told there are 10 categories where at least one case day was collected. Satellite data was composited for each category as well as for all undisturbd cases for the visible images and for each type of IR reclassified images. Using the averaging techniques described in the last section, mean soundings were also created for each of the synoptic flow categories.

Table 2.2. Definition of each synoptic wind category by surface geostrophic wind and the number of synoptically undisturbed collect days in each category.

| Synoptic Class | Geostrophic Wind Direction | Light Winds ($V_g \leq 3.5$ m/s) | Strong Winds ($V_g > 3.5$ m/s) |
|---|---|---|---|
| 1. Northeast | 1-60° | 2 | 0 |
| 2. East | 61-120° | 2 | 7 |
| 3. Southeast | 121-180° | 7 | 7 |
| 4. Southwest | 181-240° | 0 | 1 |
| 5. West | 241-300° | 1 | 0 |
| 6. Very Light and Variable ($V_g \leq 1$ m/s) | --- | 4 | --- |
| 7. All undisturbed | --- | 31 | --- |
| 8. Disturbed | --- | 8 | --- |

# CHAPTER 3

# THE NUMERICAL MODEL

## 3.1 The Model Framework

The numerical model used in this study was originally developed by Pielke (1974). The model has been extended since to include topographic features, a surface energy budget, and long and short wave radiation. These improvements have been reported in Mahrer and Pielke (1975, 1977, 1978), Pielke and Mahrer (1978), McNider and Pielke (1981), and Segal and Pielke (1981). Also included in the model used in the present study are the parameterizations of the soil layer described by McCumber and Pielke (1981) and Kessler et al. (1985), and of vegetation canopy described by McCumber (1980). Since there is no moist physics or rain scheme incorporated in the model, the ground surface parameterizations are most useful before the onset of rain when the soil moisture content is not affected by precipitation. The model used here is hydrostatic, three-dimensional and is initialized from a barotropic synoptic state. Topography was assumed flat for all the simulations shown in this report; therefore, all equations shown will omit the terrain following coordinate system available in the recent version of the model. The model governing equations are

$$\frac{du}{dt} = fv - fv_g - \Theta \frac{\partial \pi}{\partial x} + \frac{\partial}{\partial x}\left(K_H \frac{\partial u}{\partial x}\right) + \frac{\partial}{\partial y}\left(K_H \frac{\partial u}{\partial y}\right) + \frac{\partial}{\partial z}\left(K_z^m \frac{\partial u}{\partial z}\right) \tag{3.1}$$

$$\frac{dv}{dt} = - fu + fu_g - \theta \frac{\partial \pi}{\partial y} + \frac{\partial}{\partial z}\left(K_z^m \frac{\partial v}{\partial z}\right) + \frac{\partial}{\partial x}\left(K_H \frac{\partial v}{\partial x}\right) + \frac{\partial}{\partial y}\left(K_H \frac{\partial v}{\partial y}\right) \tag{3.2}$$

$$\frac{d\theta}{dt} = \frac{\partial}{\partial z}\left(K_z^\theta \frac{\partial \theta}{\partial z}\right) + \frac{\partial}{\partial x}\left(K_H \frac{\partial \theta}{\partial x}\right) + \frac{\partial}{\partial y}\left(K_H \frac{\partial \theta}{\partial y}\right) \tag{3.3}$$

$$\frac{dq}{dt} = \frac{\partial}{\partial z}\left(K_z^q \frac{\partial q}{\partial z}\right) + \frac{\partial}{\partial x}\left(K_H \frac{\partial q}{\partial x}\right) + \frac{\partial}{\partial y}\left(K_H \frac{\partial q}{\partial y}\right) \tag{3.4}$$

$$\frac{du}{dx} + \frac{dv}{dy} + \frac{dw}{dz} = 0 \tag{3.5}$$

$$\frac{\partial \pi}{\partial z} = - \frac{g}{\theta} \tag{3.6}$$

where the scaled pressure, $\pi$, is defined by

$$\pi = \theta \left(\frac{P}{P_{oo}}\right)^{R/c_p} \tag{3.7}$$

Respectively, equations 3.1 through 3.6 are the equations of motion for u and v, the thermodynamic equation, the conservation equation for specific humidity, the incompressible continuity equation, and the hydrostatic equation. A complete list of variable definitions appears in Appendix A.

## 3.2 Description of Model Physics

### 3.2.1 Boundary Layer

The surface layer fluxes of heat, moisture, and momentum are based on the work of Businger (1973), while the turbulent mixing in the remainder of the planetary boundary layer was parameterized for an unstable surface layer using an exchange coefficient formulation as described by O'Brien (1970). The depth of the planetary boundary layer for this case of upward heat flux is predicted using a formulation introduced by Deardorf (1974). An improved treatment of the

stable boundary layer adopting a local eddy diffusion form has been incorporated by McNider and Pielke (1981).

3.2.2 Radiation

The changes of air temperature due to short- and long-wave radiative fluxes are parameterized following the methods of Atwater and Brown (1974). Heating of the atmosphere by short-wave radiation is confined to water vapor, while carbon dioxide and water vapor are considered in the long-wave radiation heating/cooling algorithm.

3.2.3 Ground Surface

Most of the modifications made to the existing model during this study were performed for the treatment of the air-surface interactions. These modifications, which are based on McCumber's (1980) work, were incorporated into the model to help locate areas of enhanced or suppressed vertical motions that are due to spatial variations in the characteristics of the land ground surface. These new features to the model will now be discussed in detail. No major changes have been incorporated in the ground surface physics from what was developed by McCumber.

A. Soil Physics. On land, a surface heat balance equation is solved iteratively for surface temperature, $T_G$, at each surface grid point as described by Mahrer and Pielke (1977). The surface heat balance equation is

$$R_{sw}\downarrow + R_{Lw}\downarrow + \rho L_c u_* q_* + \rho c_p u_* \theta_* - G + \sigma T_G^4 = 0 \qquad (3.8)$$

Table 3.1 outlines the interpretation of each term and the definitions of the turbulent quantities.

Table 3.1. Surface energy budget (Tunick, 1984).

| $R_{sw}\downarrow + R_{Lw}\downarrow$ | $\rho L_c u_* q_*$ | $\rho C_p u_* \theta_*$ | $G = \lambda \left.\frac{\partial T_s}{\partial z}\right\|_G$ | $\sigma T_G^4$ |
|---|---|---|---|---|
| Incoming radiative fluxes | Latent heat flux | Sensible heat flux | Surface heat conduction | Long-wave emission |

where

$$u_* = k_o (u^2 + v^2)^{\frac{1}{2}}/(\ln(z/z_o) - I_1) \tag{3.9}$$

$$\theta_* = k_o(\theta - \theta(z_o))/(\ln z/z_o - I_2) \tag{3.10}$$

$$q_* = k_o(q - q(z_o))/(\ln(z/z_o) - I_2) \tag{3.11}$$

and $I_1$ and $I_2$ are stability adjustments as defined in Mahrer and Pielke (1977), $z_o$ is the turbulent roughness height and $\lambda$ is the thermal conductivity. $\varepsilon_G$ is the soil emissivity. The Newton-Raphson iterative algorithm discussed in Mahrer and Pielke (1977) is used to solve for the surface soil temperature, $T_G$, in equation 3.8.

The following outlines the method of solving for the heat and moisture fluxes in the soil which are used to update surface temperature in equation 3.8. In the soil, only vertical diffusion is allowed so

$$C \frac{\partial T_s}{\partial t} = \frac{\partial H_s}{\partial z} \tag{3.12}$$

where

$$H_s = \lambda \frac{\partial T_s}{\partial z} \tag{3.13}$$

is the vertical soil heat flux. $C$ in equation 3.12 is the volumetric heat capacity defined by

$$C = (1 - \eta_s)C_i + \eta C_w \quad ; \tag{3.14}$$

$\eta$ is the volumetric moisture content. This is the volume of water (vapor plus liquid) contained in a unit volume of soil. $\eta_s$ is the saturated moisture content, also called porosity. $C_i$ is the air dry volumetric heat capacity for a soil type i. $C_w$ is the heat capacity for water which was taken to be 418 $Jm^{-3}{}^{o}C^{-1}$ for the model runs. Equation 3.14 is simply a weighting of the contribution to the volumetric heat capacity of the dry soil and of the liquid water that is present. The heat capacity of air was omitted in equation 3.14 since it is negligibly small (McCumber, 1981).

The functional form of the thermal conductivity, $\lambda$, used in equation 3.13 is

$$\lambda = \exp\,(-(\log_{10}\psi + 2.7)) \qquad \log_{10}\psi \leqq 5.1$$

$$\lambda = .00041 \qquad \log_{10}\psi > 5.1 \tag{3.15}$$

$\psi$ is the moisture potential which is the suction pressure required to extract water from the soil. $\psi$ is in units of length which express the height of a water column supportable by the required suction pressure. $\psi$ is always negative and its absolute value decreases with increasing soil moisture.

For soil moisture, the prognostic equation used is

$$\rho_w \frac{\partial \eta}{\partial t} = \frac{\partial w_s}{\partial z} \tag{3.16}$$

where $w_s$ is the moisture flux into the soil and $\rho_w$ is the density of liquid water. Horizontal advection in the ground can be neglected on the mesoscale time periods (Pielke, 1984). Symbolically the soil moisture flux is

$$w_s = K_\eta \rho_w \frac{\partial}{\partial z} (\psi + z) \quad ; \tag{3.17}$$

$K_\eta$ is called the hydraulic conductivity. Physically, $K_\eta$ is an exchange coefficient which accounts for the influence of gravity drainage in a viscous soil. $K_\eta$ increases as soil moisture content increases.

Another form of the equation for the soil moisture flux can be found by using the definition of diffusivity. Diffusivity is analogous to the exchange coefficient in the representation of turbulence in the atmosphere and is given by

$$D_\eta = K_\eta \frac{\partial \psi}{\partial \eta} \tag{3.18}$$

Using this equation 3.17 becomes

$$w_s = D_\eta \rho_w \frac{\partial \eta}{\partial z} + K_\eta \rho_w \quad ; \tag{3.19}$$

$\psi$ and $W_\eta$ are functions of $\eta$ and soil type. Using the empirical relations for them derived by Clapp and Hornberger (1978) yields

$$\psi = \psi_s (\frac{\eta_s}{\eta})^b \tag{3.20}$$

$$K_\eta = K_{\eta s} (\frac{\eta}{\eta_s})^{2b+3} \tag{3.21}$$

Substituting for $K_\eta$ in equation (3.18) gives

$$D_\eta = \frac{-b\ K_{\eta s}\ \psi}{\eta} (\frac{\eta}{\eta_s})^{b+3} \tag{3.22}$$

Subscript s refers to soil saturation. The exponent b as well as $\eta_s$, $\psi_s$, $K_{\eta s}$, and $D_{\eta s}$ are all functions of the USDA soil textural classes.

Soil moisture content is predicted through a specified depth of the soil and continuity of the moisture flux at the air-soil interface is imposed through an iterative process. Continuity is insured by forcing

$$w_a - (w_s)_G = 0 \tag{3.23}$$

where $w_a$ is the turbulent atmospheric moisture flux at the surface defined by

$$w_a = \rho u_* q_* \tag{3.24}$$

At the start of each time step, $w_a$ is calculated from 3.24 and $w_s$ from 3.17. If $(w_a - w_s)/w_s > .001$, an iterative process begins and proceeds as follows.

(1) $w_s$ is calculated again, and hereafter, for each iteration by

$$(w_s)_G^{n+1} = \delta(w_s)_G^n + (1-\delta)w_a \qquad 0 \leqq \delta \leqq 1 \tag{3.25}$$

where superscript n refers to the $n^{th}$ iteration guess. $\delta$ is an empirically derived weighting function which helps to force $w_s$ toward $w_a$. As indicated by McCumber and Pielke (1981), $\delta$ must be skewed toward 1 for extremely dry soils to ensure convergence.

(2) Now that the soil moisture flux is updated, it can be used to update the soil moisture potential. This is accomplished by inverting equation 3.17 and placing it into finite difference form

$$\psi_G = \psi_{G-1} + (z_G - z_{G-1})\rho_w[(w_s)_G\{((K_\eta)_G + (K_\eta)_{G-1})/2\} - 1] \tag{3.26}$$

Subscript G refers to the ground surface and G-1 refers to the next lower soil level.

(3) $\eta$ is then calculated by inverting equation 3.20 for moisture potential so that

$$\eta = \eta_s / (\frac{\psi}{\psi_s})^{1/b} \tag{3.27}$$

(4) $K_\eta$ and $D_\eta$ at the surface are now updated using equations 3.21 and 3.22.

(5) The convergence of $\psi_G$ is checked by requiring that

$$\frac{\psi_G^{n+1} - \psi_G^n}{\psi_G^n} < 0.01 \tag{3.28}$$

If this condition is not satisfied, we return to step (2) where $\psi_G$ is recomputed with the updated value of $K_\eta$, then steps (3) and (4) are repeated.

(6) A surface relative humidity is calculated from

$$h = \exp\ (-g\psi_G / R_v T_G) \tag{3.29}$$

(7) The surface specific humidity, $q_G$, can now be obtained from

$$q_G = h\ q_s \tag{3.30}$$

where $q_s$, the saturated specific humidity, is written as

$$q_s = 0.622\ \frac{e_s}{P - 0.378\ e_s} \tag{3.31}$$

and the saturation vapor pressure, $e_s$, is only a function of surface temperature

$$e_s = 6.1078\ \exp\left[(17.269)\ \frac{T_G - 273.16}{T_G - 35.86}\right] \tag{3.32}$$

(8) The new value of $q_s$ is used to obtain $w_a$. Steps (1) through (8) are repeated until $w_a$ and $(w_s)_G$ fulfill the convergence criteria.

After $w_a$ and $(w_s)_G$ have converged, the prognostic equation for $\eta$ (equation 3.16) is solved in which vertical diffusion of soil

moisture is incorporated. As a lower boundary for solving diffusion, $\eta$ remains constant at the bottom level in the soil. If vegetation is present, the transpiration loss of soil moisture is taken into account. The transpiration uptake is affected throughout the root zone. Equation 3.16 is modified for root uptake of soil moisture as follows

$$\rho_w \frac{\partial \eta}{\partial t} = \frac{\partial}{\partial z} w_s + A(z) \tag{3.33}$$

Substituting for $w_s$ using equation 3.17 yields

$$\frac{\partial \eta}{\partial t} = \frac{\partial}{\partial z} (D_\eta \frac{\partial \eta}{\partial z}) + \frac{\partial K_\eta}{\partial z} + A(z) \tag{3.34}$$

$A(z)$ is the root extraction term. It serves to reduce the amount of soil moisture in the soil. Its form in the model is

$$A(z) = E_{tr} \frac{R(z)\ \eta}{\int_{G-r}^{G} R(z) D_\eta dz} \tag{3.35}$$

where $R(z)$ is a root distribution function accounting for the vertical profile only, $r$ is the root depth, and $G$ is the ground surface. This simple and easy-to-apply approach has been reported to be reasonable by McCumber (1980). New values of $K_\eta$, $\psi$ and $D_\eta$ for all soil levels are then calculated from 3.28, 3.25 and 3.22 using the updated value of $\eta$.

With the updated value of $\eta$, the heat capacity, $C$, and thermal conductivity, $\lambda$, are also updated from equations 3.14 and 3.15 respectively. Now the soil heat flux can be calculated from equation 3.17.

The surface albedo is also a function of surface soil moisture and is obtained from

$$a_s = 0.31 - 0.34\Delta \qquad \Delta \leqq 0.5$$

$$a_s = 0.14 \qquad \Delta > 0.5$$

$$\Delta = \eta/\eta_s \tag{3.36}$$

Equation 3.36 is used for all soil classes except peat, for which limiting albedos are known. The relationship for peat is

$$a_s = 0.14(1-\Delta) \qquad \Delta \leqq 0.5$$

$$a_s = 0.07 \qquad \Delta > 0.5 \tag{3.37}$$

The total albedo is

$$a = a_z + a_s \tag{3.38}$$

where

$$a_z = (\exp(0.003286\ Z^{1.5}) - 1)/100 \tag{3.39}$$

and $Z$ is the solar zenith angle.

The total albedo is multiplied by the incident short-wave radiative fluxes from the atmosphere to determine the effective short-wave radiative flux reflection at the surface. The radiative fluxes along with the surface sensible, latent and soil heat fluxes are used in the surface energy balance, equation 3.8, to solve for $T_G$.

B. Vegetation. The parameterization used to include the effects of vegetation at the ground is that developed by McCumber (1980). This treatment of vegetation was based on Deardorf's (1978) work where a single level canopy assumed the properties of a large leaf. The major difference between the two works is that Deardorf's techniques parameterize a canopy of given density throughout a grid area, while McCumber's formulation assumes a dense canopy which occurs over a fraction of a grid area with entirely bare soil in the remainder. The inclusion of vegetation will primarily affect the surface temperature,

roughness, and heat, radiative and moisture fluxes. The description of the parameterization of each of these effects follows.

An energy balance, much like the one used for bare soil described in the last section, is applied to solve for the equilibrium foliage temperature, $T_f$, at the top of the canopy. This is expressed by

$$(R\downarrow_{sw} - R\uparrow_{sw})_C + (R\downarrow_{Lw} - R\uparrow_{Lw})_C - (R\downarrow_{sw} - R\uparrow_{sw})_G$$

$$- (R\downarrow_{Lw} - R\uparrow_{Lw})_G + (H + LE)_C - (H + LE)_G = 0 \qquad (3.40)$$

where the subscripts C and G refer to the fluxes at the vegetation canopy and ground, respectively. Canopy storage of energy is assumed negligible.

Before outlining the computational sequence, the energy balance equation above will be condensed. The radiation terms incident on the canopy from the atmosphere, $R\downarrow_{sw_c}$ and $R\downarrow_{Lw_c}$, were qualitatively described in Section 3.2.2. The other individual short-wave fluxes are

$$R\uparrow_{sw_c} = [(1-\sigma_f)(a_z+a_s) + \sigma_f(a_f+a_z)]R\downarrow_{sw_c} \qquad (3.41)$$

$$R\downarrow_{sw_G} = (1-\sigma_f)R\downarrow_{sw_c} \qquad (3.42)$$

$$R\uparrow_{sw_G} = (a_z+a_s)(1-\sigma_f)R\downarrow_{sw_c} \qquad (3.43)$$

where $\sigma_f$ is the vegetation shielding factor and represents the fractional coverage of the ground by vegetation. $a_f$ is the foliage albedo. The short-wave flux below the canopy top has been ignored. With these definitions, all the short-wave terms can be combined to form

$$(R\downarrow_{sw} - R\uparrow_{sw})_c - (R\downarrow_{sw} - R\uparrow_{sw})_G = \sigma_f(1-a_f-a_z)R\downarrow_{sw_c} \qquad (3.44)$$

The individual long-wave terms are

$$R\uparrow_{Lw_c} = (1-\sigma_f)[\varepsilon_G\sigma T_G^4 + (1-\varepsilon_G)R\downarrow_{Lw_c}]$$

$$+ \sigma_f[\varepsilon_f\sigma T_f^4 + (1-\varepsilon_f)R\downarrow_{Lw_c}] \quad (3.45)$$

$$R\downarrow_{Lw_G} = (1-\sigma_f)\ R\downarrow_{Lw_c} + \sigma_f Rv_{\downarrow Lw_G} \quad (3.46)$$

$$R\uparrow_{Lw_G} = (1-\sigma_f)[\varepsilon_G\sigma T_G^4 + (1-\varepsilon_G)R^v\downarrow_{Lw_G}] + \sigma_f R^v\uparrow_{Lw_G} \quad (3.47)$$

where $\varepsilon_G$ and $\varepsilon_f$ are the emissivities of the ground and foliage, respectively.

$R^v\downarrow_{Lw_G}$ and $R^v\uparrow_{Lw_G}$ are the downward and upward longwave fluxes within the canopy and are defined by

$$R^v_{Lw\ \uparrow\ G} = \varepsilon_G\sigma T_G^4 + (1-\varepsilon_G)R^v_{Lw\ \downarrow\ G} \quad (3.48)$$

$$R^v_{Lw\ \downarrow\ G} = \varepsilon_f\sigma T_f^4 + (1-\varepsilon_f)R^v_{Lw\ \uparrow\ G} \quad (3.49)$$

Substituting $R^v_{Lw_G\downarrow}$ into 3.48 and $R^v_{Lw_G\downarrow}$ into 3.49 gives

$$R^v_{Lw_G\downarrow} = \varepsilon_f\sigma T_f^4 + (1-\varepsilon_f)\varepsilon_G\sigma T_G^4 + (1-\varepsilon_G)(1-\varepsilon_f)R^v{}_{Lw\ G\downarrow}$$

and

$$R^v_{Lw_G\uparrow} = \varepsilon_G\sigma T_G^4 + (1-\varepsilon_G)\sigma T_f^4 + (1-\varepsilon_f)(1-\varepsilon_G)R^v_{Lw_G\uparrow}$$

or rearranging

$$R^v_{Lw_G\downarrow} = [\varepsilon_G\sigma T_G^4 + (1-\varepsilon_G)\varepsilon_f\sigma T_f^4]/(\varepsilon_f + \varepsilon_G - \varepsilon_f\varepsilon_G) \quad (3.50)$$

$$R^v_{Lw_G\uparrow} = [\varepsilon_f\sigma T_f^4 + (1-\varepsilon_f)\varepsilon_G\sigma T_G^4]/(\varepsilon_f + \varepsilon_G - \varepsilon_f\varepsilon_G) \quad (3.51)$$

To simplify the latent and sensible heat fluxes in equation 3.40, the forms of the terms weighted by vegetation coverage are written

$$(H + LE)_C = \sigma_f(H' + LE')_C + (1-\sigma_f)(H'+LE')_G$$

and

$$(H+LE)_G = (1-\sigma_f)(H'+LE')_G$$

The difference between the two sums is just

$$\sigma_f(H'+LE')_C$$

The primed variables are the fluxes for each surface before being weighted by $\sigma_f$.

The longwave terms given in 3.45, 3.46, 3.47, 3.50, and 3.51, along with 3.44 and the simplified expression for the heat fluxes, will after rearranging give a condensed equation for the balance equation for the canopy, i.e.

$$\sigma_f[(1-a_f-a_z)R\downarrow_{sw_c} + \varepsilon_f R\downarrow_{Lw_c} + \frac{\varepsilon_f \varepsilon_G}{\varepsilon_f + \varepsilon_G - \varepsilon_f\varepsilon_G}\sigma T_G^4$$

$$- \frac{\varepsilon_f + 2\varepsilon_G - \varepsilon_f\varepsilon_G}{\varepsilon_f + \varepsilon_G - \varepsilon_f\varepsilon_G}\varepsilon_f\sigma T_f^4 + \sigma_f(H'+LE')_C = 0 \qquad (3.52)$$

This is the form of the equation which is solved for $T_f$ using the Newton-Raphson iteration sequence. The first step is to calculate the radiation terms which do not depend on $T_f$. These are the first three terms of 3.52. The incident radiation at the top of the canopy is calculated as described qualitatively in Section 3.2.2. Albedo for the foliage, $a_f$, is given as part of the initial conditions while $a_z$ is calculated from 3.39. The emissivities for the foliage and ground are also given a constant value (see Table 3.3). The ground surface temperature, $T_G$, is given the value calculated from the previous timestep. The method to obtain $T_G$ for bare soil was outlined in the previous section. However, some modifications are made to the ground surface energy budget when vegetation is present. These modifications will be described later.

The canopy sensible and latent heat fluxes, $H'_C$ and $LE'_C$, needed to solve 3.52 are defined using a drag formulation

$$H'_C = 1.1\ L_A \rho C_p C_f U_{af} \left(\frac{1000\ mb}{P(mb)}\right)^{0.286} (T_{af} - T_f) \tag{3.53}$$

and

$$LE'_C = L_A \rho L_C f' C_f U_{af} (q_{af} - q_s(T_f)) \tag{3.54}$$

The terms in these equations will now be defined and described.

$L_A$ is the leaf area index defined as the total one-sided leaf area of the foliage relative to the same size ground area. McCumber used $L_A = 7\sigma_f$. The constant 1.1 in 3.53 was included by Deardorf (1978) to account for the effect of stems, branches, and trunks of vegetation which were assumed not to be included in the equation.

$C_f$, the transfer coefficient in equations 3.53 and 3.54, is defined by

$$C_f = .01(1 + 0.3/U_{af}) \tag{3.55}$$

The constant, .01, was derived for forced convection over several types of plants. The last term in parentheses accounts for the transfer of heat, moisture and momentum during free convection. $U_{af}$, the wind speed within the free air beneath the vegetation canopy, should be given in m/s.

$U_{af}$ is estimated by

$$U_{af} = 0.83 C_G^{\frac{1}{2}} U_a \tag{3.56}$$

where $U_a$ is the wind speed in the free atmosphere at the lowest model level above canopy height. $C_G$, a nondimensional transfer coefficient valid within the canopy, is calculated by

$$C_G = \left[\frac{k_o}{\ln(z-D)/z_o}\right]^2 \tag{3.57}$$

where $k_o$ is the Von Karmen constant (0.35), $z_o$ is the turbulent roughness length, D is the zero plane displacement height. When the ground cover is high enough such that significant turbulent flow can occur beneath the top, values of $z_o$ are displaced the distance, D, from the ground surface. $D = 0.76\ H_c$ where $H_c$ is the mean canopy height. $(C_G^{\frac{1}{2}} U_a)$ is analogous to a turbulent friction velocity. No adjustment is made to $C_G$ for atmospheric stability.

$T_{af}$ and $q_{af}$ are the temperature and specific humidity within the vegetation canopy and are defined by

$$T_{af} = 0.3\ T_a + 0.6 T_f + 0.1 T_G \tag{3.58}$$

$$q_{af} = 0.3 q_a + 0.6 q_f + 0.1 q_G \tag{3.59}$$

These variables are weighted toward the vegetation characteristics. Deardorf (1978) argued that they should be weighted in this way if the canopy is relatively dense. $q_f$, in 3.59, is the specific humidity of the foliage stoma calculated from

$$q_f = f' q_s(T_f) + (1-f') q_{af} \tag{3.60}$$

with the restriction that $q_f \leqq q_s(T_f)$.

f' is the fraction of potential evapotranspiration available from the vegetation and is also needed to close out the definitions for the terms in the canopy heat flux equation. f' is expressed by

$$f' = 1 - \delta_w \frac{r_s}{r_s + r_a} \left[ 1 - \frac{w_L}{w_I} \right]^{2/3} \tag{3.61}$$

$\delta_w$ is zero if condensation is occurring onto the leaf ( i.e. if $q_{af} > q_s(T_f)$, $q_f = q_s(T_f)$ in equation 3.60). $\delta_w$ equals one otherwise. $w_L$ is the amount of liquid water retained on the foliage per unit ground area. Pielke (1984) reports values of $w_L = 0.2$ mm due to dew

formation at night in a cloud-free, arid environment. $w_I$ is the maximum interception storage and refers to the amount of water that can remain on vegetation before it falls to the ground of its own weight. $w_I$ is a function of the plant type and is determined from the individual plant geometry. The expression in brackets in 3.61 is proportional to the fractional foliage surface not covered by dew.

With the inclusion of $f'$ in 3.54, the latent heat flux at canopy top, $LE'_C$, can be interpreted as follows:

| | |
|---|---|
| $\delta_w = 0$ | $LE'_C$ is the rate of condensation of dew onto the foliage. |
| $\delta_w = 1,\ w_L > 0$ | $LE'_C$ is the rate of transpiration plus evaporation of dew. |
| $\delta_w = 1,\ w_L = 0$ | $LE'_C$ is the transpiration rate and no dew or retained water is present. This is the usual daytime case. |

Deardorf (1978) explains that the purpose of the exponent, 2/3, in 3.61 is to approximate the agglomeration of an evaporating film of water into discrete droplets which would act to cover less leaf surface and accelerate the evaporation of water.

The final terms to be discussed in 3.61 are the coefficients of bulk stomatal resistance and the generalized atmospheric resistance, $r_s$ and $r_a$. $r_s$ is defined by

$$r_s = r_c \left[ \frac{R\downarrow_{swc}^{max}}{0.03\ R\downarrow_{swc}^{max} + R\downarrow_{swc}(1-a_z)} + \left(\frac{\eta_{wilt}}{\eta_{root}}\right)^2 + P_{seas} \right] \tag{3.62}$$

while

$$r_a = \frac{1}{C_f U_{af}} \tag{3.63}$$

$R\downarrow_{sw_c}^{max}$ is the maximum incoming solar radiation at noon under clear skies, and $P_{seas}$ is a function of the time of year. $\eta_{wilt}$ is the value of soil moisture content, $\eta$, below which permanent wilting of the plant occurs. This is sometimes called the permanent wilting percentage given in $cm^3/cm^3$ and depends on soil type. $\eta_{root}$ is the minimum predicted value of soil moisture content occurring in the root zone of the plant. $r_c$ is a surface resistance of a canopy to losses of water and is a function of plant type. Equation 3.62 gives the parameterization for stomatal resistance. The squared term in 3.62 will sharply enhance the plant's stomatal resistance to moisture stress when the soil is dry.

To obtain the value of liquid water on the leaves, $w_L$, for equation 3.61, a conservation equation is used such that

$$\frac{\partial w_L}{\partial t} = LE_C' - E_{TR} \qquad 0 \leq w_L < w_I \tag{3.64}$$

$$\frac{\partial w_L}{\partial t} = 0 \qquad w_L = w_I \tag{3.65}$$

where $E_{TR}$ is the transpiration rate, whereby

$$E_{TR} = L_A \rho_a C_f U_{af} \left(\frac{r_s}{r_a + r_s}\right)\left[1 - \left(\frac{w_L}{w_I}\right)^{2/3}\right] / (q_{af} - q_s(T_f))$$

The transpiration rate represents the amount of water extracted from the root zone of the plant, and therefore was considered when predicting for the volumetric moisture content, $\eta$ (eq. 3.16). Equation 3.64 states that $w_L$ increases or decreases depending on the amount of condensation or evaporation onto or from the foliage.

Using the definitions listed above for each term in the canopy level energy balance (3.52), the foliage temperature, $T_f$, can be

found using the Newton-Raphson iteration method. When this is accomplished, the ground surface energy budget is solved for. The inclusion of vegetation will modify the ground surface energy balance (3.8) such that a weighting is made between bare ground fluxes and ground beneath a canopy fluxes. The modified surface energy balance is

$$(1-\sigma_f)[R\downarrow_{sw_c}(1-a_z-a_s) + R\downarrow_{Lw} + \rho c_p u_* \theta_* + \rho_{C_p} u_* q_* \tag{3.66}$$

$$- \varepsilon_G \sigma T_G^4] + \sigma_f[H^v + LE^v + R^v\downarrow_{Lw_G} - R^v\uparrow_{Lw_G}] - \lambda \left.\frac{\partial T_s}{\partial z}\right|_G = 0$$

The first set of bracketed terms are the bare soil shortwave, longwave, sensible heat and latent heat fluxes. The description of each of these terms and the method of solution were outlined in the last section. The second group of bracketed terms apply to the ground with canopy above it. $R^v\downarrow_{Lw_G}$ and $R^v\uparrow_{Lw_G}$, the longwave fluxes within the canopy, were defined by equations 3.48 and 3.49.

Surface sensible and latent heat fluxes beneath the canopy are determined from

$$H^v = \rho C_p C_G U_{af}(T_{af}-T_G)\left(\frac{1000\ mb}{P(mb)}\right)^{0.286} \tag{3.67}$$

$$LE^v = \rho L_c C_G U_{af}(q_{af}-q_G) \tag{3.68}$$

where $C_G$, the drag coefficient for a dense canopy (3.57) is assumed valid for the surface fluxes. The last term in 3.66 is the soil heat flux.

Once the vegetation and ground surface variables are updated, effective turbulent surface layer parameters are obtained by weighting between the bare soil and the plant values, i.e.

$$u'_* = (1-\sigma_f)u_* + \sigma_f u^v_* = (1-\sigma_f(u_*) + \sigma_f(C_G^{\frac{1}{2}}u_a) \tag{3.69}$$

$$\theta'_* = (1-\sigma_f)\theta_* + \sigma_f(\theta^c_* + \theta^v_*)$$

$$= (1-\sigma_f)\theta_* + \sigma_f[(1.1)(0.83)L_A(C_f(T_{af}-T_f)$$

$$+ 0.83C_G(T_{af}-T_f)](\frac{1000\ mb}{P(mb)})^{0.286} \tag{3.70}$$

$$q'_* = (1-\sigma_f)q_* + \sigma_f(q^c_* + q^v_*) = (1-\sigma_f)q_*$$

$$+ \sigma_f[0.83L_AC_f(q_{Af} - q(T_f))f' + 0.83C_G(q_{af}-q_G)] \tag{3.71}$$

$$L'_* = \theta\ u'^2_*/k_o g\theta'_* \tag{3.72}$$

where the unsuperscripted turbulent variables, $u_*$, $q_*$, and $\theta_*$ are the bare soil parameters defined by equations 3.9, 3.10, and 3.11. $u^c_*$, $q^c_*$, and $\theta^c_*$ are the turbulent variables at the canopy top and are defined from the canopy latent and sensible heat fluxes, equations 3.53 and 3.54, while $u^v_*$, $q^v_*$, and $\theta^v_*$ are the turbulent parameters within the vegetation and are taken from the in canopy heat fluxes, equations 3.67 and 3.68. $L'_*$ is the Monin-Obukhov length. $u'_*$, $\theta'_*$, $q'_*$, and $L'_*$ are used in similarity relationships to couple the surface and the atmosphere via turbulent exchange.

To summarize the computational sequence to calculate the subgrid scale fluxes when vegetation is present:

(1) Calculate the incident short- and long-wave radiation fluxes, $R\downarrow_{LwC}$ and $R\downarrow_{swc}$, at the canopy top and the radiation terms in the canopy energy balance, 3.52, which do not depend on $T_f$. These are the first three terms in 3.52.

(2) Calculate $U_{af}$, $C_f$, $r_s$, and $r_a$ from 3.56, 3.55, 3.62, and 3.63.

(3) Calculate $q_s(T_f)$, and $T_{af}$.

(4) Determine $q_{af}$ with 3.59. Use this value to determine if condensation is occurring on the leaf, in which case $\delta_w$ equals 1. Then $f'$ can be determined from 3.61.

(5) $q_f$ is updated with 3.60. Then $q_{af}$ is updated again.

(6) Compute $H'_c$ and $LE'_c$ using 3.53 and 3.54.

(7) Solve the foliage energy balance, 3.52, for $T_f$ using the Newton-Raphson iteration scheme.

(8) Update $q_s(T_f)$, $LE'_c$, and $E_{TR}$. $E_{TR}$ is updated using 3.65.

(9) Update $w_L$ from 3.64.

(10) Compute the ground fluxes beneath the canopy, $R{\downarrow}^{v}_{lw_G}$, $R{\uparrow}^{v}_{Lw_G}$, $H^v$, using 3.48, 3.49, and 3.67.

(11) Solve for the soil moisture parameters as outlined in Section 3.2.3(A).

(12) With the updated calculation of $q_G$ from step (11), update the moisture flux from the ground beneath the canopy, $LE^v$ from 3.68.

(13) Solve for $T_G$ from the ground surface energy balance modified for the presence of vegetation, equation 3.66.

(14) Determine the effective turbulent variables, $\theta'_*$, $q'_*$, $u'_*$, and $L'_*$, from 3.67, 3.70, 3.71, and 3.72.

## 3.3 Advection and Diffusion

Numerical solution of the predictive equations is accomplished first by including advection, then diffusion. The upstream interpolated cubic spline approximation described by Mahrer and Pielke (1978) is utilized to evaluate advection. The vertical exchange terms

in both the atmosphere and soil are evaluated using a forward-weighted Crank-Nicolson scheme as proposed by Paegle et al. (1976).

An explicit horizontal diffusion scheme is used on all the atmospheric prognostic variables in order to eliminate spurious energy generated from aliasing. The horizontal exchange coefficient is the one used by Pielke (1974) and is proportional to the deformation of the horizontal wind field and a predetermined constant, $\alpha$. The form of the exchange coefficient is:

$$K_H = \alpha(\Delta N_x)(\Delta N_y)[(\frac{\partial v}{\partial x} + \frac{\partial u}{\partial y})^2 + \tfrac{1}{2}((\frac{\partial u}{\partial x})^2 + (\frac{\partial v}{\partial y})^2)]^{\frac{1}{2}} \qquad (3.73)$$

where $\Delta N_x$ and $\Delta N_y$ are the x and y grid lengths, respectively.

## 3.4 Boundary Conditions

At the lateral boundaries of the model domain, zero gradient boundary conditions are specified for u, v, $\Theta$, q and pressure. At the ground, a no-slip condition is imposed on velocity. The upper boundary is a material surface whose height is predicted as outlined in Mahrer and Pielke (1977). On this surface, the prognostic variables are held constant.

Figure 3.1 shows the extent of the horizontal model grid over South Florida. A uniform horizontal grid spacing of 11 km is used in the interior of the domain. The grid is stretched near the boundaries such that the grid spacing is increased to 22 km, 44 km, and 88 km at the three closest grids to the boundaries. This is done to reduce the effect of the edge on the solution.

Characteristic soil parameters and the initial soil moisture content for the soil textural classes used in the South Florida simulations are given in Table 3.2. Vegetation parameters are shown in Table 3.3. The roughness length over land was 4 cm.

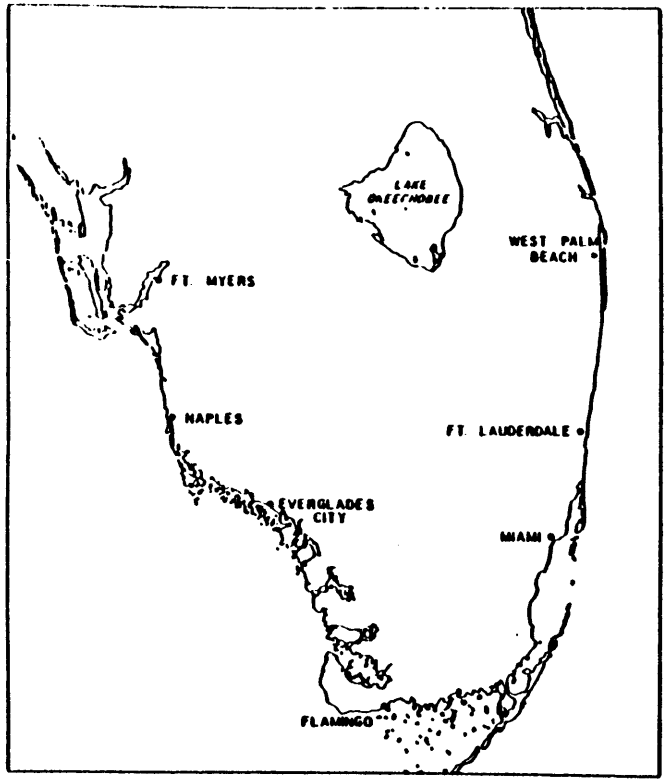


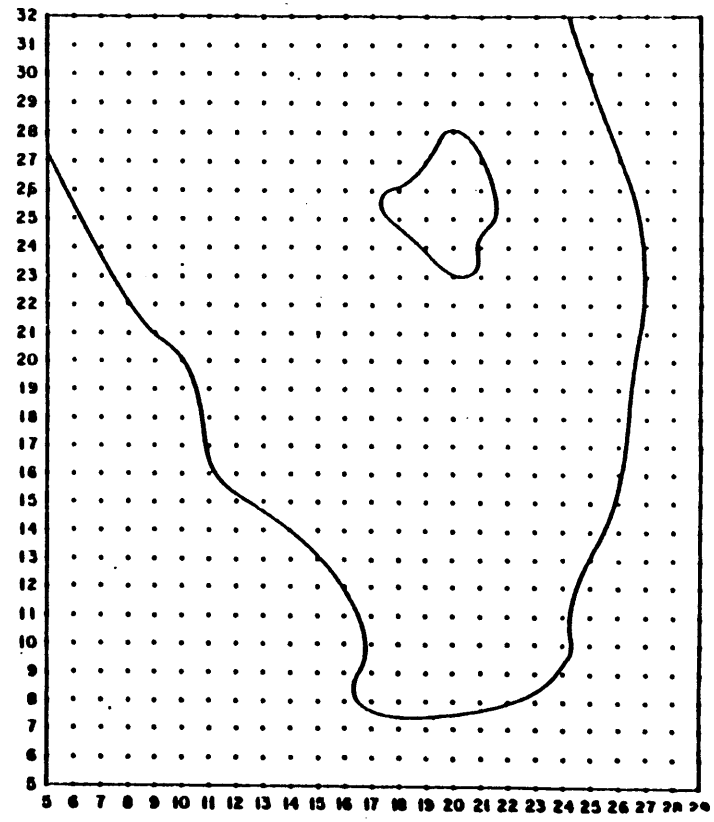

Figure 3.1. (a) Outline of the model domain, and
(b) Computational grid for the South Florida simulations.

Table 3.2. Soil parameters for the soil types used in the South Florida simulations (taken from McCumber, 1980).

| Soil Type | $\eta_s$ ($cm^3/cm^3$) | $\psi_s$ (cm) | $K_{\eta s}$ (cm/sec) | b -- | $\eta_{wilt}$ ($cm^3/cm^3$) | $C_i$ (cal/cm/°C) | $\varepsilon_G$ | $\eta$ ($cm^3/cm^3$) | % Saturation |
|---|---|---|---|---|---|---|---|---|---|
| Sand | .395 | -12.1 | .01760 | 4.05 | .0677 | .350 | 1.0 | .07 | 18% |
| Sandy Loam | .435 | -21.8 | .00341 | 4.90 | .1142 | .321 | 1.0 | .17 | 39% |
| Sandy Clay | .426 | -15.3 | .00022 | 10.40 | .2193 | .281 | 1.0 | .27 | 63% |
| Peat | .863 | -35.6 | .00080 | 7.75 | .3947 | .200 | 1.0 | .58 | 67% |
| Marsh | .863 | -35.6 | .00080 | 7.75 | .3947 | .200 | 1.0 | .86 | 100% |

Table 3.3. Vegetation parameters for grass and trees used in the South Florida simulation (from McCumber, 1980).

| | Grass | Trees |
|---|---|---|
| Emissivity ($\varepsilon_f$) | 0.95 | 0.98 |
| Albedo ($a_f$) | 0.20 | 0.10 |
| Resistance Coefficient ($r_c$, sec/cm) | 4.00 | 8.00 |
| Transfer Coefficient ($C_G$) | 0.0038 | 0.0176 |
| Interception Storage ($W_I$, cm) | 0.06 | 0.16 |
| Displacement Height (D, m) | 1.14 | 15.20 |

## 3.5 Initialization

Three-dimensional simulations were performed for all the synoptic flow categories summarized in Table 2.2 which contained three or more satellite collect days; light southeast, strong southeast, strong east, and very light and variable. A strong southwesterly flow simulation was also performed, even though only one collect day was available. Model runs with the inclusion of the ground surface parameterization described for these synoptic flow regimes were not performed previously.

The soil layer contains 14 levels extending from the surface to a depth of 1 m. Its initial temperature and moisture perturbation profiles from the surface value as well as the root distribution function, R(z), are shown in Table 3.4. The initial soil profiles were assumed the same for the various synoptic class simulations. These same profiles were used for all soil grid columns. Table 3.4 shows that initially the soil moisture content is equal to its surface value at all levels in the soil. McCumber states that the soil moisture was initialized in this way since no data was available for this profile.

Also equivalent for the five simulations was the value of the weighting coefficient, $\alpha$, for horizontal diffusion, $\alpha$. It was chosen equal to 0.65. This value eliminated much of the spurious $2\Delta x$ noise while reducing the amplitude of the truly physical features very little. Other constants needed to initialize the model are shown in Table 3.5.

As discussed in Section 2.2., the 12 GMT (7 EST) rawinsonde data was averaged for all the days in each of the synoptic classes. The

atmospheric constants needed for initialization of the synoptic classes are given in Table 3.6. The vertical profiles of $\theta$, q, u, v for the 14 atmospheric levels extending to 5 km above the ground are given in Table 3.7. Initially the atmosphere is assumed barotropic so these profiles are valid for all atmospheric grid columns. u and v were specified from the averaged soundings for all the model levels above the initial planetary boundary height. In the boundary layer, a balance is prescribed between the pressure gradient, Coriolus and friction forces.

Table 3.4. Initial vertical profile of soil temperature ($\Delta T_s$) and soil moisture ($\Delta\eta$) perturbations from the surface values and of the root distribution function (R(z); z is depth in cm).

| Level | z (cm) | $\Delta T_s$ (°C) | $\Delta\eta$ | R(z) |
|---|---|---|---|---|
| 14 | 0.0 | 0.0 | 0.0 | 0.000 |
| 13 | 0.5 | 0.08 | 0.0 | 0.036 |
| 12 | 1.5 | 0.41 | 0.0 | 0.073 |
| 11 | 3.0 | 0.85 | 0.0 | 0.073 |
| 10 | 5.0 | 1.85 | 0.0 | 0.109 |
| 9 | 8.0 | 1.68 | 0.0 | 0.145 |
| 8 | 12.0 | 1.57 | 0.0 | 0.145 |
| 7 | 18.0 | 2.86 | 0.0 | 0.146 |
| 6 | 26.0 | 3.90 | 0.0 | 0.182 |
| 5 | 36.0 | 4.15 | 0.0 | 0.091 |
| 4 | 48.0 | 4.46 | 0.0 | 0.000 |
| 3 | 62.0 | 3.20 | 0.0 | 0.000 |
| 2 | 79.0 | 2.18 | 0.0 | 0.000 |
| 1 | 100.0 | 1.95 | 0.0 | 0.000 |

Table 3.5. Constants needed to initialize the model. These constants were the same for all the various synoptic class simulations.

| | |
|---|---|
| Mean Latitude | 26°N ($f = 6.38 \times 10^{-5}\ s^{-1}$) |
| Day of Year | July 17 |
| Model Start-up Time | Sunrise (5:28 a.m. EST) |
| Program Run Time | 24 hours |
| Grid Spacing ($\Delta x$) | 11 km |
| Time Step | 90 sec |
| Weighting Coefficient for Horizontal Diffusion ($\alpha$) | 0.65 |
| Roughness Length, Land | 4 cm |

Table 3.6. Atmospheric constants needed for model initialization for the five synoptic class simulations based on a composite analysis of synoptic rawinsonde data described in Chapter 4.

| Synoptic Class | Geostrophic Wind Speed (m/s) | Geostrophic Wind Direction | Synoptic Surface Pressure (mb) | Synoptic Surface Temperature (°K) | Synoptic Height of Planetary Boundary Layer (m) | Initial Surface Specific Humidity (g/kg) |
|---|---|---|---|---|---|---|
| Light Southeast | 2.4 | 150° | 1017 | 297.1 | 200 | 17.6 |
| Strong Southeast | 5.7 | 150° | 1017 | 298.1 | 200 | 17.7 |
| Strong East | 5.8 | 100° | 1017 | 299.3 | 200 | 18.0 |
| Very Light and Variable | 0.3 | 150° | 1018 | 299.3 | 200 | 19.2 |
| Strong Southwest | 4.2 | 225° | 1013 | 296.5 | 550 | 18.3 |

Table 3.7. Initial atmospheric vertical profiles of potential temperature (θ) in °K, specific humidity (g) in g/kg), and the u and v components of velocity in m/s. z is in m. These composites were derived by using the methods described in Section 2.2.

| | | Light Southeast | | | | Strong Southeast | | | | Strong East | | | | Very Light and Variable | | | | Strong Southwest | | | |
|---|---|---|---|---|---|---|---|---|---|---|---|---|---|---|---|---|---|---|---|---|---|
| Level | z | θ | q | u | v | θ | q | u | v | θ | q | u | v | θ | q | u | v | θ | q | u | v |
| 1 | 25.0 | 297.5 | 17.8 | -1.3 | 1.7 | 298.3 | 17.9 | -3.1 | 3.2 | 299.5 | 18.1 | -4.5 | -0.4 | 299.4 | 19.3 | -.20 | 0.2 | 296.8 | 0.0183 | 1.32 | 0.75 |
| 2 | 50 | 298 | 18.0 | -1.4 | 1.8 | 298.6 | 18.1 | -3.3 | 3.4 | 299.6 | 18.2 | -4.8 | -0.3 | 299.6 | 19.3 | -.26 | 0.3 | 297.1 | 0.0182 | 1.35 | 0.75 |
| 3 | 100 | 299 | 18.5 | -1.4 | 1.9 | 299.2 | 18.4 | -3.4 | 3.7 | 300.0 | 18.3 | -5.1 | -0.2 | 299.9 | 19.5 | -.1 | 0.3 | 297.7 | 0.0181 | 1.40 | 0.75 |
| 4 | 200 | 299.7 | 17.8 | -1.2 | 2.1 | 299.8 | 17.5 | -2.8 | 4.9 | 300.4 | 17.8 | -5.7 | 1.0 | 300.2 | 18.6 | -0.1 | 0.3 | 299.4 | 0.0172 | 1.57 | 1.04 |
| 5 | 500 | 300.8 | 14.2 | -0.7 | 1.7 | 301.3 | 14.8 | -1.2 | 2.9 | 301.3 | 15.7 | -3.7 | 1.7 | 301.6 | 14.2 | -2.7 | 2.5 | 301.6 | 0.0154 | 1.93 | 1.76 |
| 6 | 1000 | 302.7 | 12.3 | -0.6 | 1.6 | 303.3 | 11.9 | -1.3 | 2.8 | 302.8 | 12.4 | -3.6 | 1.5 | 303.8 | 9.9 | -2.7 | 1.9 | 303.2 | 0.0135 | 2.38 | 2.64 |
| 7 | 1500 | 305.0 | 10.8 | -0.9 | 1.5 | 305.3 | 9.3 | -1.3 | 2.7 | 304.9 | 10.7 | 3.0 | 0.5 | 307.3 | 7.5 | -1.8 | 1.4 | 305.0 | 0.0117 | 2.53 | 2.60 |
| 8 | 2000 | 307.2 | 8.9 | -0.7 | 1.1 | 307.1 | 8.0 | -1.4 | 2.8 | 307.1 | 9.1 | -3.1 | 0.2 | 309.8 | 6.7 | -1.2 | 1.8 | 307.2 | 0.0100 | 2.32 | 1.37 |
| 9 | 2500 | 309.2 | 7.7 | -0.1 | 1.1 | 309.3 | 6.8 | -1.5 | 2.4 | 309.5 | 7.3 | -2.5 | 0.5 | 311.9 | 5.9 | -0.5 | 2.2 | 309.3 | 0.0083 | 2.09 | 0.14 |
| 10 | 3000 | 311.4 | 6.2 | 0.3 | 1.1 | 311.5 | 5.5 | -1.1 | 2.4 | 311.9 | 5.7 | -2.2 | 0.2 | 313.6 | 5.0 | -1.8 | 1.7 | 311.5 | 0.0068 | 1.95 | -0.73 |
| 11 | 3500 | 313.5 | 5.6 | 1.0 | 0.7 | 313.7 | 4.7 | -0.6 | 2.4 | 314.5 | 4.3 | -1.7 | -0.3 | 313.6 | 3.4 | -1.5 | 2.2 | 313.8 | 0.0065 | 2.20 | 0.15 |
| 12 | 4000 | 315.9 | 4.5 | 1.7 | 1.0 | 315.9 | 3.8 | -0.1 | 1.8 | 316.4 | 3.8 | -1.2 | -0.7 | 315.5 | 3.1 | -0.8 | 2.7 | 316.1 | 0.0062 | 2.45 | 1.03 |
| 13 | 4500 | 318.9 | 3.4 | 2.2 | 0.6 | 318.4 | 3.7 | 1.0 | 1.2 | 318.5 | 3.1 | -1.0 | -0.9 | 317.9 | 2.9 | -1.0 | 1.3 | 319.4 | 0.0052 | 2.71 | 1.92 |
| 14 | 5000 | 319.3 | 3.4 | 2.4 | 0.5 | 319.6 | 3.2 | 1.2 | 1.1 | 319.7 | 2.4 | -0.9 | -1.2 | 319.0 | 2.5 | -1.2 | 1.2 | 320.7 | 0.0048 | 2.84 | 2.37 |

# CHAPTER 4

# DESCRIPTION OF THE THERMODYNAMIC AND KINEMATIC SYNOPTIC ENVIRONMENT

## 4.1. Qualitative Results

In order to determine the importance of the synoptic scale environment on controlling the amount of deep convective clouds over the South Florida peninsula, the percent of convective cloudiness was compared qualitatively to the averaged quantities of:

(1) $\Delta P$; $\Delta\overline{\theta_e}$; $\overline{\theta_{es}-\theta_e}$; and 200 mb wind speed.

(2) The vertical profiles of wind speed and direction; $\theta_e$; $\theta_{es}$ and $\theta_{es}-\theta_e$.

for the light southeast, strong southeast, strong east, light and variable, and strong southwest synoptic flow categories; and for all synoptically undisturbed and all disturbed cases combined. These variables were defined in Section 2.2. The differences in these variables for each category will help define the synoptic environment for each category and also partly explain the observed differences in the amount of convective cloudiness noted from the cloud composites.

Figure 4.1 shows a time series of the percent of deep convective cloudiness over the South Florida peninsula for the synoptic classes listed above. The percent coverage of deep convection normalized by area for a satellite image was obtained using the procedure described in Section 2.1. The mean was found by averaging the percent of deep

Figure 4.1. Time series of the averaged percent of deep convective clouds for the hours for which satellite data was collected for the synoptic classes: (a) light southeast, (b) strong southeast, (c) strong east, (d) light and variable, (e) undisturbed, and (f) disturbed. The error bars corresponding to one standard deviation around the mean are given for the mean quantities at 0800, 1000, 1200, 1400, 1600, and 1800 EST.

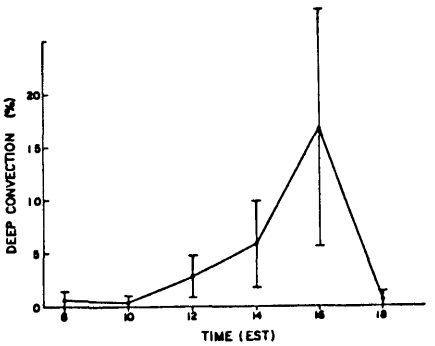
DEEP CONVECTION (%)
0
5
10
15
20
6
10
12
14
16
18
TIME (EST)

(a)

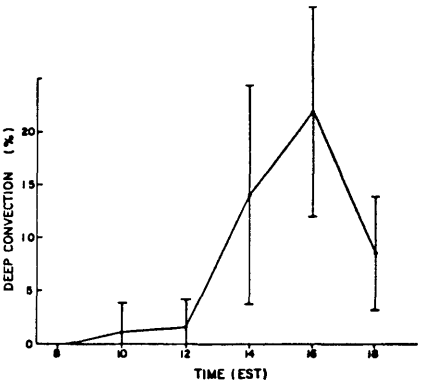
DEEP CONVECTION (%)
0
5
10
15
20
6
10
12
14
16
18
TIME (EST)

(b)

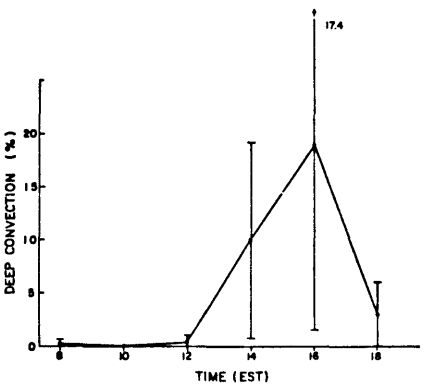
17.4
DEEP CONVECTION (%)
0
5
10
15
20
6
10
12
14
16
18
TIME (EST)

(c)

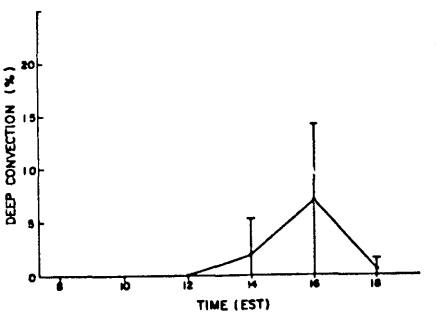
DEEP CONVECTION (%)
0
5
10
15
20
6
10
12
14
16
18
TIME (EST)

(d)

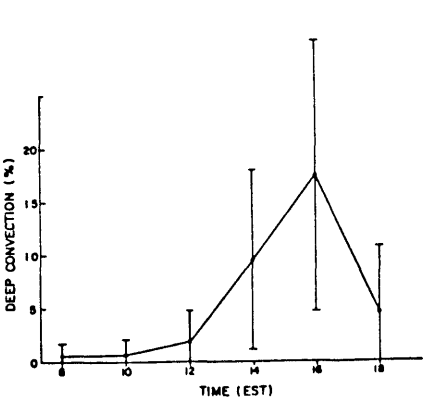
DEEP CONVECTION (%)
0
5
10
15
20
6
10
12
14
16
18
TIME (EST)

(e)

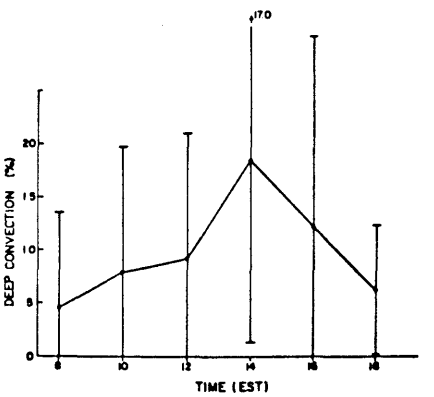
17.0
DEEP CONVECTION (%)
0
5
10
15
20
6
10
12
14
16
18
TIME (EST)

(f)

convective clouds for all of the satellite images that fell into the particular synoptic class. An error bar corresponding to one standard deviation on either side of the mean is given for all of the plotted points. Statistically significant differences between means will be defined when there is a difference of at least two standard deviations.

For all the synoptically undisturbed categories presented, the peak percentage of deep convective clouds occurs at 1600 EST. Through 1200 EST for each undisturbed category, well developed convection was less than 4 percent. For the undisturbed class, the average was less than 1.9 percent at 1200 EST but increased rapidly two hours later to 9.5 percent.

Deep convective clouds on disturbed days are more prevalent in the morning and reach a maximum two hours earlier (i.e. at 1400 EST) as compared to the average for the undisturbed days. The diurnal cycle is seen in all the plots as the percentage drops off sharply toward evening.

As seen in Figure 4.1, each synoptic flow category exhibits similar patterns in the amount of deep convective cloudiness present during the day. The most noticeable differences come when comparing magnitudes. Light and variable flow has a much lower percentage during the afternoon as compared to the other classes. Strong south-easterly flow has the highest amounts of deep convective clouds during the afternoon hours. The variance in the means is high for all the plots since the standard deviations are greater than 50 percent of the mean for each of the afternoon hours for each synoptic class. The only statistically significant difference between classes is the

afternoon percentage difference between the light and variable class and the other classes.

Table 4.1 shows the averaged values for each synoptic class for several of the thermodynamic variables defined in Section 2.2, wind speed at 200 mb, and the percent deep convective cloudiness averaged for all the times of the day. The standard deviation, $\sigma$, and coefficient of variation, $\sigma/\bar{x}$, are given for each mean quantity, $\bar{x}$. The coefficient of variation is normalized by the mean so that the variance of each mean from one category to another can be directly compared. The synoptic categories in Table 4.1 are listed in order from most to least convectively active. For the daily average, strong southeasterly is the most convectively active undisturbed class with a value of 7.9 percent. Light and variable wind days are the least with 1.6 percent, which is 4.2 percent less than the undisturbed average. The disturbed category has statistically significant more deep convection than the undisturbed class, as expected.

The coefficients of variation are high for each class. However, except for the light and variable class, each flow category has a smaller or comparable coefficient of variation when compared to that for the combined undisturbed days average. The coefficient of variation is reduced by as much as 50 percent for strong southeasterly flow as compared to coefficient calculated for the all undisturbed days average. Implications can be drawn from this that the synoptic flow has some control although weak on the daily amount of deep convective activity over the Florida peninsula on synoptically undisturbed days.

The depth of convective instability, $\Delta P$, is similar for all synoptic categories with strong southwesterly flow having the smallest

Table 4.1. The daily averaged percent of deep convection over the South Florida peninsula for each synoptic class. Synoptic classes are listed from most to least convectively active. Also given for each class are the average value of the depth and magnitude of convective instability, $\Delta P$ and $\Delta\overline{\theta}_e$, the magnitude of moisture deficiency $\overline{\theta_{es}-\theta_e}$, and wind speed at 200 mb. The standard deviation, $\sigma$, and coefficient of variation $(\sigma/\bar{x})$ are given for each averaged quantity $(\bar{x})$. The number in parentheses is the number of soundings available for that class.

| Synoptic Class (Number of Collect Days) | Percent of Deep Convect. | | | $\Delta P$ MB | | | $\Delta\overline{\theta}_e$ (°K) | | | $\overline{\theta_{es}-\theta_e}$ (°K) | | | Speed at 200 mb (m/s) | | |
|---|---|---|---|---|---|---|---|---|---|---|---|---|---|---|---|
| | $\bar{x}$ | $\sigma$ | $\sigma/\bar{x}$ | $\bar{x}$ | $\sigma$ | $\sigma/\bar{x}$ | $\bar{x}$ | $\sigma$ | $\sigma/\bar{x}$ | $\bar{x}$ | $\sigma$ | $\sigma/\bar{x}$ | $\bar{x}$ | $\sigma$ | $\sigma/\bar{x}$ |
| 1 Disturbed (6) | 9.3 | 13.6 | 1.3 | 420.5 | 70.3 | 0.2 | 3.6 | 2.5 | 0.7 | 7.8 | 2.4 | 0.3 | 13.0 | 7.7 | 0.6 |
| 2 Strong Southeast (7) | 7.9 | 5.1 | 0.6 | 415.1 | 46.0 | 0.1 | 5.0 | 1.5 | 0.3 | 10.0 | 2.3 | 0.2 | 13.5 | 10.8 | 0.8 |
| 3 All Undisturbed Days (28) | 5.8 | 5.3 | 0.9 | 428.0 | 54.4 | 0.1 | 3.9 | 2.1 | 0.5 | 9.7 | 4.7 | 0.4 | 13.4 | 9.0 | 0.7 |
| 4 Strong East (7) | 5.4 | 5.1 | 0.9 | 440.8 | 46 | 0.1 | 4.9 | 2.6 | 0.5 | 8.7 | 3.4 | 0.4 | 14.6 | 7.0 | 0.5 |
| 5 Light Southeast (6) | 5.4 | 4.1 | 0.8 | 469.7 | 59.6 | 0.1 | 2.4 | 1.0 | 0.4 | 8.2 | 2.7 | 0.3 | 14.5 | 13.9 | 1.0 |
| 6 Light and Variable (4) | 1.6 | 2.0 | 1.3 | 418.0 | 52 | 0.1 | 2.4 | 2.0 | 0.8 | 14.2 | 8.3 | 0.5 | 14.3 | 6.2 | 0.4 |
| 7 Strong Southwest (1) | | -- | | 373 | -- | -- | 4.9 | -- | -- | 5.3 | -- | -- | 13.5 | -- | -- |

depth and light southeasterly, the largest, although the differences are only slightly significant. The larger the value of the magnitude of convective instability, $\overline{\Delta\theta_e}$, the greater is the thermal instability. The values for the light and variable and the light southeasterly flow regimes show a more stable environment relative to the other classes. However, the coefficient of variation for the light and variable class is greater than for all the undisturbed days by 0.3, indicating that its value is less significant compared to the other categories. The undisturbed and disturbed categories have nearly equivalent thermal stabilities. The averaged wind speed at 200 mb shows only slight differences.

The magnitude of moisture deficiency through the layer of convective instability, $\overline{\theta_{es}-\theta_e}$, is defined so that the more positive its value, the less moisture is available in the layer. Of note is the very dry environment indicated for the light and variable class. The other classes have similar values except that of strong southwesterly flow which indicates a relatively moister environment. A value of 9.7 for the undisturbed class reveals a drier environment than the disturbed class with a value of 7.8. However, the statistical significance is only marginal. The coefficient of variation for all the flow classes, except for light and variable flow which is only slightly higher, are lower than the undisturbed class value. This would imply that the direction and strength of the synoptic flow also controls, to some extent, the amount of available moisture in the lower troposphere.

To further describe the environment for each synoptic category, vertical plots of several of the variables are presented from

Figure 4.2. Wind hodographs for synoptic classes: (a) light southeast, (b) strong southeast, (c) strong east, and (d) light and variable. Speed is in m/s. The individual winds which made up the means are plotted at 850 (Δ), 700 (O), 500 (X), 300 (□), and 200 (O) mb.

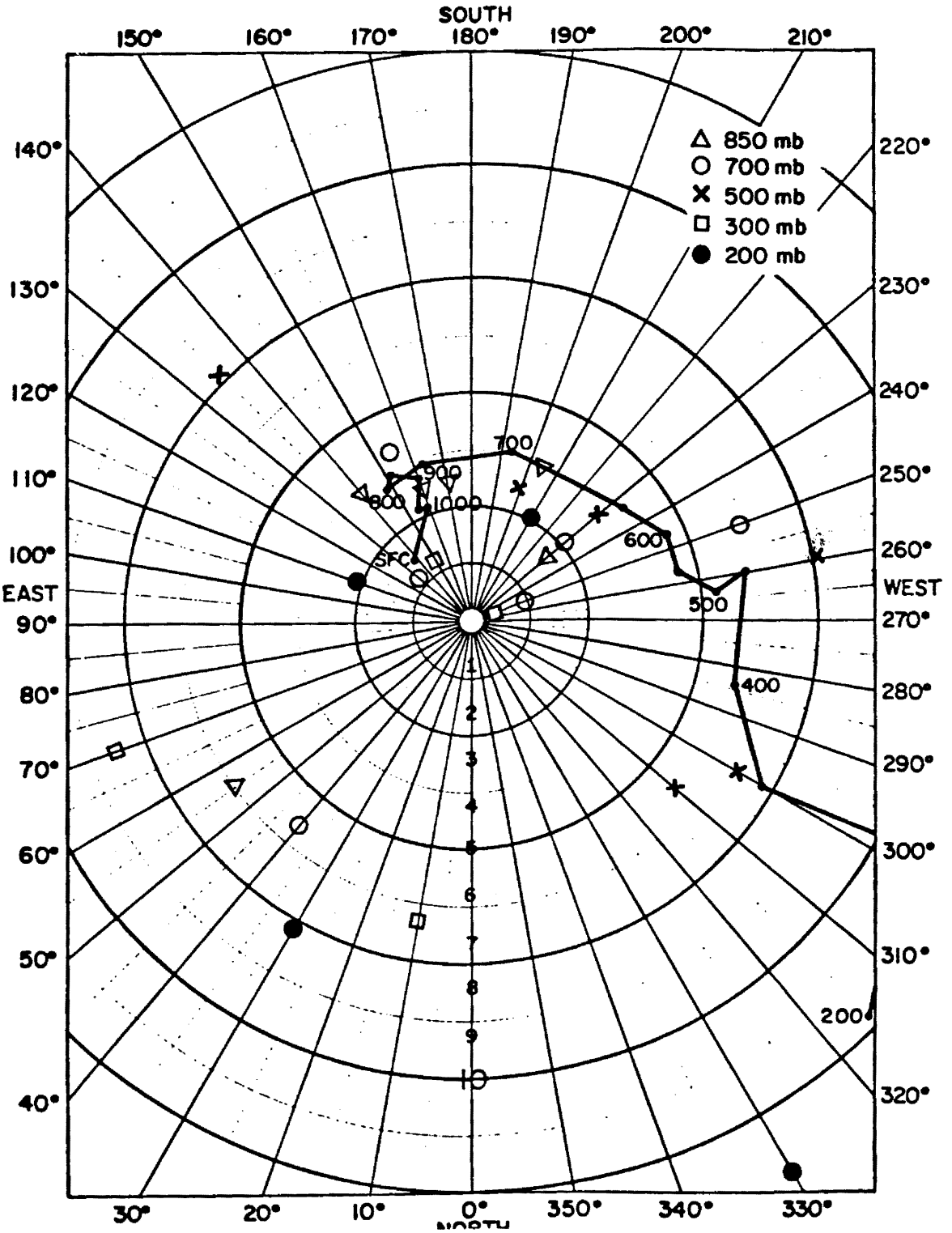


a. Light southeast

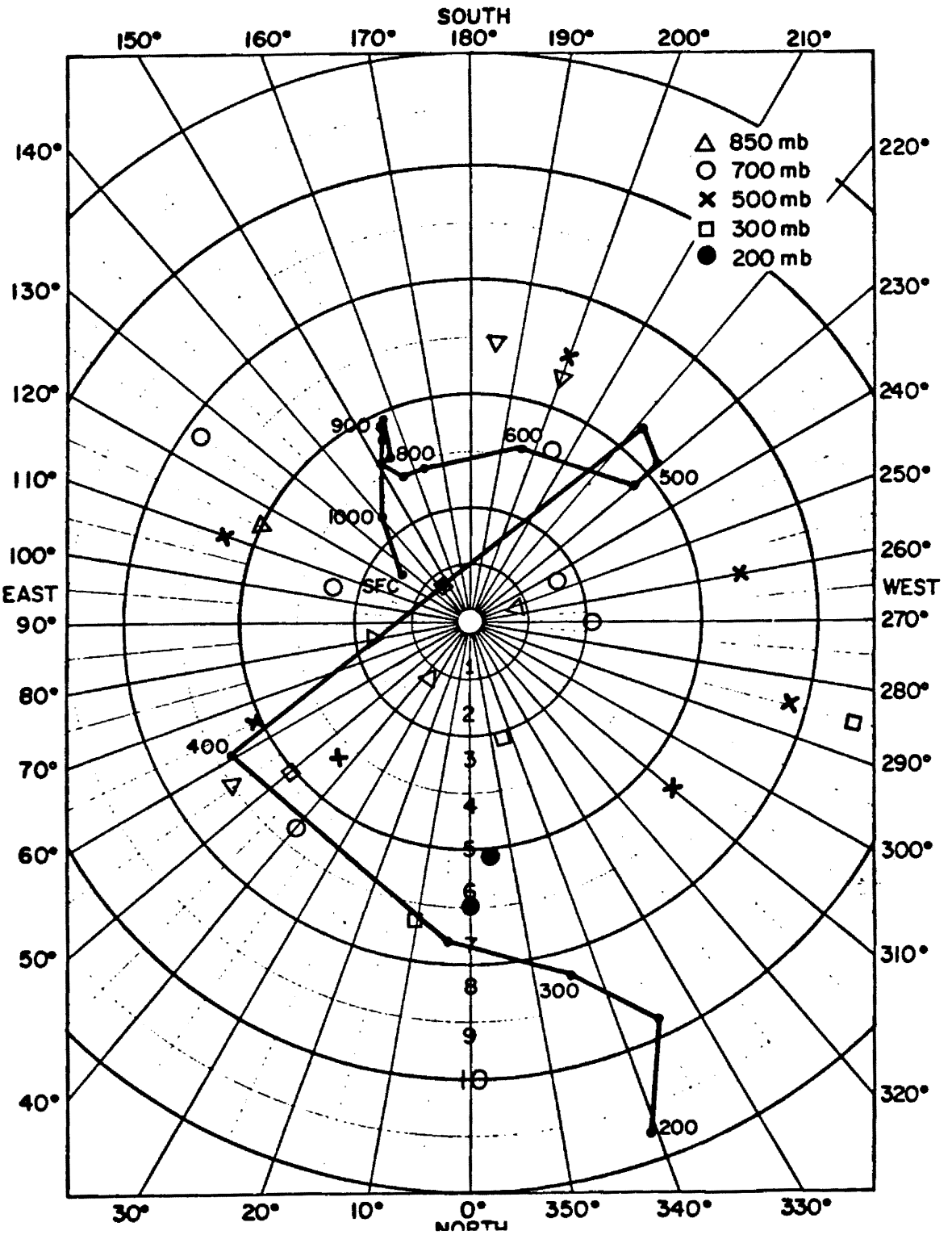


b. Strong southeast

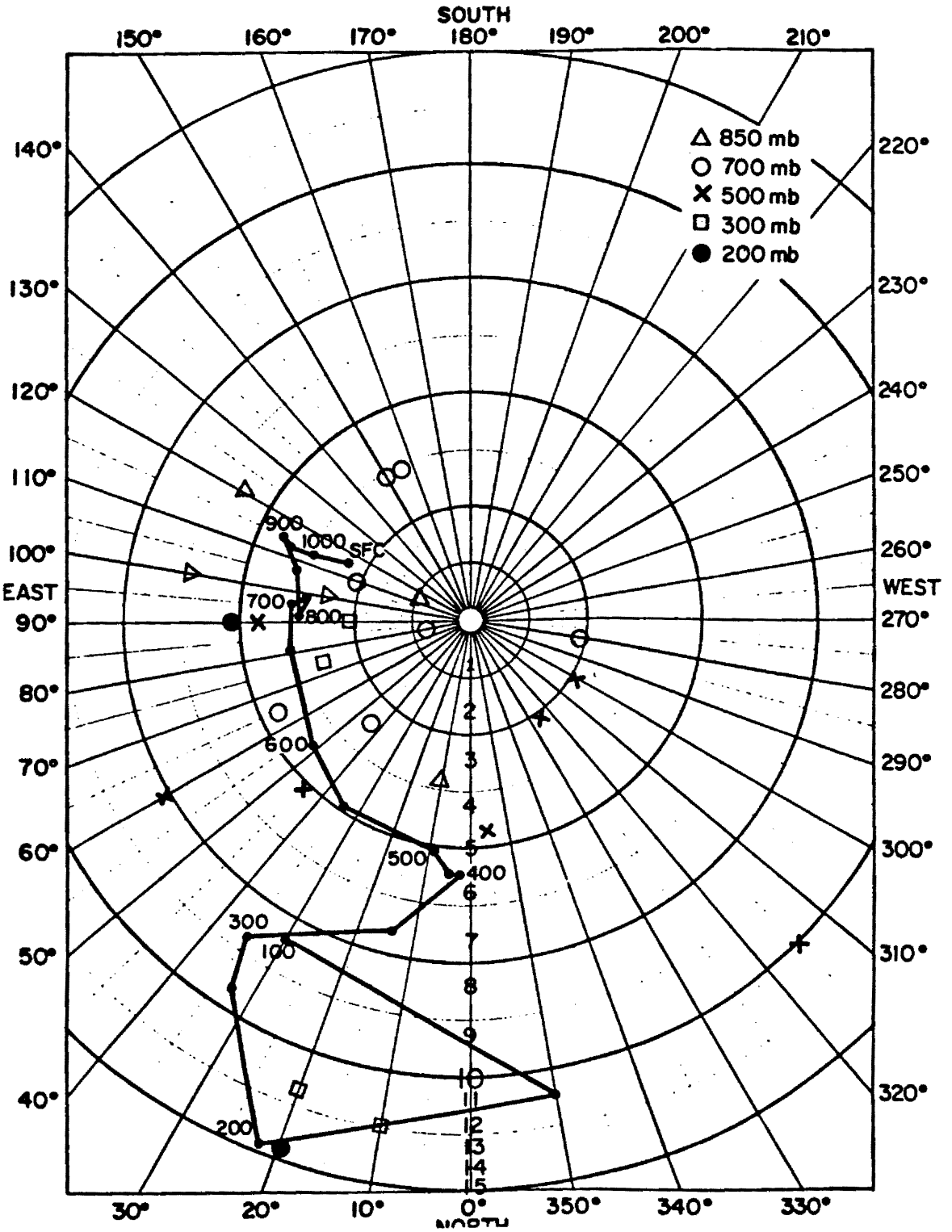


c. Strong east

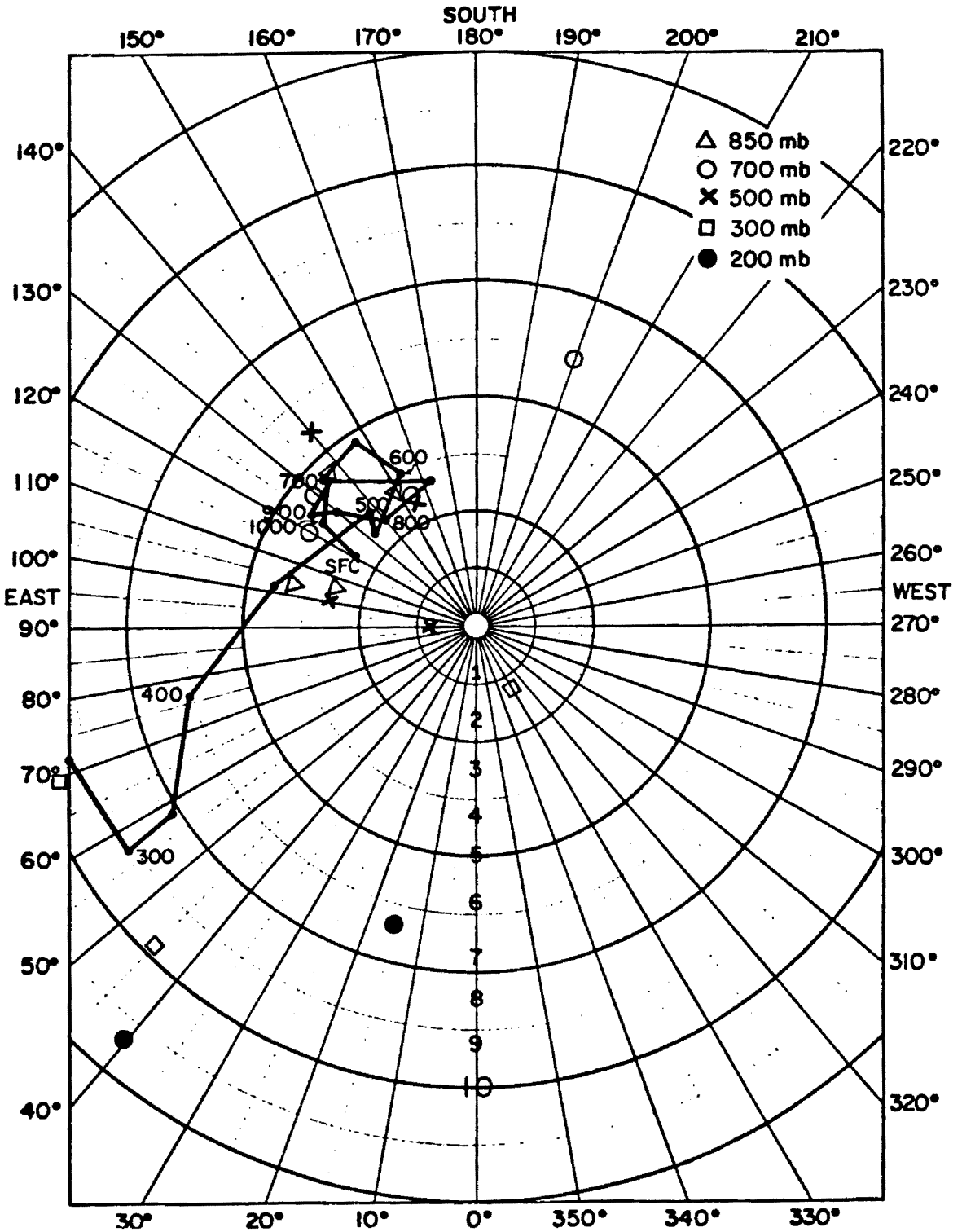


d. Light and variable

Figure 4.3. Wind hodographs for synoptic classes: (a) strong southwest and (b) disturbed synoptic class. Speed is in m/s. The individual winds which made up the means are plotted at 850 (Δ), 700 (O), 500 (X), 300 (□), and 200 (↓) mb.

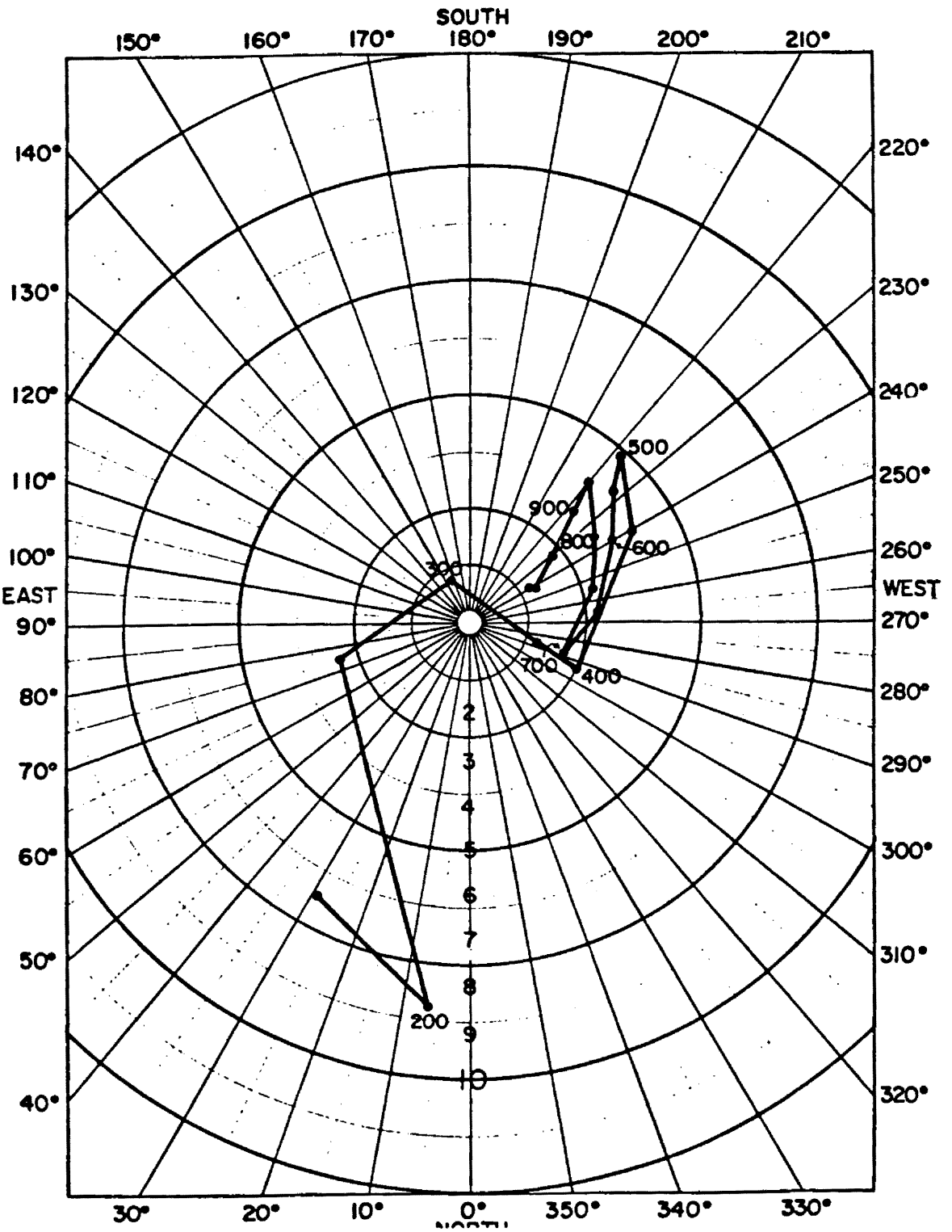


a. Strong southwest

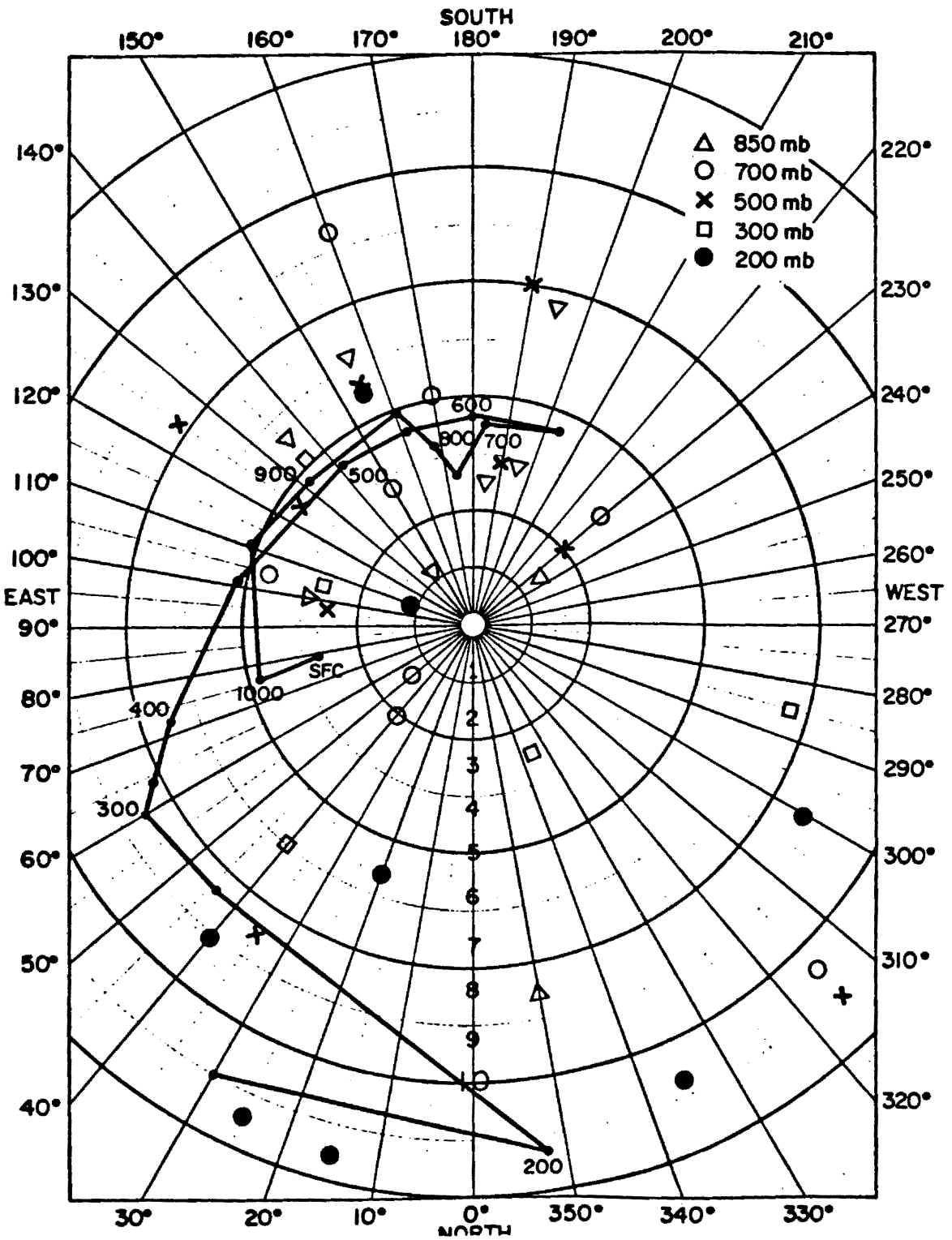
SOUTH
150°
160°
170°
180°
190°
200°
210°
140°
130°
120°
110°
100°
EAST
90°
80°
70°
60°
50°
40°
220°
230°
240°
250°
260°
WEST
270°
280°
290°
300°
310°
320°
30°
20°
10°
0°
NORTH
350°
340°
330°
850 mb
700 mb
500 mb
300 mb
200 mb
600
800
700
900
500
SFC
1000
400
300
200
1
2
3
4
5
6
7
8
9
10

b. Disturbed

averaging the Key West and West Palm Beach, Florida, soundings. Wind hodographs are shown in Figs. 4.2 and 4.3. A measure of variability for the hodographs are given by a scatter plot of the individual winds which made up the mean at several sounding levels. Wind direction for a point is found by drawing a vector from the origin to the point, then extending a line along the vector to the graph label and reading the direction in degrees. Statistics for wind speed are given in Table 4.2 for several sounding levels.

Both southeasterly class profiles have southeasterly winds through the lower troposphere. The strong southeasterly class profile (Fig. 4.2b) increases in speed remaining southeasterly from the surface to 700 mb while the light southeasterly flow class (Fig. 4.2a) stays fairly constant in direction but increases in speed to 800 mb. Above this, winds veer toward the northwest for the light southeasterly class. Above 500 mb winds back toward the northeast and then northwest for the strong southeasterly class. From the thermal wind relationship, veering winds with height indicate warm advection aloft in the layer producing a less favorable environment for convection. This is the case for the light southeasterly class while for the strong southeasterly class a destabilizing influence is present with cold advection above 500 mb. The strong easterly class increases in speed remaining out of the east-southeast to 900 mb. Above this level, the winds back toward the north indicating cold advection through much of the troposphere.

For all three classes, above 500 mb, greater variations in the mean wind exist as shown from the scatter plots and the standard deviations for wind speed in Table 4.2. The means for the light

southeasterly and strong easterly classes have less variance at lower levels than do the winds at the same level for strong southeasterly flow.

Light and variable winds vary back and forth in direction ranging from 120° to 160° from the surface to 500 mb. Speeds also vary in intensity through this layer. Above this, height winds back consistently to the east-northeast and increase rapidly in speed. Both of these tendencies indicate cold advection. The winds for this case have relatively little variance throughout most of the troposphere.

Wind directions for the strong southwest synoptic class (Fig. 4.3a) remain out of the southwest from the surface to 850 mb, then vary back and forth from 850 mb to 400 mb ranging from 220° to 290° through that layer. Above this height, winds back strongly toward the north-northeast indicating cold advection aloft.

Figure 4.3b shows the wind hodograph for the disturbed class. The undisturbed class is not shown since it is made up of a wide range of directions although it is dominated by southeasterly flow days. Winds generally retain an easterly component through the depth of the troposphere. Wind direction begins to vary greatly above 1000 mb veering from 1000 mb to 650 mb from the east-northeast to the south. The wind shear is also large at mid and upper levels for the disturbed class as winds begin to back above 650 mb signifying cold advection. However, the variance in the winds is significant for all levels.

Total wind speed with height is presented in Fig. 4.4. The light southeasterly and strong southwesterly classes plots indicate lighter speeds in the lowest 100 mb. Aloft, speeds are quite similar except

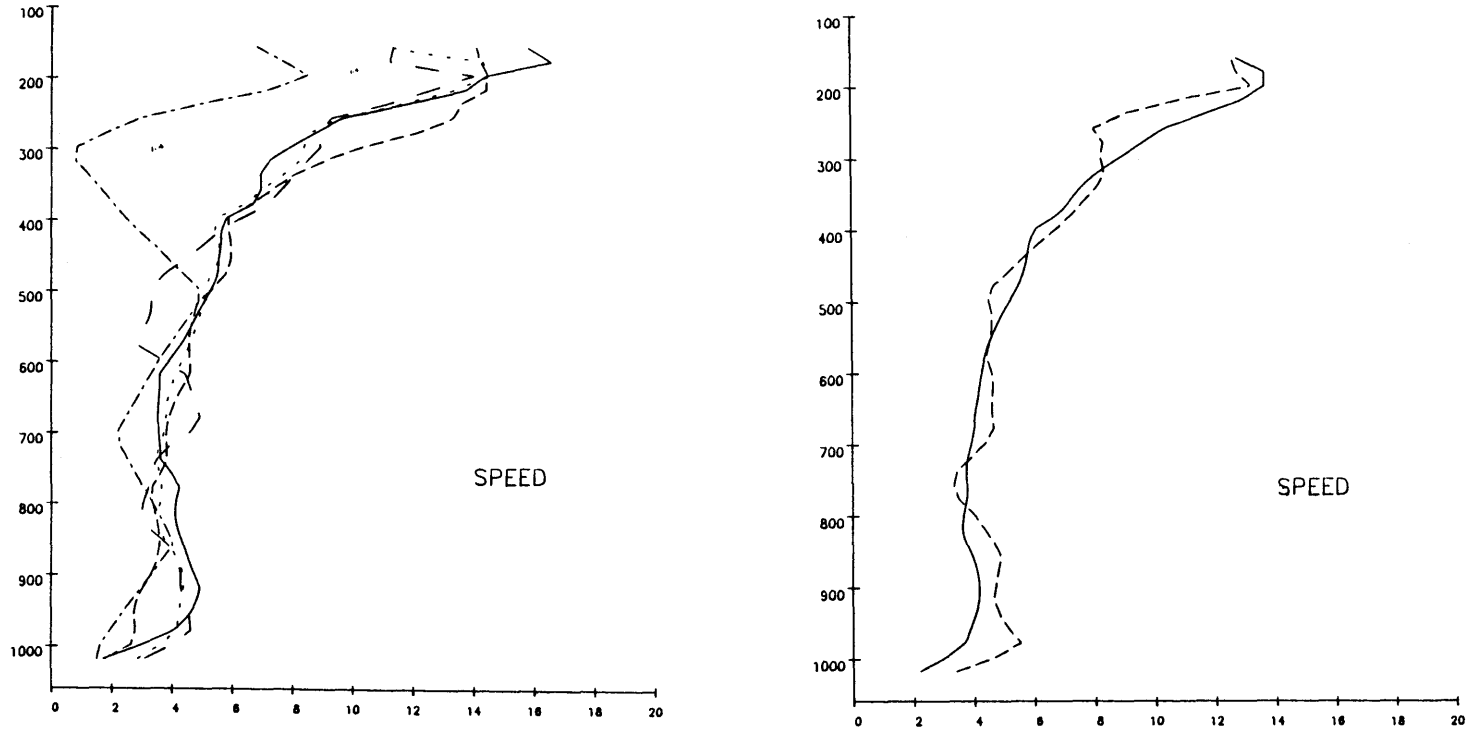


Figure 4.4. Composite vertical profiles of wind speed in m/s for (a) strong southeast (——), light southeast (– – –), strong east (- - - -), very light and variable (— —), and strong southwest (-·-·-). Synoptic wind classes and (b) the averaged profiles for the undisturbed (——) and disturbed (— —) synoptic classes. Vertical ordinate axis is pressure in mb.

Table 4.2. Means, $\bar{x}$, and standard deviations, $\sigma$, for wind speed (m/s), equivalent potential temperature ($\theta_e$ in °K), and saturated equivalent potential temperature ($\theta_{es}$ in °K) at several pressure levels for all synoptic classes for which three or more cases were collected.

| P(mb) | | All Undisturbed | | | Disturbed | | | Light Southeast | | | Strong Southeast | | | Strong East | | | Light and Variable | | |
|---|---|---|---|---|---|---|---|---|---|---|---|---|---|---|---|---|---|---|---|
| | | Speed | $\theta_e$ | $\theta_{es}$ | Speed | $\theta_e$ | $\theta_{es}$ | Speed | $\theta_e$ | $\theta_{es}$ | Speed | $\theta_e$ | $\theta_{es}$ | Speed | $\theta_e$ | $\theta_{es}$ | Speed | $\theta_e$ | $\theta_{es}$ |
| 850 | $\sigma$ | 1.7 | 5.3 | 3.9 | 2.6 | 3.8 | 2.4 | 1.3 | 2.6 | 2.6 | 2.6 | 3.0 | 2.4 | 1.6 | 3.8 | 2.3 | 1.5 | 11.9 | 4.9 |
| | $\bar{x}$ | 4.0 | 334.8 | 347.2 | 4.9 | 335.3 | 343.8 | 3.6 | 336.0 | 345.8 | 4.4 | 334.5 | 346.8 | 3.9 | 335. | 345. | 3.9 | 329.8 | 353.4 |
| 700 | $\sigma$ | 1.8 | 5.2 | 3.9 | 2.2 | 6.9 | 1.5 | 2.3 | 4.6 | 3.2 | 2.0 | 2.4 | 3.4 | 1.6 | 4.8 | 2.5 | 2.2 | 11.3 | 4.0 |
| | $\bar{x}$ | 3.9 | 329.3 | 340.6 | 4.4 | 329.1 | 338.4 | 3.8 | 330.4 | 339.1 | 3.6 | 328.3 | 339.1 | 3.8 | 329.2 | 340.1 | 4.6 | 329. | 345.6 |
| 500 | $\sigma$ | 2.5 | 3.6 | 2.3 | 2.5 | 4.7 | 2.7 | 3.0 | 4.5 | 2.9 | 2.6 | 2.6 | 2.5 | 2.4 | 2.4 | 1.2 | 1.4 | 2.6 | 3.1 |
| | $\bar{x}$ | 5.3 | 330.8 | 337.5 | 4.5 | 331.1 | 337.6 | 5.4 | 330.3 | 337.2 | 5.4 | 329.2 | 336.7 | 5.1 | 330.9 | 337.9 | 3.4 | 330.6 | 336.1 |
| 300 | $\sigma$ | 6.0 | 1.8 | 1.9 | 5.1 | 2.8 | 2.9 | 10.7 | 2.8 | 2.8 | 4.6 | 0.9 | 0.8 | 4.0 | 1.4 | 1.6 | 4.1 | 1.3 | 2.2 |
| | $\bar{x}$ | 8.9 | 339.5 | 341.3 | 8.2 | 339.0 | 340.5 | 10.3 | 338.9 | 340.4 | 7.9 | 340.2 | 342.0 | 8.4 | 338.6 | 340.6 | 8.9 | 340.0 | 341.8 |
| 200 | $\sigma$ | 9.0 | 3.6 | 3.7 | 7.7 | 3.7 | 3.8 | 13.9 | 5.6 | 5.8 | 10.8 | 3.7 | 3.8 | 7.0 | 2.9 | 3.0 | 6.2 | 2.5 | 2.7 |
| | $\bar{x}$ | 13.7 | 346.8 | 347.2 | 13.2 | 345.6 | 346.0 | 14.5 | 347.7 | 348.2 | 94.4 | 347.8 | 348.2 | 14.5 | 345.3 | 345.6 | 14.0 | 346.2 | 346.6 |

for strong southwesterly which reaches a minimum speed at 300 mb. The disturbed and undisturbed class winds are similar; the major difference is found below 800 mb where the disturbed winds are stronger. Standard deviations for each class given in Table 4.2 are, in general, less than the values for the undisturbed class indicating that the synoptic flow classes show less variance and the means for wind speed are more significant than for the average of the undisturbed class. In summary, wind directions are more representative of the synoptic flow class than was wind speed which shows less statistically significant differences between classes.

To discuss the temperature and moisture profiles, $\theta_e$, $\theta_{es}$ and $\theta_{es}-\theta_e$ were plotted. As implied from the definitions for these variables in Section 2.2, $\theta_e$ is a measure of both temperature and humidity, while $\theta_{es}$ is a function of temperature. $\theta_{es}-\theta_e$ represents how unsaturated the atmosphere is.

The $\theta_e$ profiles depicted in Figure 4.5 show the light and variable and strong southeast classes to have the smallest values in the lowest 400 mb. Standard deviations through this layer, however, presented in Table 4.2, are high for the light and variable class as compared with the values for the other classes. Therefore, this difference is apparently not significant. $\theta_e$ is greatest through most of the atmosphere for strong southwesterly synoptic flow. When $\partial\theta_e/\partial z$ becomes positive at mid and upper levels, the profiles for all the categories begin to converge toward each other.

$\theta_e$ is lower for the disturbed case as compared to the undisturbed class from the surface to 920 mb and slightly larger in the mid troposphere (Figure 4.5b). However, due to the relatively

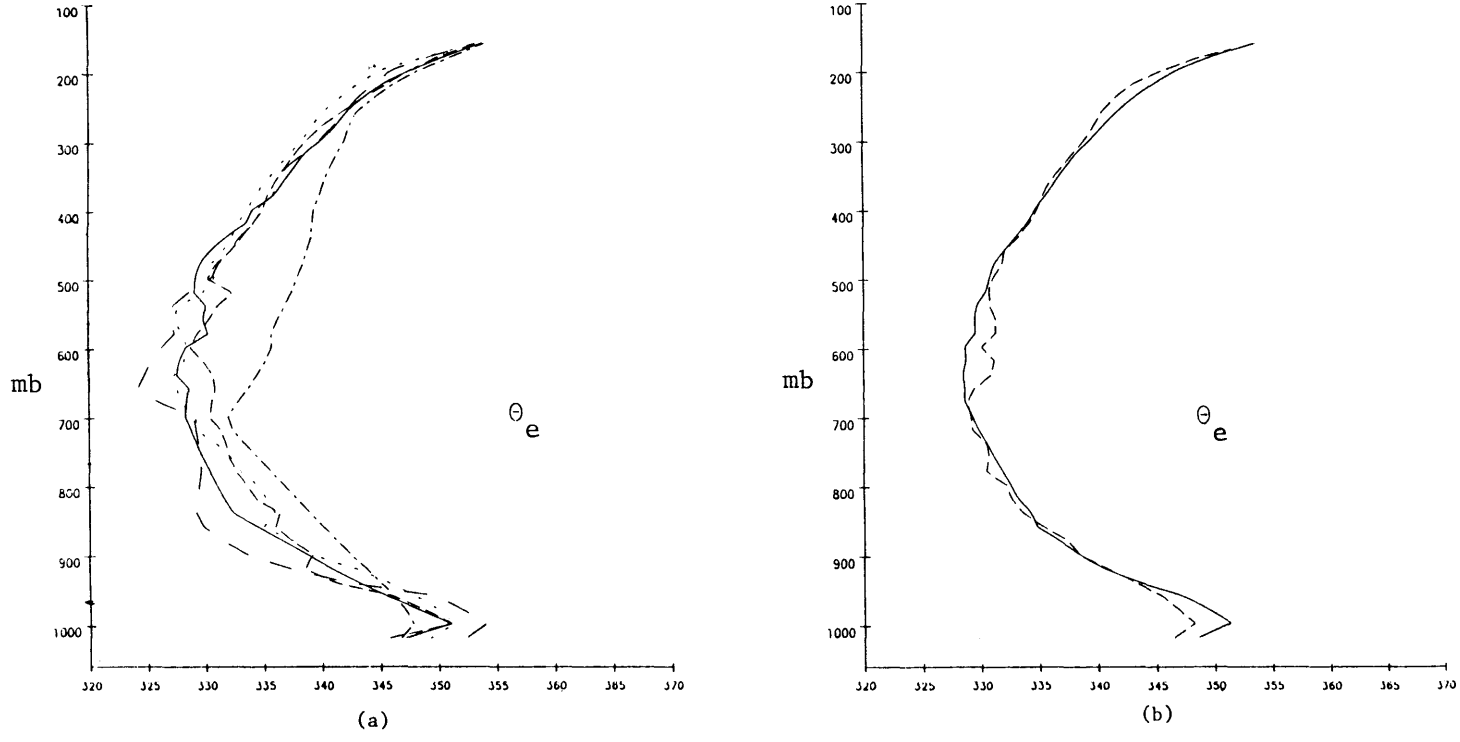


Figure 4.5. Composite vertical profiles of equivalent potential temperature ($\theta_e$) in °K for (a) strong southest (———), light southeast (– – –), strong east (- - - -) very light and variable (— —), and strong southwest (– · – ·) synoptic wind classes and (b) the averaged profiles for the undisturbed (———) and disturbed (— —) synoptic classes. Vertical ordinate axis is pressure in mb.

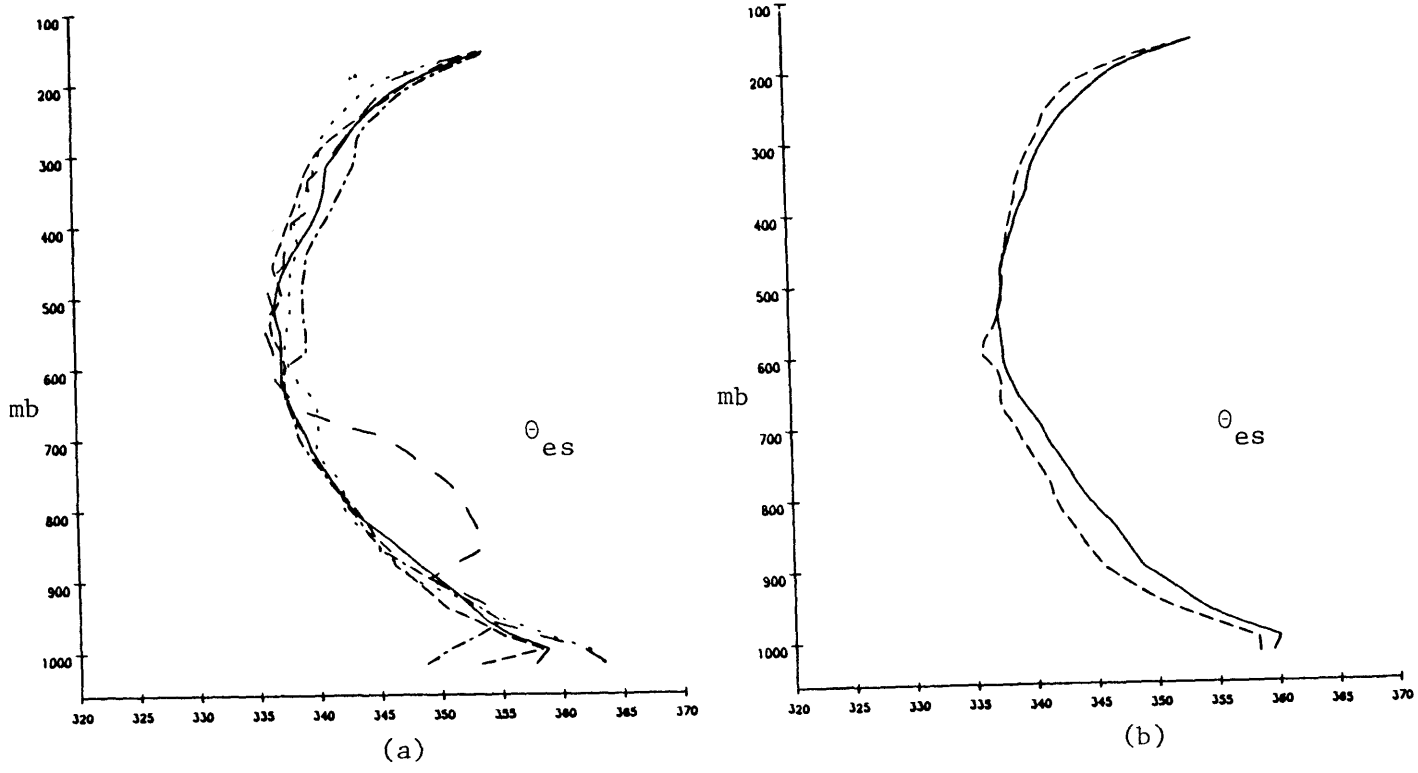


Figure 4.6. Composite vertical profiles of saturated equivalent potential temperature ($\Theta_{es}$) in °K for (a) strong southeast (——), light southeast (– – –), strong east (- - - -), very light and variable (— —), and strong southwest (-·-·) synoptic wind classes and (b) the averaged profiles for the undisturbed (——) and disturbed (— —) synoptic classes. Vertical ordinate axis is pressure in mb.

large standard deviations for $\theta_e$ in the lower levels, the differences through these layers are statistically insignificant.

For $\theta_{es}$ (Fig. 4.6), there are not many distinctions between each class above the lowest 50 mb. One exception is for light and variable flow which shows a warmer atmosphere from 920 to 700 mb. This is possibly associated with the warm advection through this layer which was noted earlier for this class. Using the definition for statistical significance provided earlier and the standard deviations shown in Table 4.2, at 850 mb, it is concluded that the warming indicated is statistically significant. $\theta_{es}$ for the undisturbed class is somewhat greater through the lowest 400 mb when compared to the disturbed class.

For the $\theta_{es}$-$\theta_e$ profiles (Fig. 4.7), the light and variable category exhibits a very dry layer from 950 to 600 mb. However, as indicated from Table 4.2, the standard deviations for $\theta_e$ at 850 and 700 mb for this case are 11.7°C and 11.3°C, respectively, which is twice as large as that for the undisturbed class for the same levels. This may imply that the dry layer for light and variable flow is not as significant as implied by Fig. 4.7. Strong southwesterly and light southeasterly classes have relatively moist atmospheres. Some drying is present in the lower troposphere for strong southeasterly flow and in the mid troposphere for strong easterly flow. The undisturbed class reveals a drier lower and mid troposphere compared to the disturbed class. The difference is statistically significant at 850 mb but not at 700 mb.

The above discussion helps give a qualitative description of the synoptic environment for each synoptic flow regime. These results can

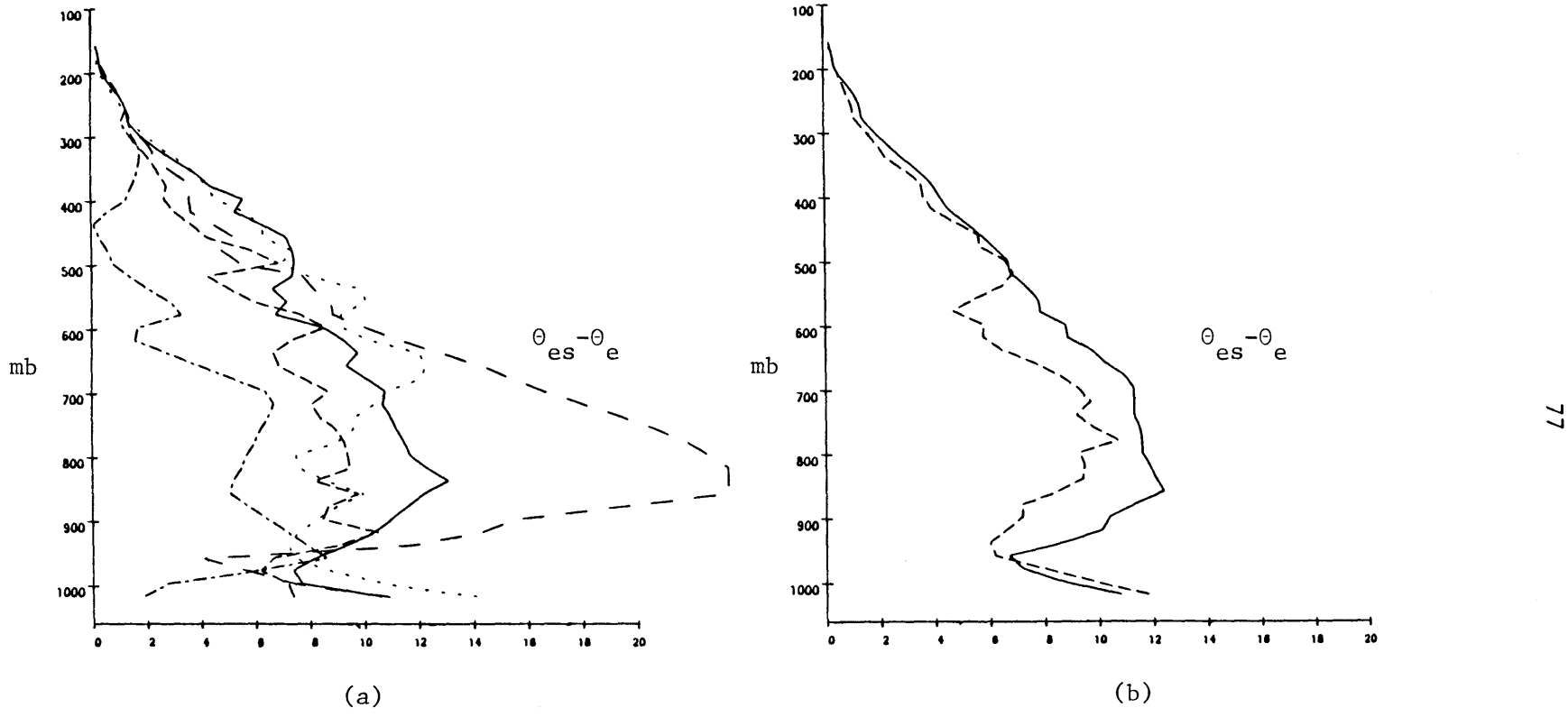


Figure 4.7. Composite vertical profiles of the difference between saturated equivalent and equivalent potential temperature ($\Theta_{es}-\Theta_e$) in °K for (a) strong southeast (——), light southeast (– – –), strong east (- - - -), very light and variable (— —), and strong southwest (– · – ·) synoptic wind classes and (b) the averaged profiles for the undisturbed (——) and disturbed (— —) synoptic classes. Vertical ordinate axis is pressure in mb.

be helpful while examining the causes for differences in the results between the cloud composites for each category.

With the above results, the large scale environment for each class can be summarized. The disturbed class revealed considerably more wind shear through the troposphere and therefore more baroclinicity, with stronger low-level winds than for the undisturbed class. Cold air advection aloft as inferred from the wind hodographs extended through a deep layer. Also, while it was found that the differences in convective stabilities were insignificant based on the values of $\overline{\Delta\theta_e}$, the $\theta_{es}$ and $\theta_{es}-\theta_e$ vertical profiles exhibited a somewhat cooler and moister lower troposphere for the disturbed category although the differences were statistically marginal. The disturbed regime had a higher daily average of deep convective clouds than for the undisturbed class (as was shown in Table 4.1).

When comparing the variables between each synoptic flow category, the light and variable environment was found to be the most unique. This category was shown to have much drier and warmer conditions between 950 and 600 mb than for any of the other categories. Also the value for $\overline{\Delta\theta_e}$ indicated that the light and variable environment was the most stable of all the classes presented although this result was not very significant as indicated from the value of its standard deviation. Winds remained out of the southeast through 500 mb and then backed toward the east-northeast suggesting cold advection aloft for this case. The percent of deep convection was very small for the light and variable class and its magnitude was well below the value obtained for the other classes. Although the light and variable environment was most different from the environments of any other

class, the variances in most of its mean variables were greater than any other undisturbed flow category, therefore reducing the significance of some of the differences.

For light southeast synoptic flow, the wind direction remained fairly constant from the southeast through the lowest 300 mb. The winds shifted toward the northwest and increased in speed with height above 700 mb. The veering of the winds above 700 mb through 200 mb implied warm advection aloft through a depth greater than any of the other categories. This category proved to have the same value of $\overline{\Delta\theta_e}$ as light and variable but the variance was much less. Light southeasterly synoptic flow was relatively moist through most of the troposphere. The amount of convection present (5.4 percent daily average) was just below the average for all the undisturbed days combined. Having a near average amount of deep convection under a relatively stable (but moist) atmosphere for light southeasterly flow may imply that if this category persisted for several days, a significant amount of moisture may accumulate aloft due to the diurnal cycle of convection.

Some of the more statistically meaningful environmental characteristics for the strong southeast class were that low-level winds resembled the light southeast winds in direction but had stronger speeds. Also, from 950 to 650 mb, the moisture deficit was relatively large. It was the most convectively unstable class with $\overline{\Delta\theta_e}$ equal to 5.0°C. Strong southeasterly flow had the most deep convective clouds of any undisturbed class although the difference in the daily average between it and the undisturbed days average was only 2.1 percent.

The easterly environment winds were strong and easterly through the lowest half of the atmosphere. A deep layer of cold advection was noted from 900 to 200 mb. Just above the surface, the moisture for this class was relatively high to around 800 mb. Above this, considerable drying was noted. Convective instability was high for this class with a value of $\overline{\Delta\Theta_e}$ equal to 4.9°C. The daily averaged percent deep convection was 5.4 percent, the same as the value for light southeasterly flow.

The strong southwest winds were out of the southwest from the surface to 300 mb. Above this level, winds backed to light northeasterly. This environment is the moistest through the entire troposphere. It had a warmer upper atmosphere and was fairly unstable through the depth of convective instability. During the afternoon, the percent coverage of deep convective clouds was similar to all the undisturbed classes except the light and variable class.

There is a suggestion from the above that a certain threshold of available moisture in the lower troposphere is a necessary condition for significant amounts of well-developed cumulus clouds to occur. This is indicated from the relationship between the very low amount of moisture available and low percent of afternoon deep convection for light and variable flow. Another large-scale characteristic for the light and variable class was its very warm lower troposphere.

Betts (1974) composited tropical soundings according to the degree of convective activity. His results showed $\Theta_e$ to increase and $\Theta_{es}$ and $\Theta_{es}-\Theta_e$ to decrease in the lower and middle troposphere with increasing convective activity. This suggested that a cool and moist low and middle troposphere is favorable for convection to

develop in the tropics. Burpee (1979) also found this result to be true for South Florida. The results from the light and variable sounding composite revealing a warm and dry low and mid troposphere with little convective activity are in agreement with the above authors' findings. Another anomaly present in the light and variable environment which may inhibit convection was the strong thermal stability present as seen in the low values of $\overline{\Delta\theta_e}$ and $\Delta P$. However, the differences when comparing these variables with those calculated for the other categories were relatively small.

Except for the light and variable flow environment, differences in convective activity and thermodynamic characteristics were only slightly significant for the various synoptic flow categories. This may suggest that the low level synoptic flow and therefore the sea breeze forcing only weakly controls the amount of convective cloud coverage, although as discussed in Chapter 5, the patterning of the cumulus convection over the area critically depends on the location of the sea breeze convergence zones and sea breeze induced spatial variations in thermodynamic structure over the area. The low level wind, especially the low level wind direction, did show significant variations from class to class, as expected because of the synoptic classification scheme. Therefore, the subjective categorization based on surface geostrophic wind used to classify the synoptic flow, did agree well with the single station wind profiles. Some differences between the single station winds and the subjectively categorized winds can be due to local effects particular to the station.

Before discussing further the importance of these large-scale forcings and the low-level winds on controlling the amount of deep

convective clouds over South Florida, correlations will be found between these forcings and the percent of deep convection in the afternoon. The results of the regressional analysis should help interpret what has been implied from the data so far.

## 4.2. Quantitative Results

Results of a bivariate regression correlating the percent of deep convective clouds covering the South Florida peninsula at 1400 EST with some of the large-scale environmental variables are presented in this section. Correlation coefficients and their significance are shown in Table 4.3 for populations with (1) only undisturbed days, (2) all days including disturbed, (3) undisturbed light low-level wind days ($V_g \leq 3.5$ m/s at the surface at 7 EST) as estimated from surface pressure analysis, and (4) undisturbed strong low-level wind days ($V_g > 3.5$ m/s at the surface at 7 EST). $SPd_{200}$, $U_{200}$, and $V_{200}$ are the wind speed, and U and V component of the wind at 200 mb, respectively. $SPd_{Vg}$, $U_g$ and $V_g$ are the geostrophic wind speed, and U and V components of the geostrophic wind at the surface.

Conclusions made from these results alone can only be considered preliminary since the sample size for undisturbed days was small with only 28 soundings available. Comparisons with other works which used different data sets for South Florida will be made whenever possible to help substantiate the results presented here.

Some of the major indications implied from Table 4.3 are:

(1) For only undisturbed days, the moisture deficit through the depth of convective instability, $\overline{\theta_{es}-\theta_e}$, is the only variable indicating appreciable significance. Since it is negatively correlated,

Table 4.3. Correlation coefficients (R) and significance (Sig) from a bivariate regression analysis correlating the percent of deep convection over the South Florida peninsula at 1400 EST with several large-scale variances. Populations used for the regressions were subdivided into four categories: (1) only undisturbed days, (2) all days including disturbed days, (3) light wind undisturbed days ($V_g \leq 3.5$ m/s), and (4) strong wind undisturbed days ($V_g > 3.5$ m/s). Asterisks indicate significance at the .05 level or less.

| | Undisturbed | | All Days | | Undisturbed | | | |
|---|---|---|---|---|---|---|---|---|
| | | | | | Light Wind | | Strong Wind | |
| | R | Sig | R | Sig | R | Sig | R | Sig |
| $\Delta P$ | .05 | .82 | .24 | .20 | -.26 | .40 | .40 | .22 |
| $\Delta\overline{\theta_e}$ | .007 | .97 | -.24 | .22 | .04 | .91 | -.26 | .43 |
| $\overline{\theta_{es}-\theta_e}$ | -.38 | .07 | -.26 | .18 | -.42 | .18 | -.36 | .27 |
| $SPd_{200}$ | -.16 | .43 | -.18 | .32 | -.32 | .26 | -.06 | .85 |
| $U_{200}$ | -.15 | .47 | -.17 | .35 | -.04 | .89 | -.34 | .30 |
| $V_{200}$ | -.10 | .62 | -.24 | .20 | -.03 | .93 | -.16 | .64 |
| $SPd_{vG}$ | .18 | .37 | .39 | *.03 | .44 | .10 | -.50 | .12 |
| $U_g$ | .03 | .89 | .13 | .46 | .06 | .82 | .42 | .19 |
| $V_g$ | .11 | .60 | -.09 | .60 | -.28 | .32 | .15 | .66 |

the amount of moisture available in the lower and middle troposphere will be positively correlated with the amount of deep convective clouds in the afternoon. The results of Frank and Smith (1968), Pielke et al. (1977), and Burpee and Lahiff (1984) agree with this finding that the availability of moisture is the best correlated variable with the daily rainfall amount over South Florida. For all days combined the availability[4] of moisture is not as significant as for the undisturbed days alone.

(2) While the other variables are not correlated at the significant level with afternoon convective cloud activity for undisturbed days, some general conclusions can be drawn.

   (a) The variables describing the thermal stability, $\overline{\Delta\theta_e}$ and $\Delta P$, are both unimportant for sea breeze days but are better correlated with convective activity when all days are considered. The results imply that the percent of coverage by convective clouds increases as the depth of convective instability increases but with the magnitude of convective instability decreasing. This possibly suggests that weaker convective instability is associated with more, but less intense deep cumulus.

   (b) Wind speeds at 200 mb are negatively correlated with convective activity for synoptically undisturbed days and when all days are considered. Therefore, the weaker the winds aloft, then the more deep convective clouds will be present at 1400 EST.

   (c) For low-level winds, when all days are considered, the geostrophic wind speed is positively and significantly

correlated at the .05 level but is positively but not significantly correlated for undisturbed days. The positive correlation for undisturbed days partly reflects cloud behavior for the very light and variable wind class, which as described in the last section, was strongly suppressed compared to the other synoptic classes.

For undisturbed days, a more southerly wind component in the low level flow was favorable for enhancing convective activity while the east-west wind component showed near zero correlation. These tendencies were also revealed in the data sets of Burpee and Lahiff (1984) and Lopez et al. (1984), only their results suggested an even stronger correlation for southerly winds with the daily rainfall over South Florida.

Remembering that the number of cases available was only 13 for light wind days and 15 for strong wind days, the following points are suggested from the results shown in Table 4.3.

(1) The most correlated variable for both wind days is the low-level geostrophic wind speed which is significant in both cases to the 0.10 level. Results confirm the conclusion that the positive correlation on the light wind days is partly due to the suppressed convective activity of the very light and variable wind days, which are included in the light wind class. For strong wind days the correlation is negative. These results indicate that medium wind speeds are favorable for convection. A possible explanation for this is that if the winds are very light, then it is likely that high pressure could be centered

over the peninsula and convection would be suppressed by synoptic scale subsidence and less advection of moister air from the ocean. If the winds are too strong, then convection along the upwind coast is not allowed to develop while convection along the downwind coast is advected offshore. Blanchard and Lopez (1984) noted a reduced amount of convective activity on days which had strong easterly winds.

(2) $\overline{\theta_{es}-\theta_e}$ is more significantly correlated for light wind days ($r = -.42$) than for strong wind days ($r = -.36$). Pielke et al. (1977) similarly stratified synoptically undisturbed days into light and strong wind days. The results of that regression calculation showed $\overline{\theta_{es}-\theta_e}$ to be negatively correlated with daily averaged rainfall over South Florida for light wind days but positively correlated for strong wind days. The correlations between the two wind populations only weakly exhibit Pielke et al.'s findings. A larger population would be needed to substantially verify or refute their results.

Table 4.4 gives the results for the bivariate regressions between the percent of deep convective clouds covering the land at 1400 EST with other percent cloudiness variables. Methods to calculate these variables were described in Section 2.2 . Some of the major points from the table are:

(1) For synoptically undisturbed days, the percent of afternoon deep convective clouds is not well correlated with the 0800 EST deep convective cloudiness activity covering the peninsula. It is correlated positively, however, at the .01 level with the percent

Table 4.4. Correlation coefficients (R) and significance (Sig) from a bivariate regression analysis correlating the percent of deep convection over the South Florida peninsula at 1400 EST with several percent cloudiness variables. Populations used for the regressions were subdivided into four categories: (1) only undisturbed days, (2) all days including disturbed days, (3) light wind undisturbed days ($V_g \leq 3.5$ m/s), and (4) strong wind undisturbed days ($V_g > 3.5$ m/s). Asterisks indicate significance at the .05 level or less.

| | Undisturbed | | All Days | | Undisturbed | | | |
|---|---|---|---|---|---|---|---|---|
| | | | | | Lt. Wind | | Str. Wind | |
| | R | Sig | R | Sig | R | Sig | R | Sig |
| % All Clouds over Land at 0800 EST | .10 | .68 | .29 | .16 | .34 | .28 | .20 | .61 |
| % Deep Convection over Land at 0800 EST | .26 | .25 | .40* | .05 | .61* | .04 | .11 | .78 |
| % Deep Convection over Land at 1000 EST | .59* | .01 | .46* | .03 | .81* | .01 | .55 | .16 |
| % Deep Convection over Water at 0800 EST | .44* | .05 | .43* | .03 | .74* | .01 | .30 | .43 |

of convective cloudiness over the peninsula at 1000 EST. The correlation coefficient is .59.

(2) Unlike the behavior on undisturbed days, the all-day population illustrated that the percent of deep convective clouds over land at 0800 EST exhibits a significant correlation with deep convective cloudiness activity over land in the afternoon. This suggests that disturbed days depend less on the onset of solar heating than the undisturbed days.

(3) The 1400 EST percent of deep convection on light wind, undisturbed days indicates significant positive correlations between the percent of deep convective cloudiness over land at 0800 and 1000 EST and that found over water at 0800 EST. For strong wind days the correlations between these variables are not significant. Due to the lack of data for each of the wind regimes, these results can only be considered preliminary.

(4) For undisturbed days and for all days, the percent of deep convective activity over water at 0800 EST is correlated with the percent convection at 1400 EST over land to within the .05 significance level.

From the last point it is suggested that the amount of convective cloudiness at 0800 EST over water may be an indicator of how favorable the synoptic environment will be for the development of deep convective cloud activity over land in the afternoon. The percent of deep convective cloudiness over land at 0800 EST does not correlate well with the afternoon convective cloud activity. Over the offshore water the nocturnal land breeze provides the forcing for convective cloudiness over the oceans when the atmosphere is synoptically undisturbed.

Since the synoptic thermodynamic atmosphere over the land will generally be the same as over the offshore waters, the amount of convection off the coast which is generated by the land breeze would be expected to be well correlated with afternoon convection over land as the triggering mechanism of the sea breeze develops.

The results of the regressions verify the inference made qualitatively in the last section that the available moisture in the lower troposphere is an important ingredient determining the percent of coverage of deep convective clouds over South Florida. The thermal stability has less of a control on the percent of afternoon deep convective cloudiness than did the moisture availability. The regression analysis also supports the conclusion made in Section 4.1 that the low-level winds only weakly control the amount of convective cloudiness (although the positioning of the clouds will be affected as discussed in the next section). Blanchard and Lopez (1984) also found this to be the case from the results of a radar climatology of the South Florida peninsula. However, the subjective synoptic classification based on the surface geostrophic winds did agree well with the averaged low-level winds calculated from single station data. Finally, another useful predictor for the amounts of deep convective cloudiness in the afternoon for synoptically undisturbed days over the peninsula was the 1000 EST percent of deep convective cloudiness over land and the 0800 EST percent of deep convective cloudiness over the waters surrounding the South Florida peninsula.

# CHAPTER 5

# THE SPATIAL VARIATIONS OF CONVECTIVE CLOUDINESS OVER SOUTH FLORIDA

## 5.1 Results from the Satellite Image Composites

Previous studies have compiled radar-derived climatologies stratified by synoptic flow (Frank et al., 1967; Smith, 1970) and by similarities in radar patterns (Blanchard and Lopez, 1984) to determine the spatial variations of rainfall over Florida. For the current study, satellite image composites will be presented to describe the spatial variations in the cloudiness patterns over South Florida and the surrounding waters for the various synoptic classes described in Chapter 4. The results of the composites will indicate preferred areas of the peninsula for cloud activity. The differences in the spatial patterns of the cloud activity from one synoptic flow to another will also be outlined. Section 5.2 will attempt to explain some of the observed patterns found in the satellite image composites using the results of a numerical model which encompasses the surface peninsula scale forcings and its interaction with the synoptic flow, as well as incorporates the effects of the sub-peninsula variations in the ground surface. The details of the model were reported in Chapter 3.

Figures 5.1 and 5.2 show the evolution of deep convective cloudiness for all undisturbed days at 1200, 1400, 1600, and 1800 EST. On the bottom of each image is a bar[1] relating shading to cloud frequency.

[1]Originals of these Figures are in color. Costs prevented color reproductions in this report.

These composites are useful to locate the preferred areas of deep convective clouds throughout the afternoon. However, they include all synoptic flows so that the convective patterns will not be representative of any particular flow condition although a majority of satellite days collected during the summer of 1983 were categorized as southeasterly or easterly over South Florida.

At 1200 EST, two deep convective cloud maxima are found; one along the eastern shore of Lake Okeechobee, the other at the southern edge of the west coast. In both cases, the maximum cloud frequencies are around 25 percent. There is also a region of 10 percent cloud frequencies paralleling the southeast coast. This region is found inland, south of Lake Okeechobee leaving no deep convective cloud activity along the immediate southeast coastline.

By 1400 EST, the deep convective cloud activity has dramatically increased as compared to 1200 EST. The preferred areas of deep convective clouds lie mainly in an elongated region along the southwest coast. In this area, two wide zones of high cloud frequencies are separated by a local minima. The southern maxima extends eastward to the center of the peninsula. The northern maxima of high cloud frequencies appears near a region of preferred convective clouds extending from the maxima to just west of Lake Okeechobee. From the lake, the line turns toward the northwest paralleling the coast. An area of low convective activity lies along the northwest coast.

By 1600 EST, the zone of high convective cloud frequency grows larger in size along the west coast. It also follows the geometry of the coast quite well. Maximum deep convective cloud frequencies have reached 50 percent. To the north there is a lack of deep convective

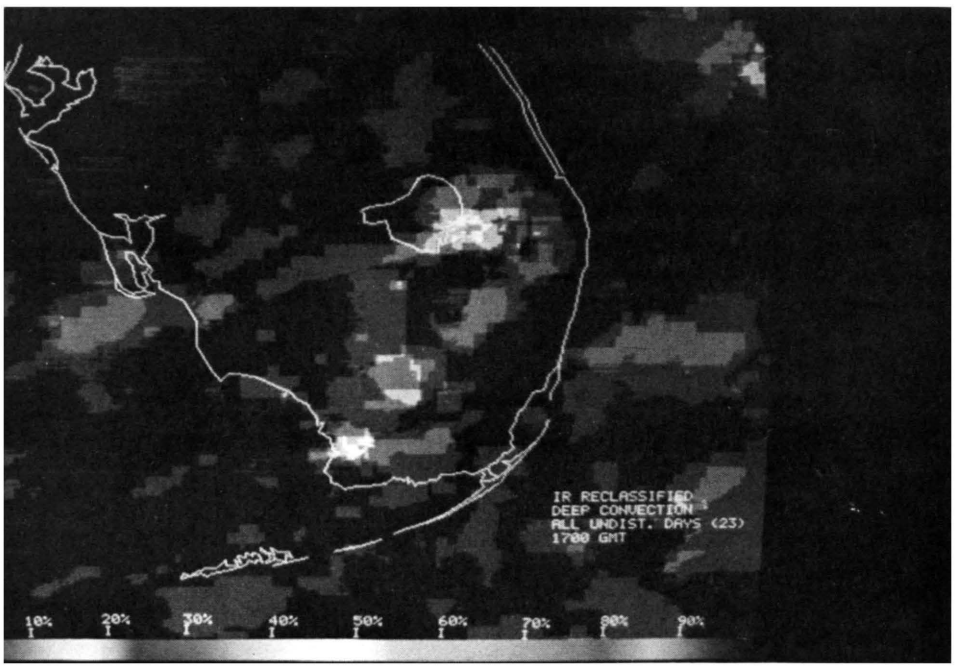


(a)

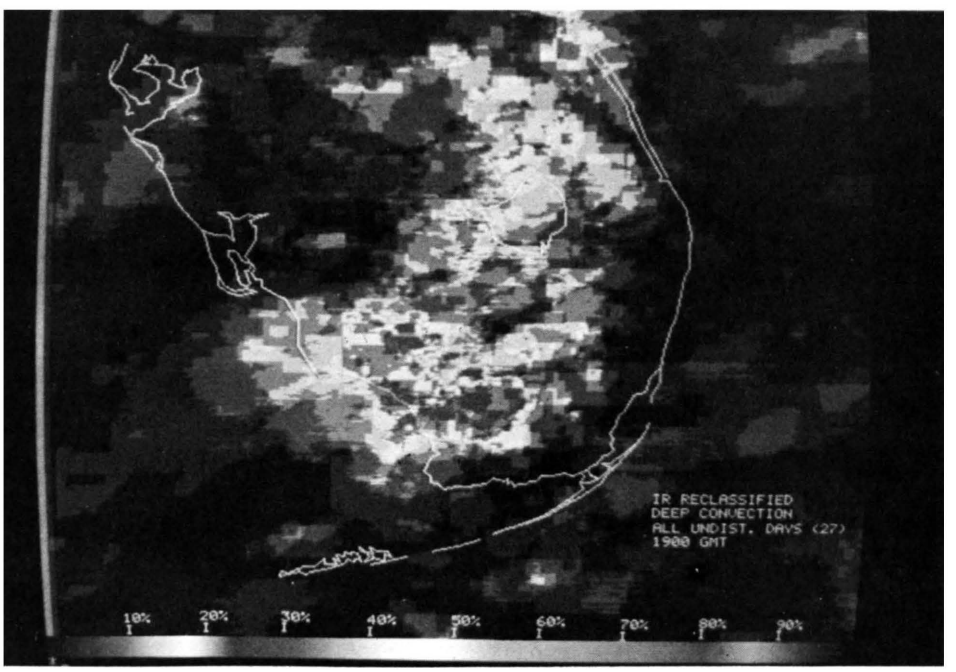


(b)

Figure 5.1. All undisturbed days composite for deep convective clouds for (a) 1200 EST and (b) 1400 EST. Bar on the bottom of image relates shading to cloud frequency (on originals, a color bar is used). The number in parentheses on each image label indicates the number of images which went into creating the composite. (Color slides of all the composites are available, which more clearly illustrate the cloud composite frequencies; costs prevented reproducing these Figures in color for this report).

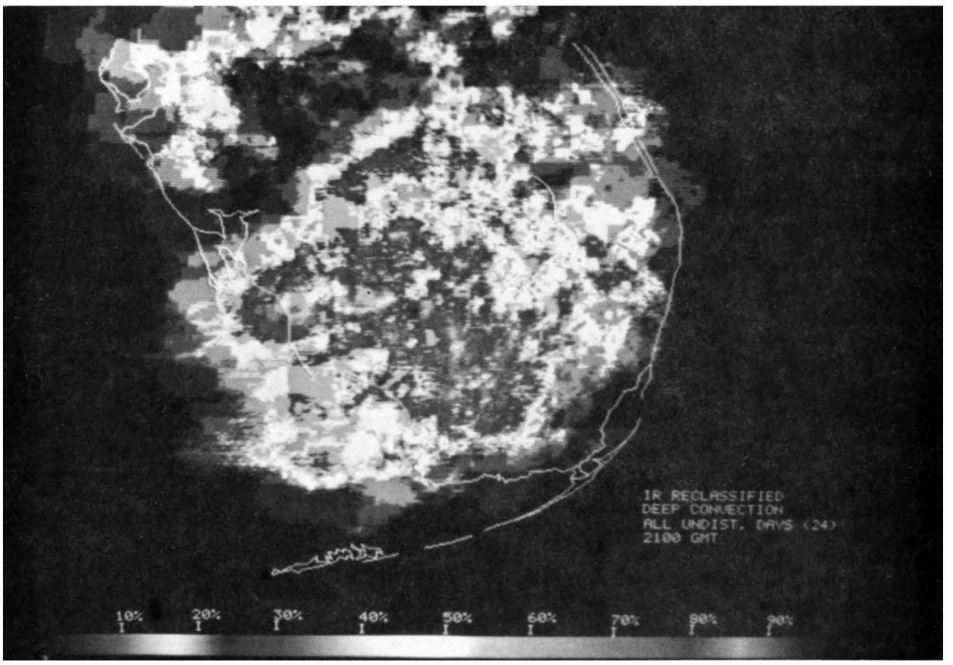


(a)

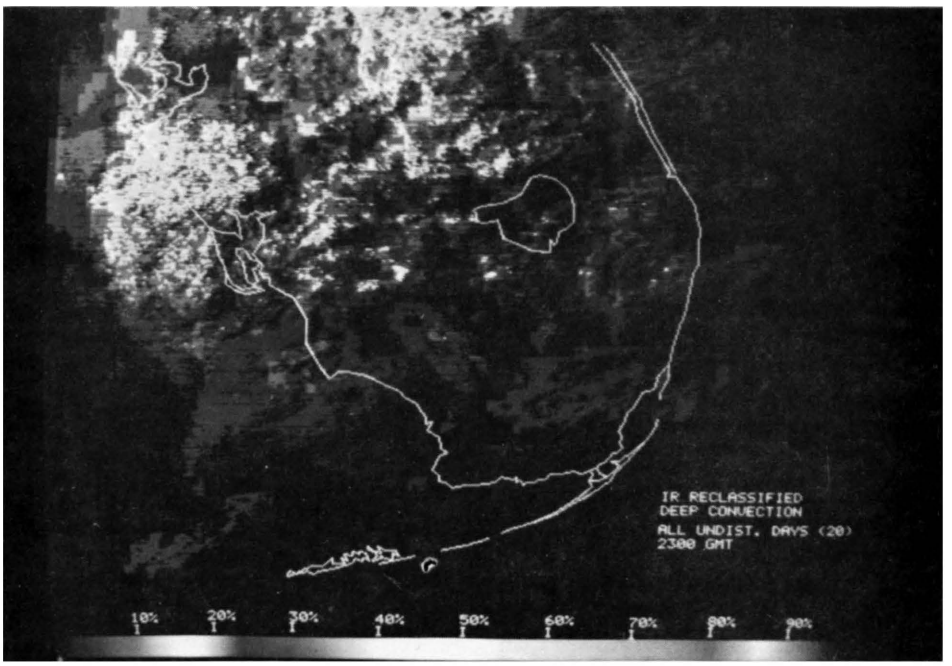


(b)

Figure 5.2. All undisturbed days composite for deep convective clouds for (a) 1600 EST and (b) 1800 EST. Bar on the bottom of image relates shading to cloud frequency (on originals, a color bar is used). The number in parentheses on each image label indicates the number of images which went into creating the composite. (Color slides of all the composites are available, which more clearly illustrate the cloud composite frequencies; costs prevented reproducing these Figures in color for this report).

cloudiness as compared with the south, as was found, also, from the 1400 EST composite. A minimum region in convection stretches along from the west coast to the northeastern interior. Some deep convective cloudiness had developed just north and south of this region.

By 1800 EST, a dramatic decrease in the convective cloud activity has taken place over the southern peninsula. A possible explanation for this was described by Gannon (1978) who found cloud shielding effects to decrease convective cloud activity in the late afternoon over South Florida. Cirrus from the convection may have decreased the thermal contrasts between land and sea by shielding the land from solar radiation. This would serve to decrease the convergence and cool the peninsula. Cooper et al. (1982) also emphasized the importance of convective cloud downdrafts to reduce the convective activity by cooling and drying the planetary boundary layer. To the north, however, deep convective cloud frequencies reach a maximum of 25 percent along the west coast and the center of the peninsula.

Figures 5.3 through 5.10 show the deep convective cloud composite images for light southeast, strong southeast, strong east, and light and variable wind classes for all the afternoon hours. The strong southwesterly case images of August 30, 1983, for 1000, 1200, 1600, and 1800 EST are presented in Figures 5.11 and 5.12. All other images for this day were unavailable. The strong southwest images are examples of the three-shaded reprocessed images which include both deep convective clouds which appear white and all other clouds, which appear grey. The method to create a three-shaded image was described in Section 2.1.

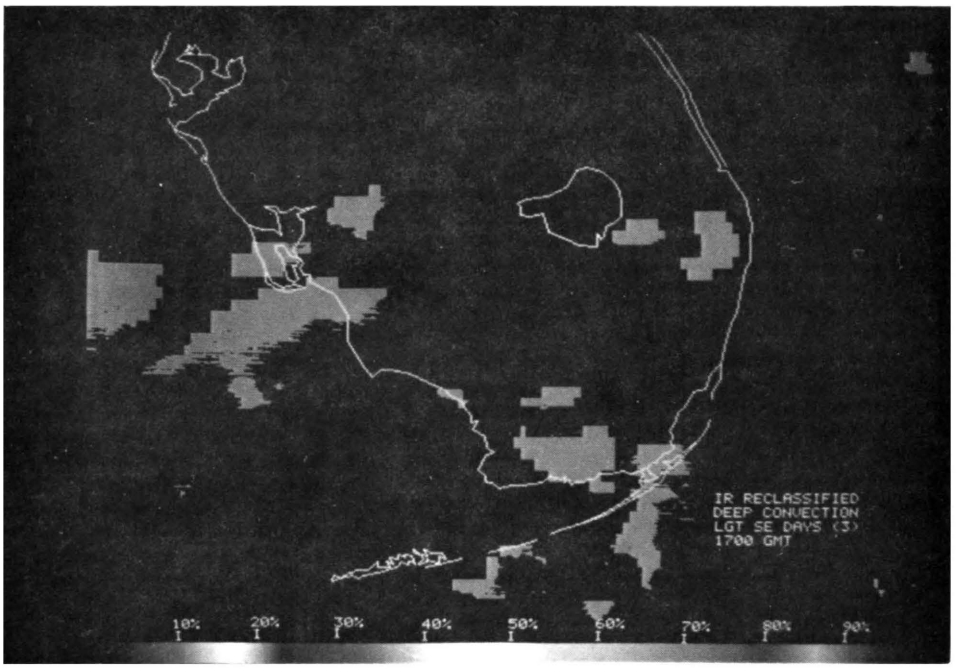


(a)

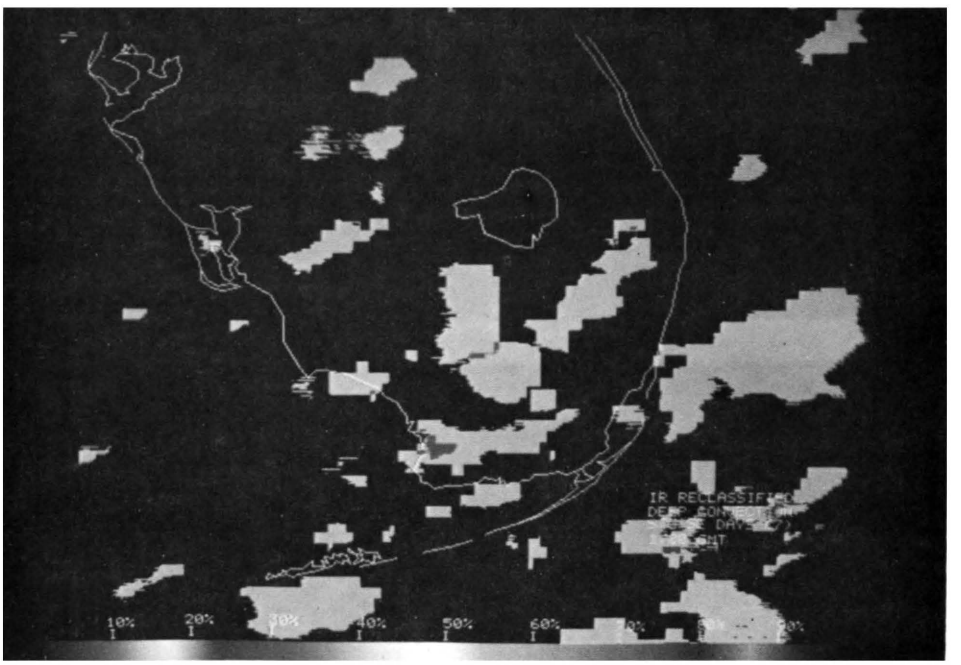


(b)

Figure 5.3. Satellite image composites by synoptic flow for (a) light southeast and (b) strong southeast classes at 1200 EST. Bar on the bottom of image relates shading to cloud frequency (on originals, a color bar is used). The number in parentheses on each image label indicates the number of images which went into creating the composite. (Color slides of all the composites are available, which more clearly illustrate the cloud composite frequencies; costs prevented reproducing these Figures in color in this report).

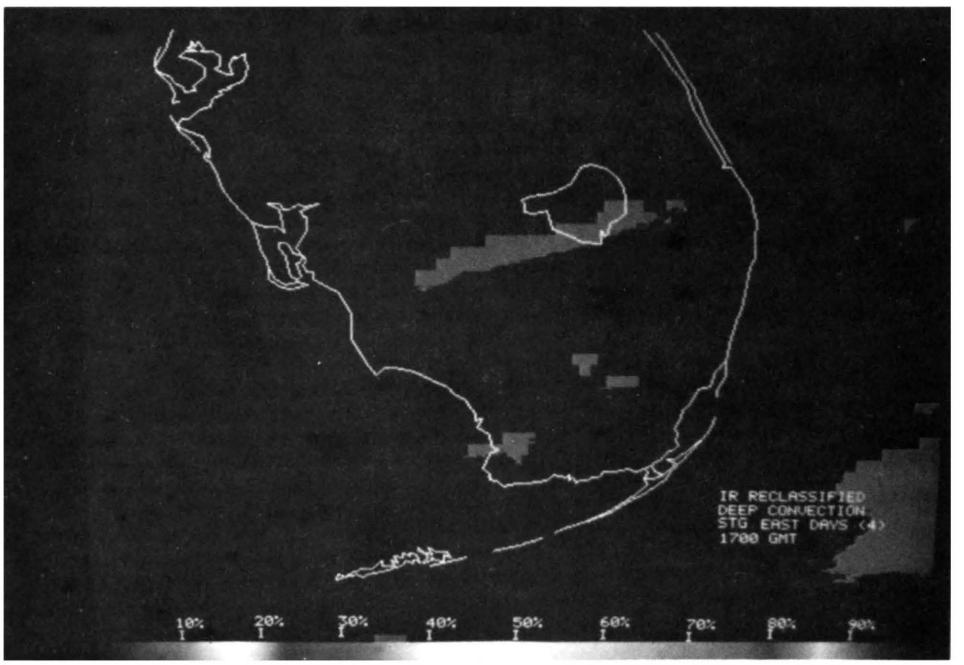


(a)

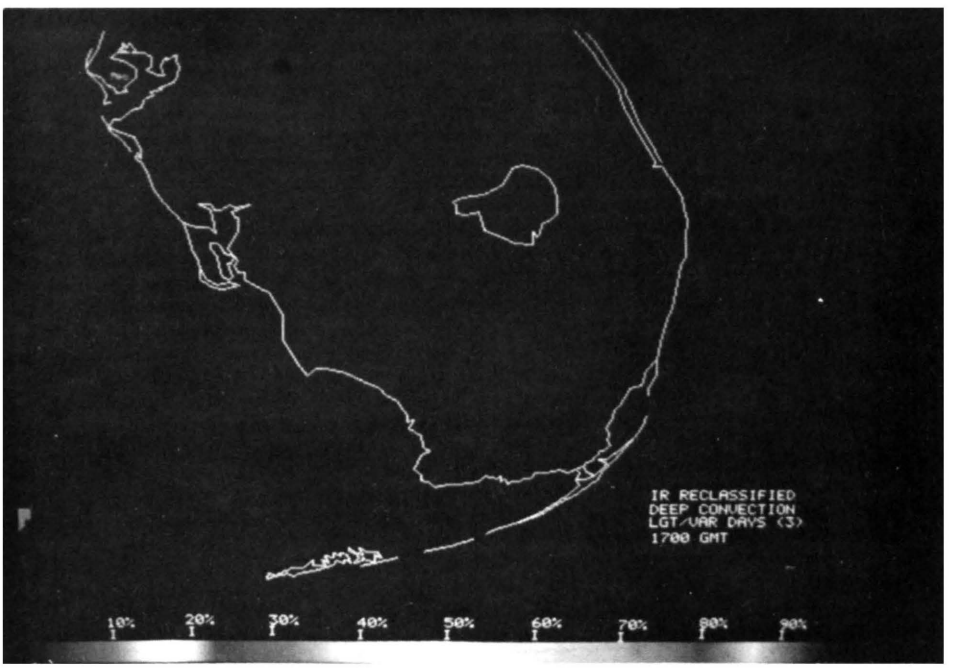


(b)

Figure 5.4. Satellite image composites by synoptic flow for (a) strong east and (b) light and variable synoptic classes at 1200 EST. Bar on the bottom of image relates shading to cloud frequency (on originals, a color bar is used). The number in parentheses on each image label indicates the number of images which went into creating the composite. (Color slides of all the composites are available, which more clearly illustrate the cloud composite frequencies; costs prevented reproducing these Figures in color in this report).

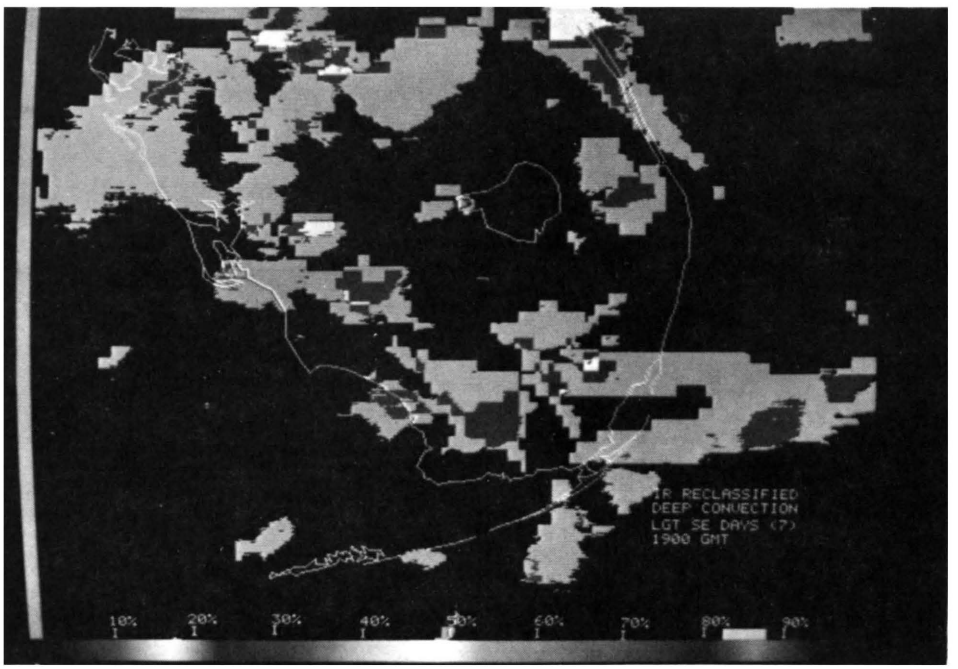


(a)

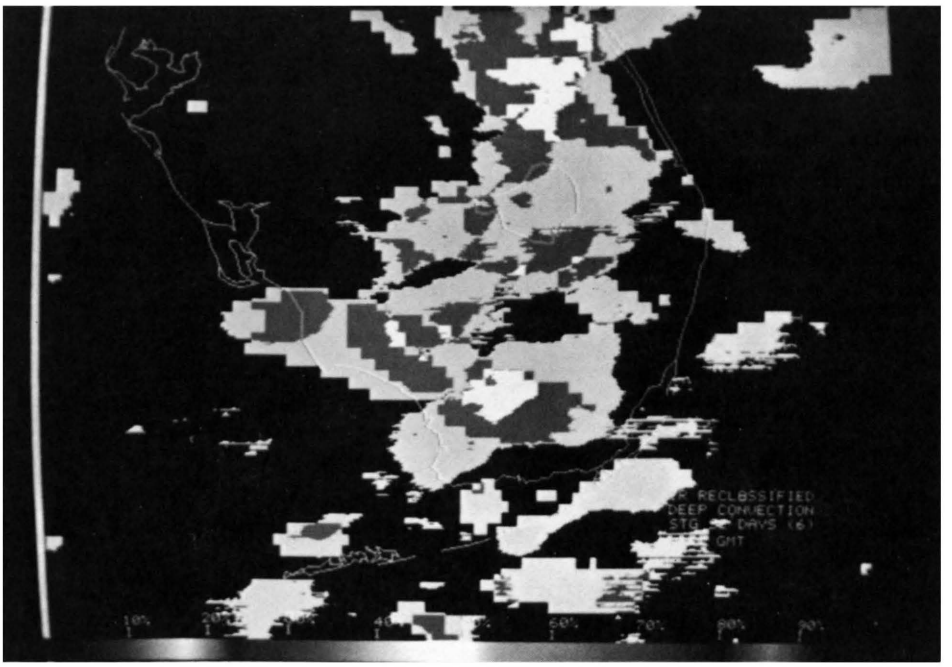


(b)

Figure 5.5. Satellite image composites by synoptic flow for (a) light southeast and (b) strong southeast synoptic classes at 1400 EST. Bar on the bottom of image relates shading to cloud frequency (on originals, a color bar is used). The number in parentheses on each image label indicates the number of images which went into creating the composite. (Color slides of all the composites are available, which more clearly illustrate the cloud composite frequencies; costs prevented reproducing these Figures in color in this report).


(a)

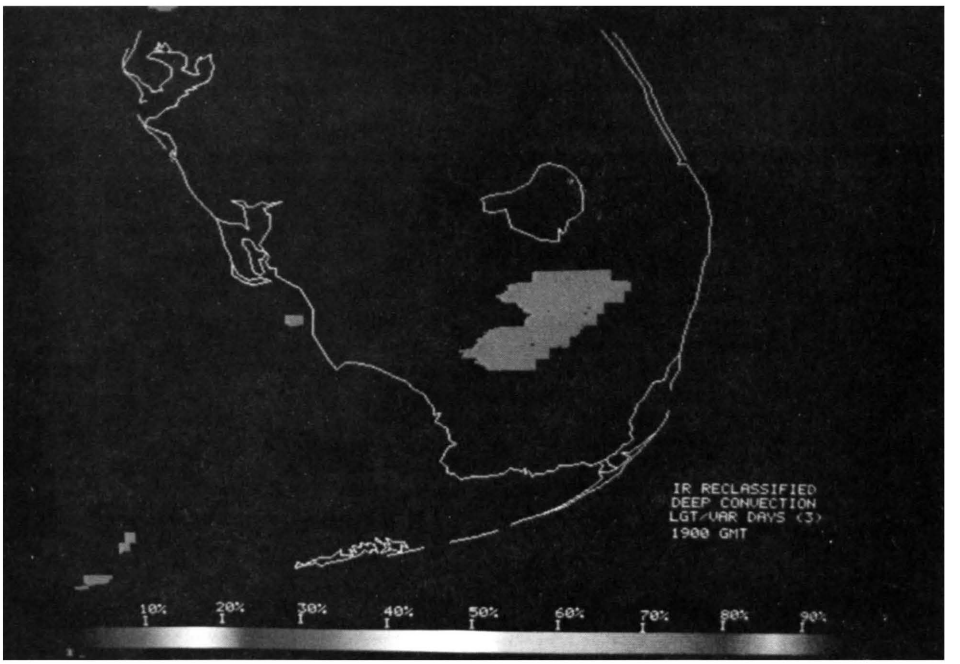


(b)

Figure 5.6. Satellite image composites by synoptic flow for (a) strong east and (b) light and variable synoptic classes at 1400 EST. Bar on the bottom of image relates shading to cloud frequency (on originals, a color bar is used). The number in parentheses on each image label indicates the number of images which went into creating the composite. (Color slides of all the composites are available, which more clearly illustrate the cloud composite frequencies; costs prevented reproducing these Figures in color in this report).

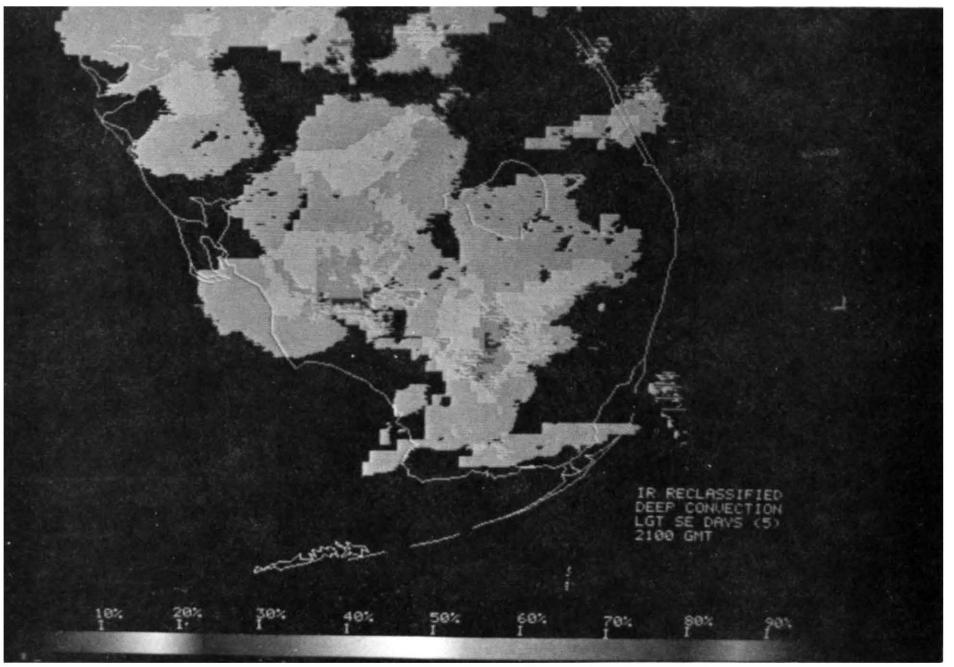


(a)

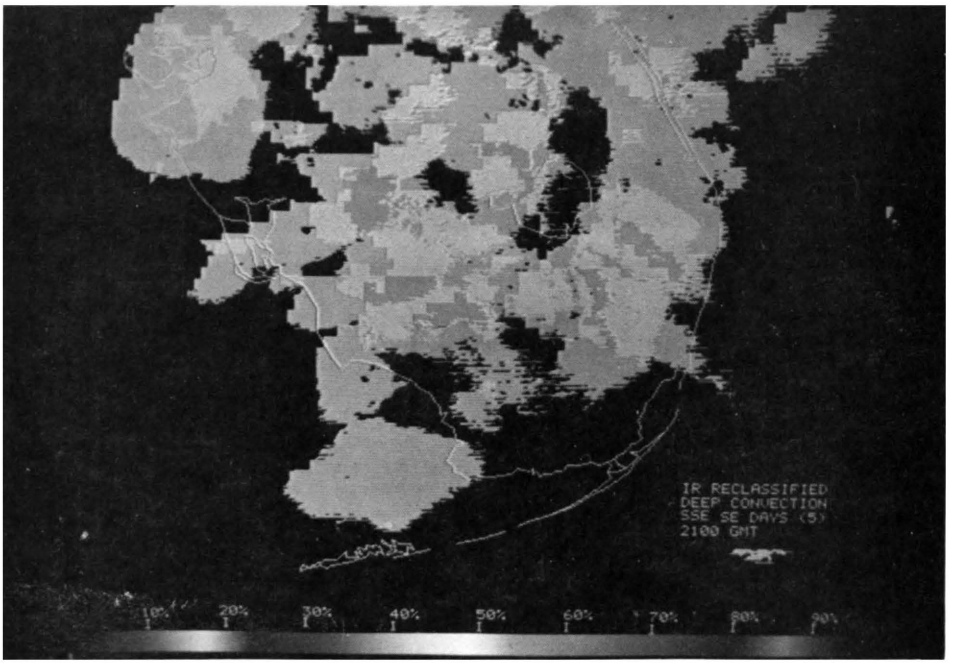


(b)

Figure 5.7. Satellite image composites by synoptic flow for (a) light southeast and (b) strong southeast synoptic classes at 1600 EST. Bar on the bottom of image relates shading to cloud frequency (on originals, a color bar is used). The number in parentheses on each image label indicates the number of images which went into creating the composite. (Color slides of all the composites are available, which more clearly illustrate the cloud composite frequencies; costs prevented reproducing these Figures in color in this report).

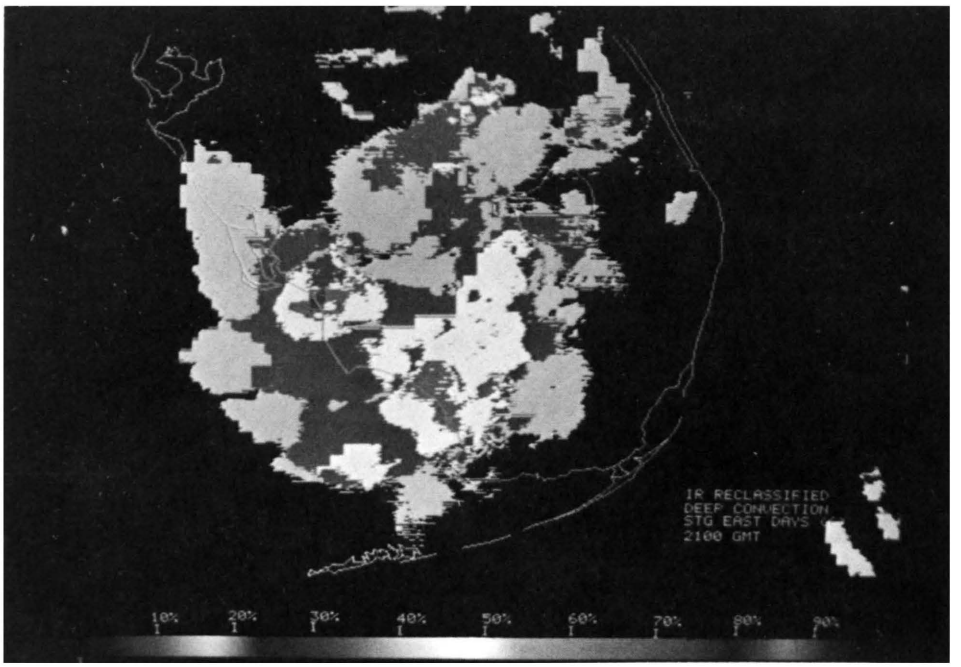


(a)

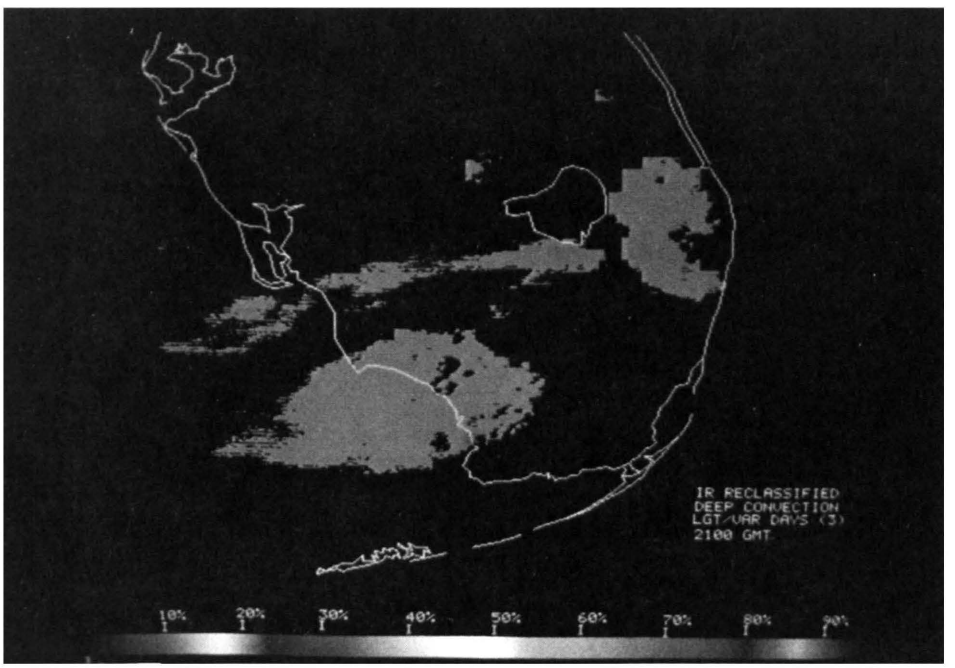


(b)

Figure 5.8. Satellite image composites by synoptic flow for (a) strong east and (b) light and variable synoptic classes at 1600 EST. Bar on the bottom of image relates shading to cloud frequency (on originals, a color bar is used). The number in parentheses on each image label indicates the number of images which went into creating the composite. (Color slides of all the composites are available, which more clearly illustrate the cloud composite frequencies; costs prevented reproducing these Figures in color in this report).

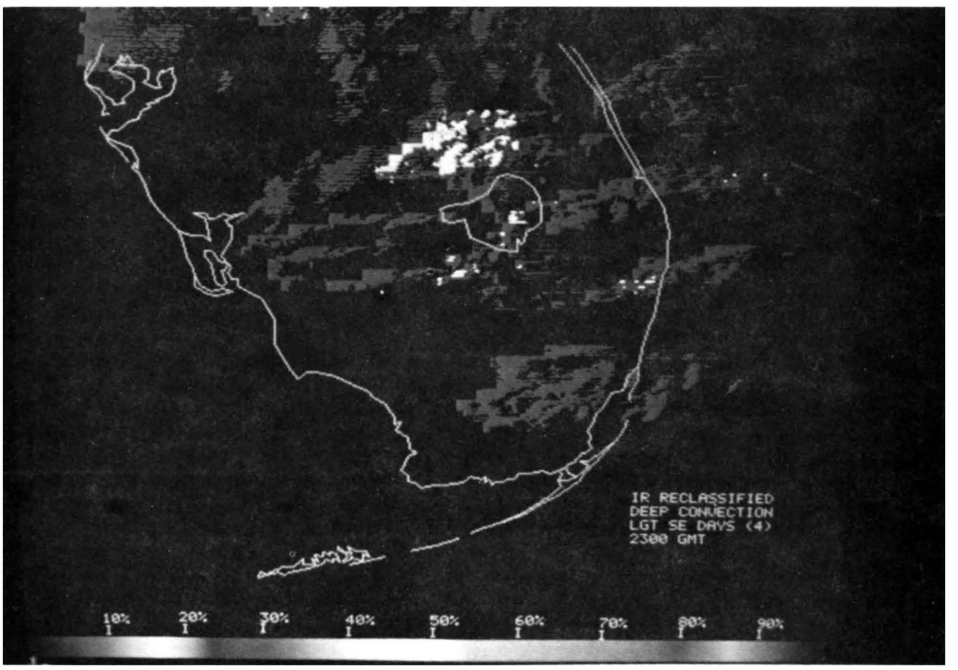


(a)

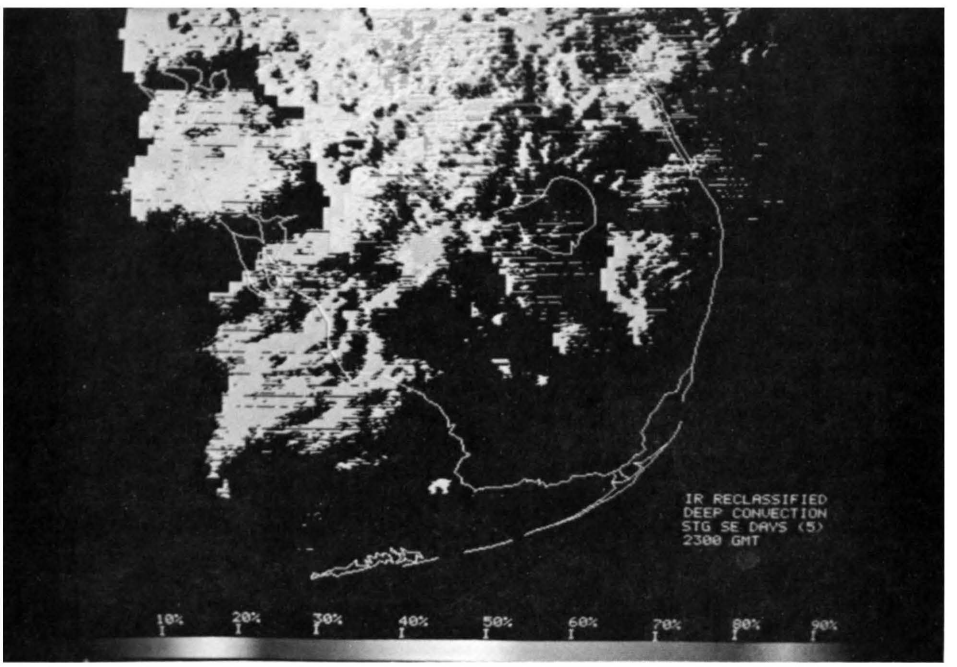


(b)

Figure 5.9. Satellite image composites by synoptic flow for (a) light southeast and (b) strong southeast synoptic classes at 1800 EST. Bar on the bottom of image relates shading to cloud frequency (on originals, a color bar is used). The number in parentheses on each image label indicates the number of images which went into creating the composite. (Color slides of all the composites are available, which more clearly illustrate the cloud composite frequencies; costs prevented reproducing these Figures in color in this report).

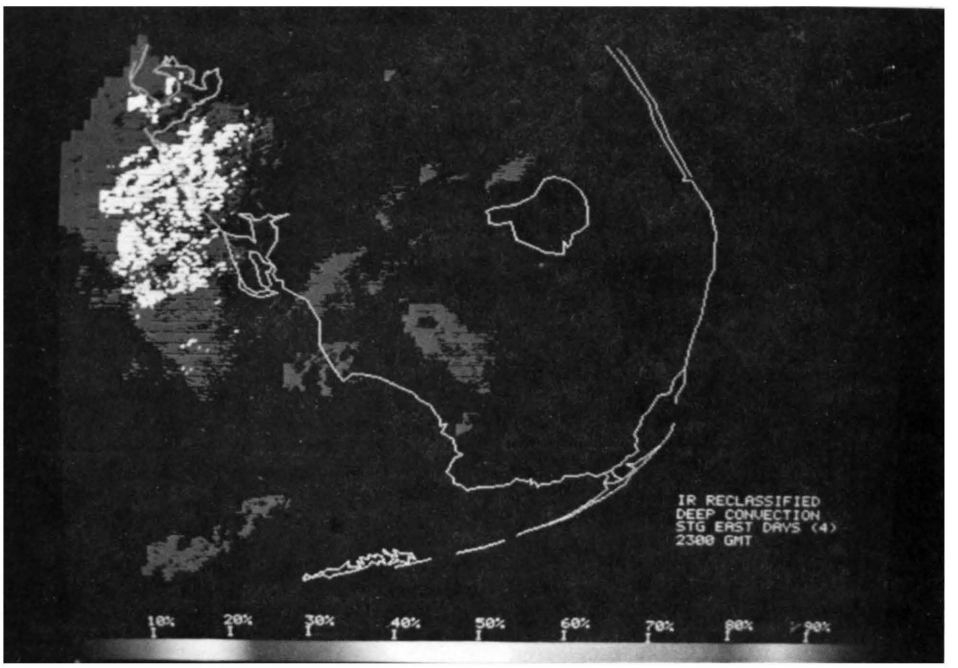


(a)

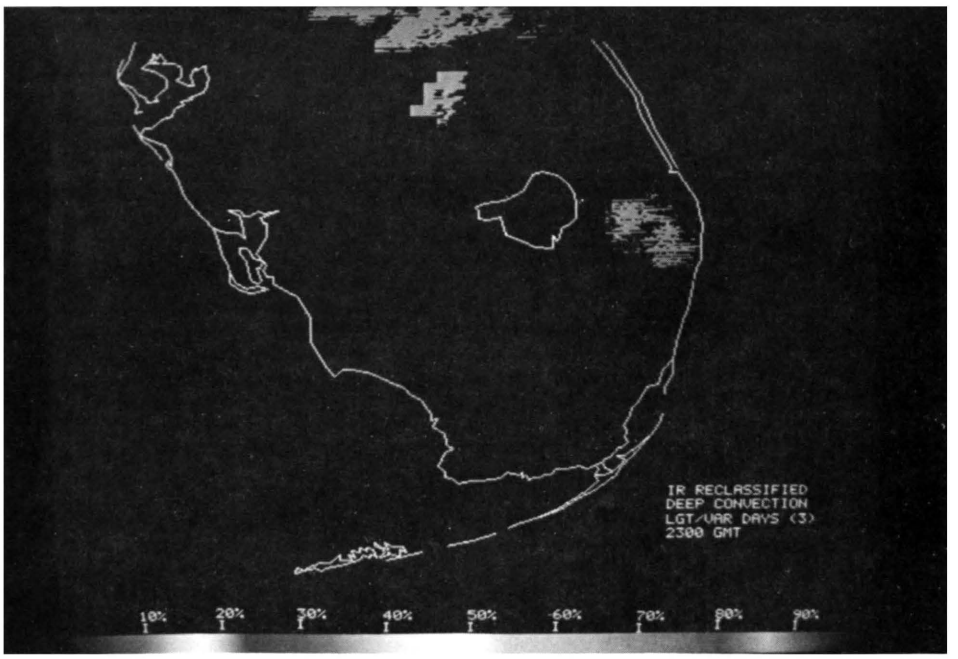


(b)

Figure 5.10. Satellite image composites by synoptic flow for (a) strong east and (b) light and variable synoptic classes at 1800 EST. Bar on the bottom of image relates shading to cloud frequency (on originals, a color bar is used). The number in parentheses on each image label indicates the number of images which went into creating the composite. (Color slides of all the composites are available, which more clearly illustrate the cloud composite frequencies; costs prevented reproducing these Figures in color in this report).

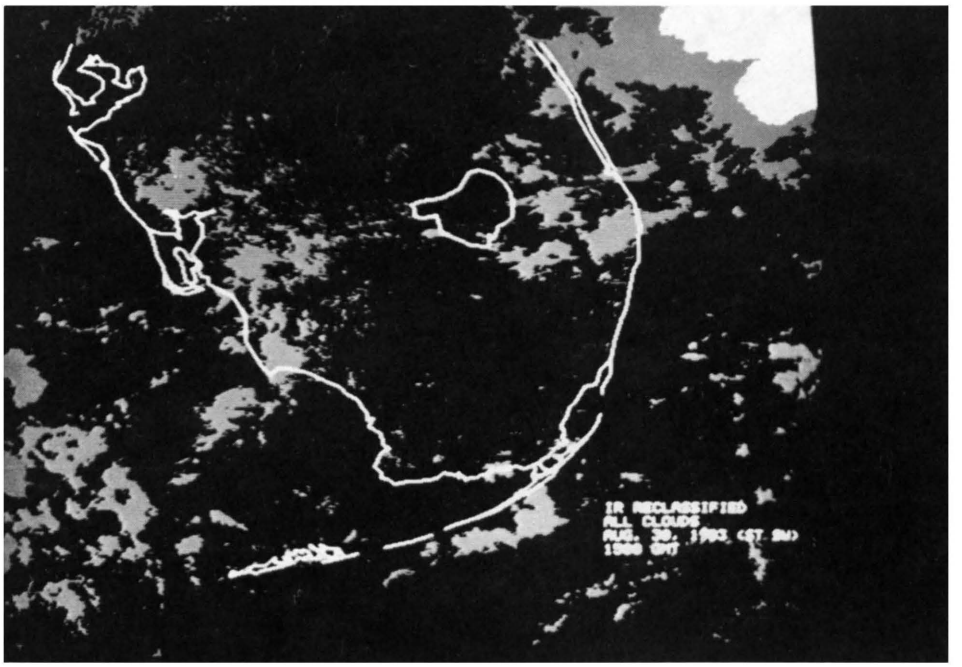


(a)

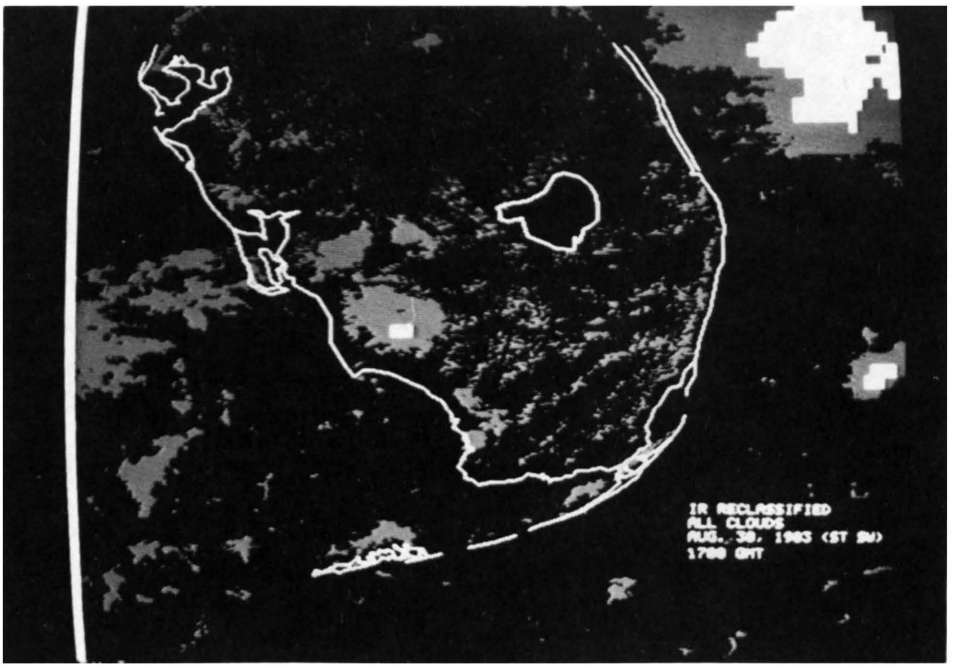


(b)

Figure 5.11. Strong southwest case image on August 30, 1983 for (a) 1000 EST and (b) 1200 EST. Images are three-shaded reprocessed images. White area locates deep convection. Grey areas locate all other clouds.

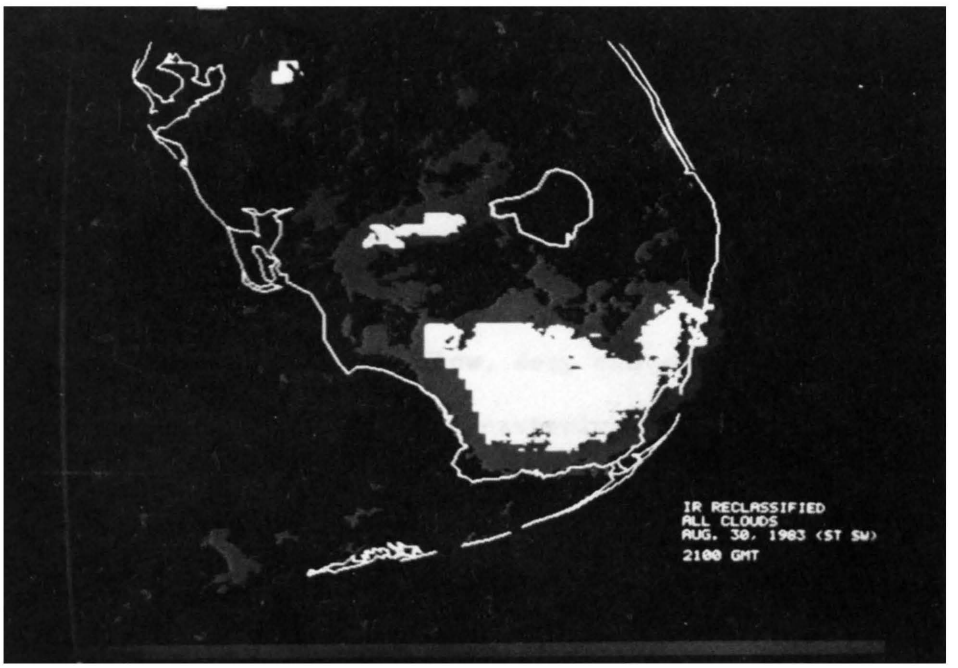


(a)


(b)

Figure 5.12. Strong southwest case image on August 30, 1983 for (a) 1600 EST and (b) 1800 EST. Images are three-shaded reprocessed images. White area locates deep convection. Grey areas locate all other clouds.

The 1200 EST image composites are shown in Figures 5.3 and 5.4. For light southeasterly flow, the only deep convective clouds to develop are in an area directly east of Lake Okeechobee, along the southern coast and along the west coast near the southernmost bay on the Florida outline shown in the figure.

For strong southeasterly flow, deep convective clouds are further inland compared to the light southeasterly clouds. Along the southern coast, convection is very active. Deep convective cloudiness is also found a little further north along the west coast and is more prevalent than for light southeasterly flow. To the north and west of Lake Okeechobee, a band of cloudiness exists.

For strong easterly and very light and variable flows at 1200 EST, little convective activity or organization is present. No deep convective clouds are found over the peninsula for light and variable flows while for strong easterly flow, small areas are found near the southern coast. The line extending over the southern part of Lake Okeechobee was determined to be associated with a cold front which moved into the area from the north on July 21. Further images for this day were not included in the undisturbed composite or the statistical studies.

The strong southwest case image at 1200 EST is presented in Figure 5.11b. Only a small area of deep convection is noted along the upwind west coast near the region of convex coastal curvature.

The 1400 EST composites are presented in Figures 5.5 and 5.6. The southeasterly composites show a high degree of organization with deep convective cloud activity paralleling the coast, especially for the light southeasterly composite. Also convection has increased

significantly from 1200 EST. For the light southeast composite, the region of convection paralleling the west coast is more continuous with higher frequencies than the east coast band. There is a concentration of clouds along the southern tip of the peninsula. To the north and west of Lake Okeechobee, a small region of frequencies greater than 30 percent exists.

For strong southeasterly flow, the convection lies further from the east coast than for the light southeasterly composite. A significant area of frequencies of 50 percent or greater lie along the southwest coast. Two maxima are seen in the cloud frequencies along the west coast. The southern one has a large area of 50 percent cloud frequencies with a small region where frequencies reach 66 percent. A small region of preferred convective cloudiness also exists along the southern shores of Lake Okeechobee while an even more preferred region is located just north and east of the lake. The strong southeast composite contains more areas of 50 percent cloud frequencies than any other image at this time.

For strong easterly days, the areas of strongly preferred convection all lie in the southwestern half of the peninsula. Clouds are seen in two areas of the west coast as was the case for the southeasterly flows. The west coast convection maxima lie closer to the coast than the maxima for the other classes. Another significant area of preferred convection is seen along the southwest coast of Lake Okeechobee.

The light and variable class exhibits little convective activity at 1400 EST. One area is found due south of the lake and parallels

the Florida east coast. No image was available for the strong southwest case at this time.

Figures 5.7 and 5.8 show the 1600 EST composites. The two maxima in cloud frequencies have propagated inland off the west coast for light southeasterly days. Cloud frequencies for these two maxima are generally equal to 60 percent with smaller areas of 80 percent.

For strong southeasterly flow, there are several regions of cloud frequencies of 60 percent. The preferred areas of convection along the west coast are further north than for the light southeast or strong east classes. Other preferred regions are found inland and parallel to the southeast coast. The eastern regions are probably new developments since they lie upwind of any convective areas noted at 1400 EST. Another preferred area of deep convective cloudiness is found along the north coast of Lake Okeechobee.

The strong east composite at 1600 EST reveals a strong signal for preferred regions of deep convective clouds along the southwest coast with two distinct maxima with large areas of cloud frequencies equal to or greater than 50 percent. The southern maximum has not moved from the 1400 EST image while the northern maximum has moved further north. A region of high frequencies extends from the southern maximum to Lake Okeechobee where it meets another region of somewhat lower frequencies which parallel the east coast.

The light and variable composite at 1600 EST shows an area of cloudiness just east of Lake Okeechobee. The area indicated at 1400 EST has apparently moved to the west coast where another area of cloudiness is located.

For the strong southwest case at 1600 EST (Fig. 5.12a), a large area of deep convection has developed covering most of the southern tip of the peninsula. Also seen is a small region of deep convective clouds forming just east of Tampa Bay.

The 1800 EST southeasterly composites shown in Figures 5.9 and 5.10 illustrate that almost all of the deep convective cloudiness has dissipated over the southern half of the peninsula. Some new deep convection has developed just to the north of Lake Okeechobee for light southeasterly and further north for strong southeasterly flow.

Clouds in the south have dissipated for strong easterly flow as well. The previously cloud-free northwest coast now contains most of the convective cloud activity. Some of this convection has been advected offshore by the synoptic flow.

For light and variable flow at 1800 EST, convection just east of Lake Okeechobee has remained stationary from the earlier composite but it has diminished in size. Convective clouds along the west coast have completely died out by this time.

By 1800 EST for the strong southwest case (Fig. 5.12b), cloudiness is found further east of Tampa Bay while the southern convective clouds have dissipated.

## 5.2 The Results of the Numerical Model and Comparisons with the Satellite Image Composites

The three-dimensional numerical model described in Chapter 3 was integrated for the light and strong southeast, strong east, light and variable and strong southwest flow regimes for South Florida. Simulations for all 5 flow regimes have not previously been done with this version of the model. The data needed to initialize the model for

each case was presented in Section 3.4. The model physics incorporates the peninsula scale sea breeze circulation due to the land-sea thermal contrasts along with its interaction with the large-scale synoptic flow. As discussed earlier, variations of the ground surface type are also accounted for by the model. Figures 5.13, 5.14, and 5.15 show the spatial variations of soil type, vegetation type and the amount of vegetation coverage, respectively, over Florida. These data were used as a bottom boundary for the model.

Comparisons between the results of each model simulation will illustrate the variations in the position and magnitude of the sea breeze convergence zones as a function of the synoptic flow. Comparisons of the model predicted convergence patterns with the cloud patterns observed from the satellite composites will help identify physical explanations for the spatial variations in the deep convective cloud composite images.

Figures 5.16 through 5.30 present the model output wind vectors at 25 m, the vertical velocity fields at 1 km, and the moisture availability at 500 m which is defined by the difference between saturated equivalent and equivalent potential temperature ($\theta_{es}$-$\theta_{e}$), for the first four flow regimes listed above. The results for the strong southwest run are shown in Figures 5.28 through 5.30. The model results are given at 1230, 1430, 1630, and 1830 EST which are one-half hour after the corresponding satellite images.

As shown in Figure 5.16, by 1230 EST onshore flow has begun along the west coast in all cases. Also the east coast sea breeze has moved inland by this time. For light and strong southeasterly, and light and variable model simulations, the east coast sea breeze has its


Figure 5.13. Soil types over South Florida used to define the bottom boundary for model runs (from McCumber, 1980).

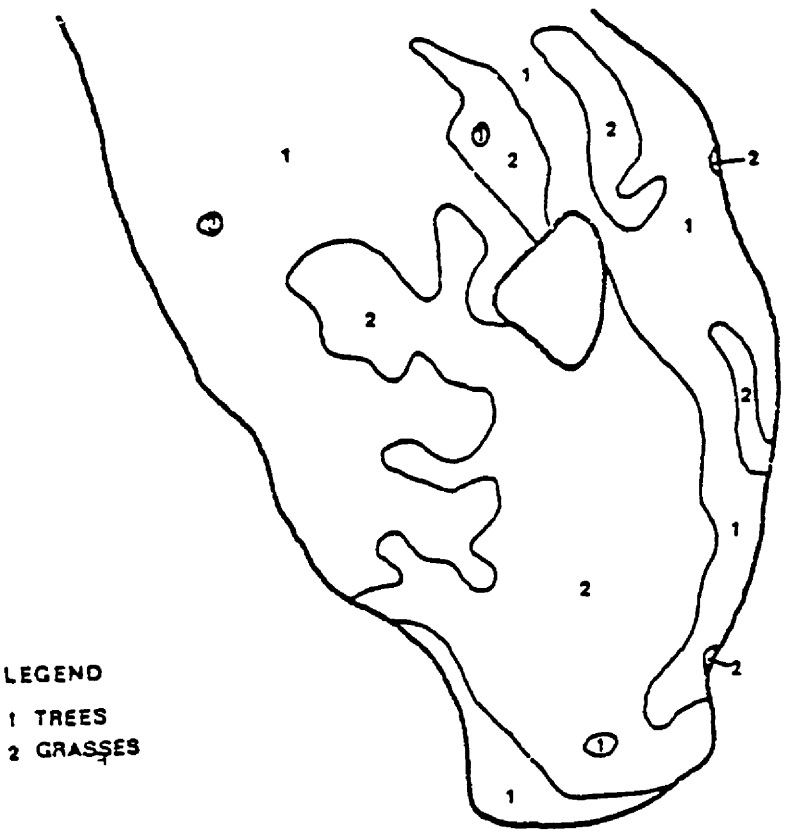


Figure 5.14. Vegetation types over South Florida used to define the bottom boundaries for model runs (from McCumber, 1980).

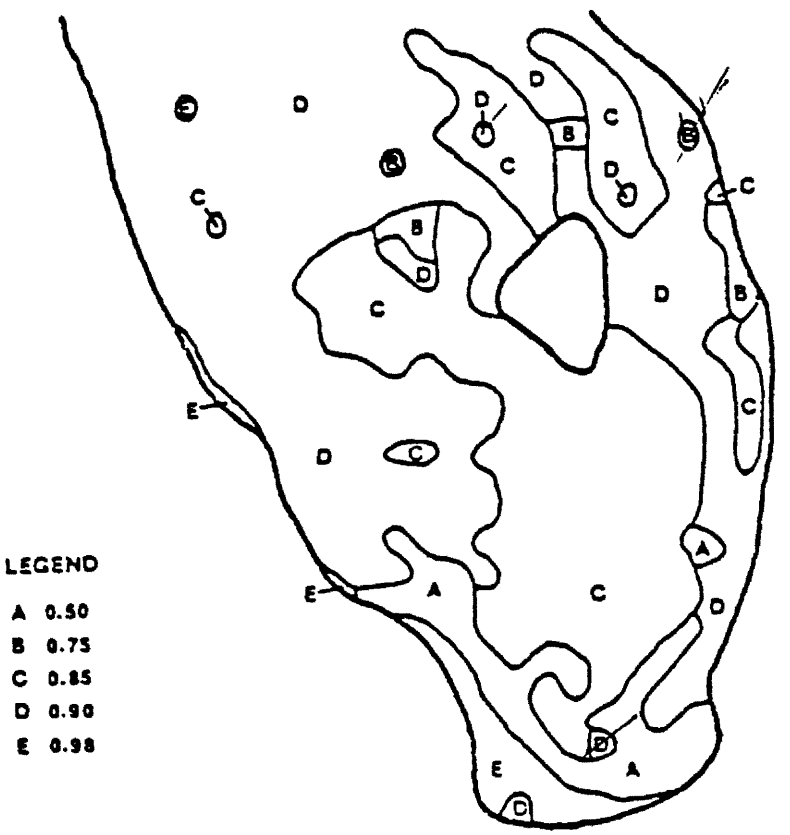


Figure 5.15. Vegetation shielding coverage ($\sigma$) over South Florida used to define the bottom boundaries for model runs (from McCumber, 1980).

Figure 5.16. Model-predicted wind vectors at 25 m for (a) light southeast, (b) strong southeast, (c) strong east, and (d) very light and variable synoptic wind simulations at 1230 EST. A vector of one grid length equals 8 m/s.

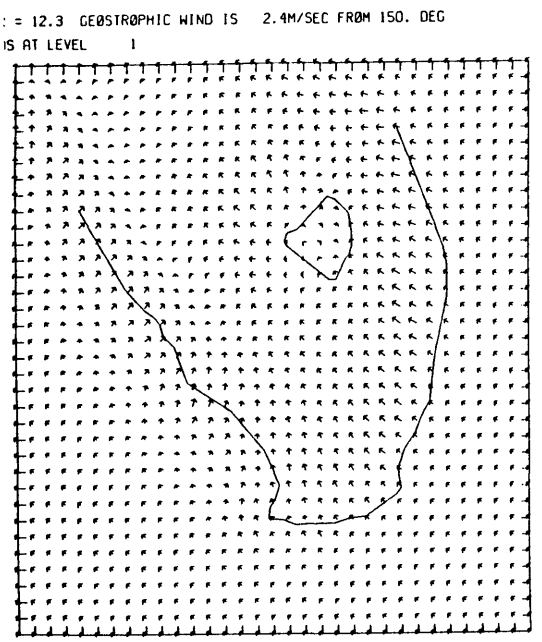
: = 12.3 GEØSTRØPHIC WIND IS 2.4M/SEC FRØM 150. DEG
IS AT LEVEL 1

(a)

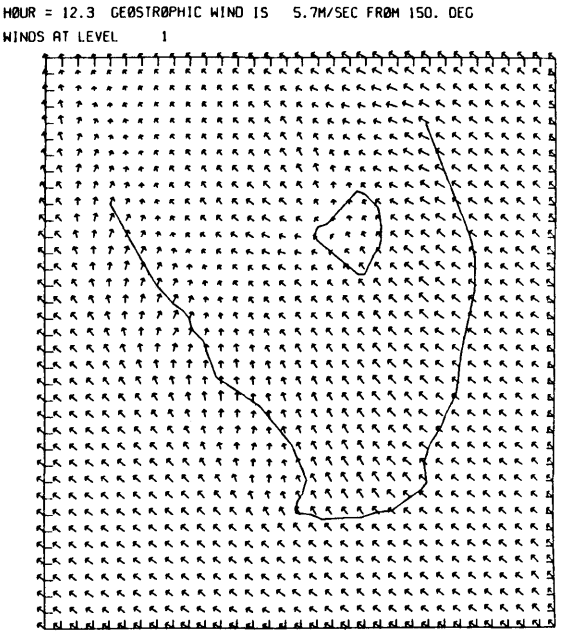
HØUR = 12.3 GEØSTRØPHIC WIND IS 5.7M/SEC FRØM 150. DEG
WINDS AT LEVEL 1

(b)

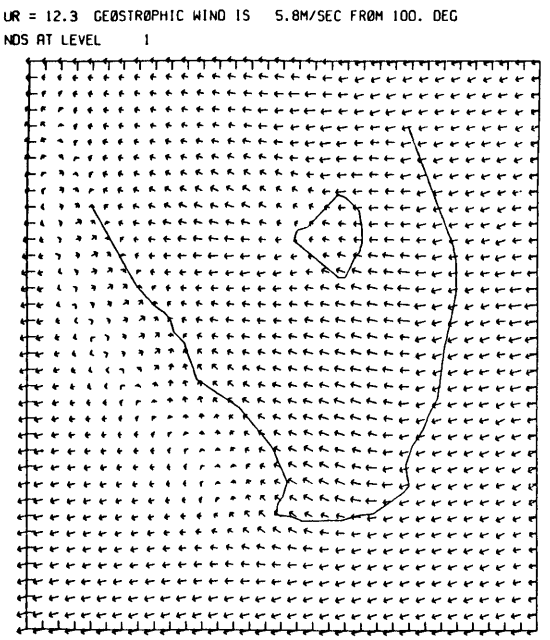
UR = 12.3 GEØSTRØPHIC WIND IS 5.8M/SEC FRØM 100. DEG
NDS AT LEVEL 1

(c)

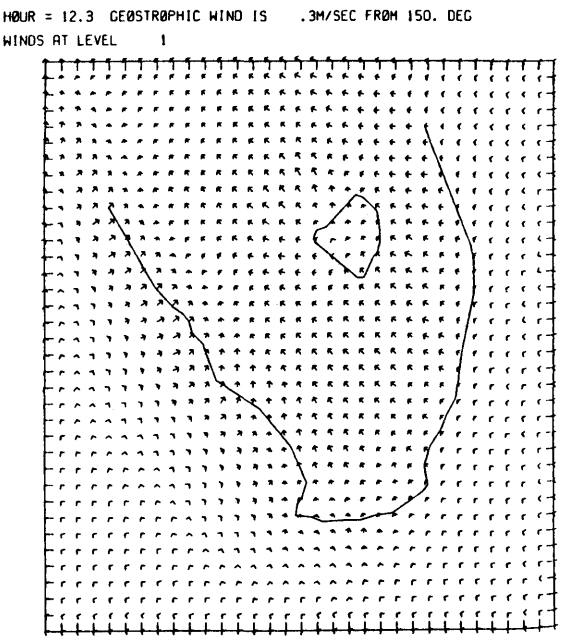
HØUR = 12.3 GEØSTRØPHIC WIND IS .3M/SEC FRØM 150. DEG
WINDS AT LEVEL 1

(d)

Figure 5.17. Model-predicted vertical velocity fields in cm/s at 1 km for (a) light southeast, (b) strong southeast, (c) strong east, and (d) very light and variable synoptic wind simulations at 1230 EST. Contour interval is 3 cm/s.

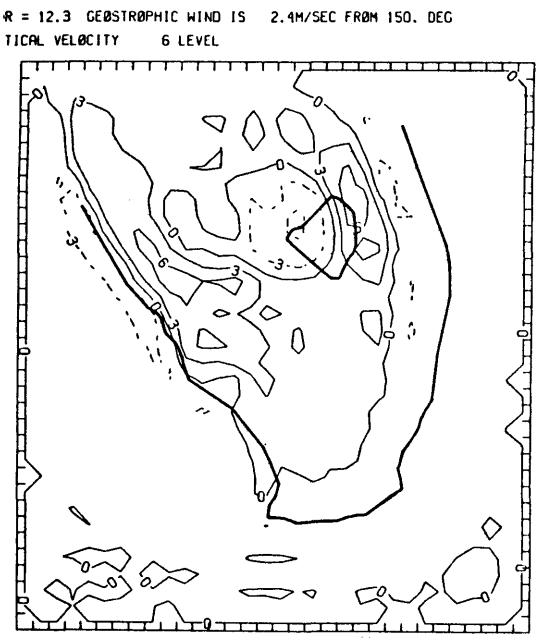
R = 12.3 GEØSTRØPHIC WIND IS 2.4M/SEC FRØM 150. DEG
TICAL VELØCITY 6 LEVEL

(a)

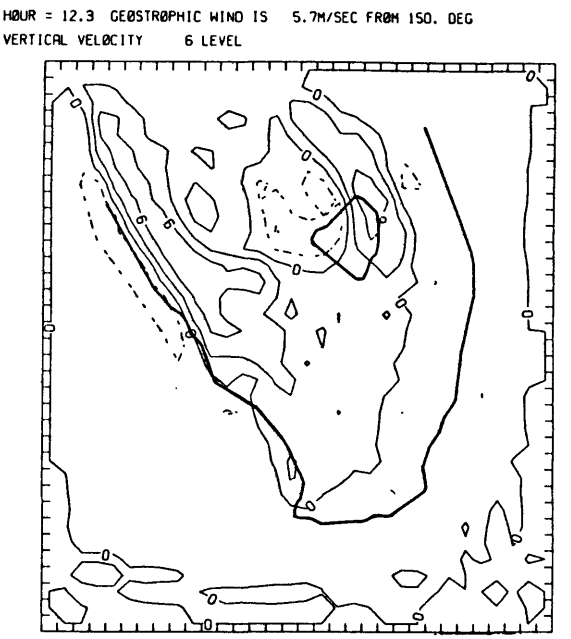
HØUR = 12.3 GEØSTRØPHIC WIND IS 5.7M/SEC FRØM 150. DEG
VERTICAL VELØCITY 6 LEVEL

(b)

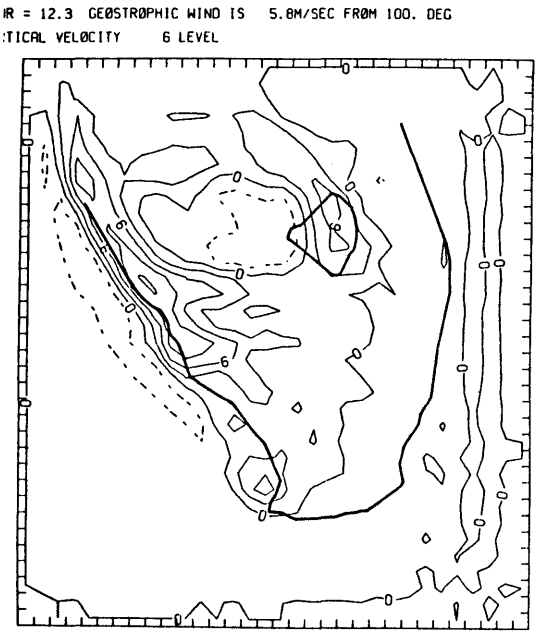
R = 12.3 GEØSTRØPHIC WIND IS 5.8M/SEC FRØM 100. DEG
TICAL VELØCITY 6 LEVEL

(c)

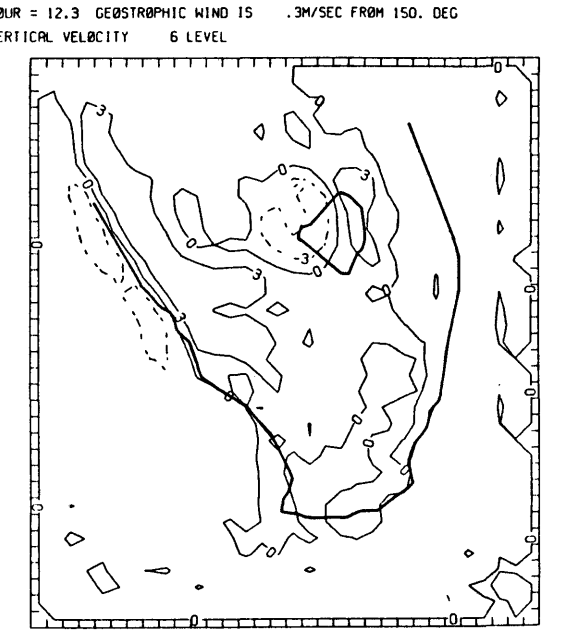
HØUR = 12.3 GEØSTRØPHIC WIND IS .3M/SEC FRØM 150. DEG
VERTICAL VELØCITY 6 LEVEL

(d)

Figure 5.18. Model-predicted moisture availability fields ($\theta_{es}-\theta_{e}$) at 500 m for (a) light southeast, (b) strong southeast, (c) strong east, and (d) very light and variable synoptic wind simulations at 1230 EST. Contour interval is 4°K.

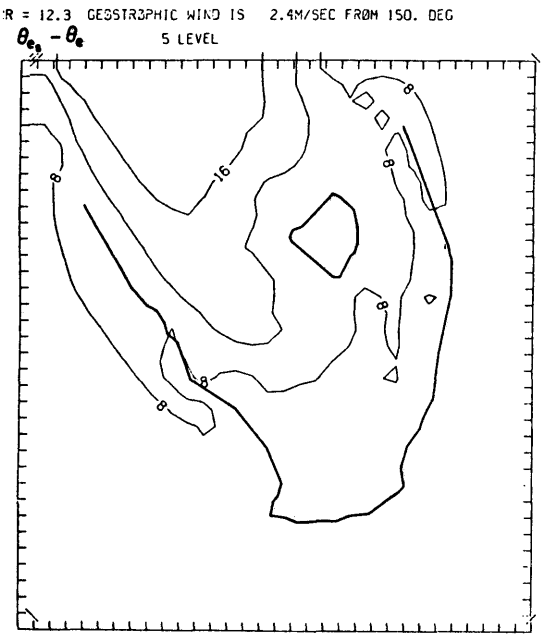
:R = 12.3 GEØSTRØPHIC WIND IS 2.4M/SEC FRØM 150. DEG
$\theta_{e_s} - \theta_e$
5 LEVEL
8
16
8
8
8
8

(a)

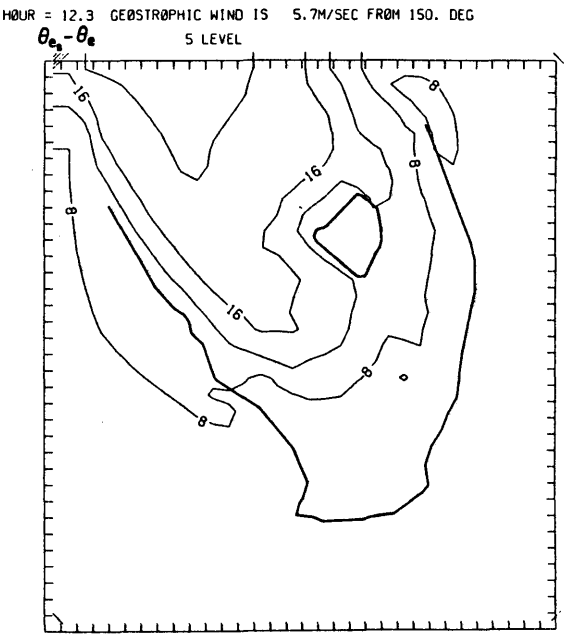
HØUR = 12.3 GEØSTRØPHIC WIND IS 5.7M/SEC FRØM 150. DEG
$\theta_{e_s} - \theta_e$
5 LEVEL
8
16
8
16
8
8

(b)

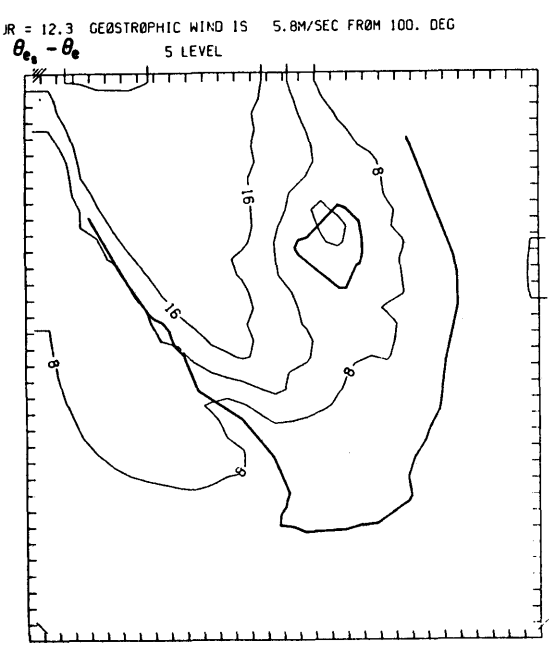
JR = 12.3 GEØSTRØPHIC WIND IS 5.8M/SEC FRØM 100. DEG
$\theta_{e_s} - \theta_e$
5 LEVEL
8
16
16
8
8
8

(c)

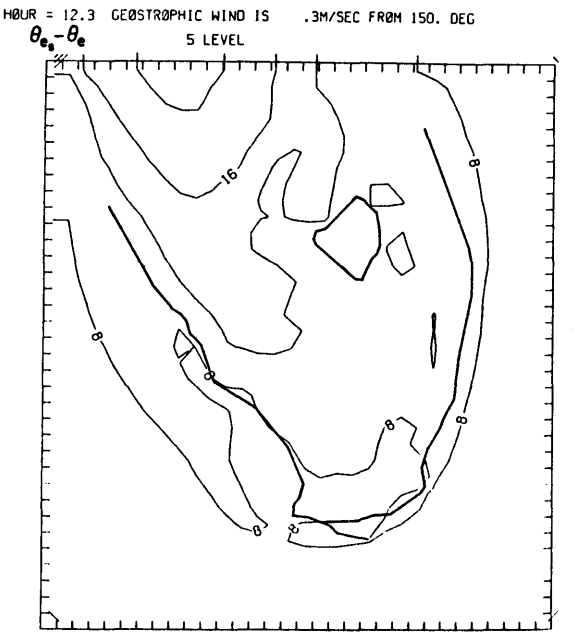
HØUR = 12.3 GEØSTRØPHIC WIND IS .3M/SEC FRØM 150. DEG
$\theta_{e_s} - \theta_e$
5 LEVEL
8
16
8
8
8
8

(d)

Figure 5.19. Model-predicted wind vectors at 25 m for (a) light southeast, (b) strong southeast, (c) strong east, and (d) very light and variable synoptic wind simulations at 1430 EST. A vector of one grid length equals 8 m/s.

JR = 14.3 GEØSTRØPHIC WIND IS 2.4M/SEC FRØM 150. DEG
NDS AT LEVEL 1

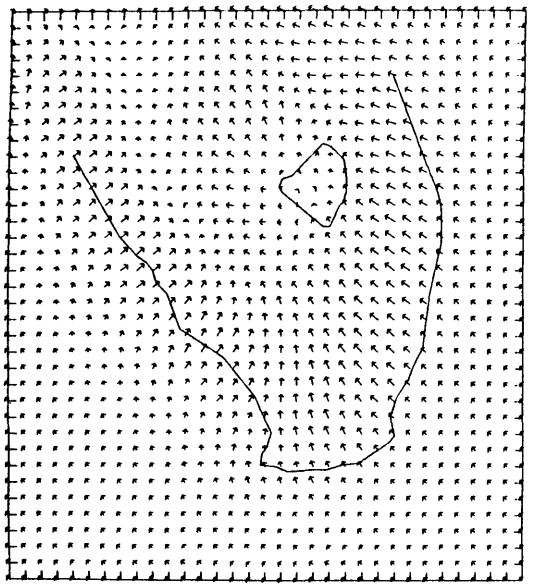

(a)

HØUR = 14.3 GEØSTRØPHIC WIND IS 5.7M/SEC FRØM 150. DEG
WINDS AT LEVEL 1

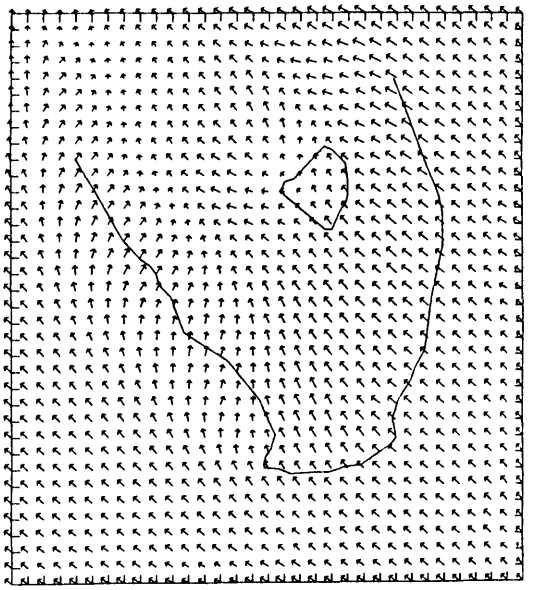

(b)

R = 14.3 GEØSTRØPHIC WIND IS 5.8M/SEC FRØM 100. DEG
DS AT LEVEL 1

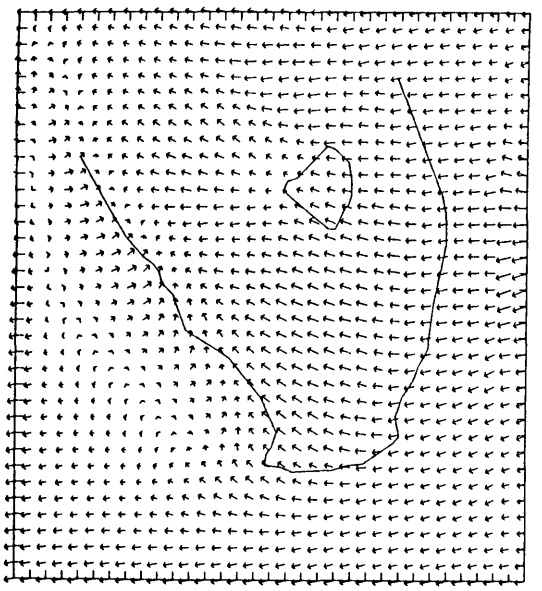

(c)

HØUR = 14.3 GEØSTRØPHIC WIND IS .3M/SEC FRØM 150. DEG
WINDS AT LEVEL 1

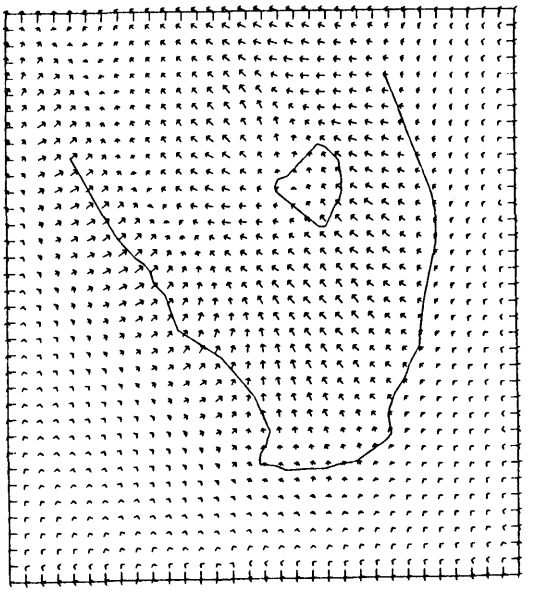

(d)

Figure 5.20. Model-predicted vertical velocity fields in cm/s at 1 km for (a) light southeast, (b) strong southeast, (c) strong east, and (d) very light and variable synoptic wind simulations at 1430 EST. Contour interval is 3 cm/s.

ØUR = 14.3 GEØSTRØPHIC WIND IS 2.4M/SEC FRØM 150. DEG
ERTICAL VELØCITY 6 LEVEL

(a)

HØUR = 14.3 GEØSTRØPHIC WIND IS 5.7M/SEC FRØM 150. DEG
VERTICAL VELØCITY 6 LEVEL

(b)

HØUR = 14.3 GEØSTRØPHIC WIND IS 5.8M/SEC FRØM 100. DEG
VERTICAL VELØCITY 6 LEVEL

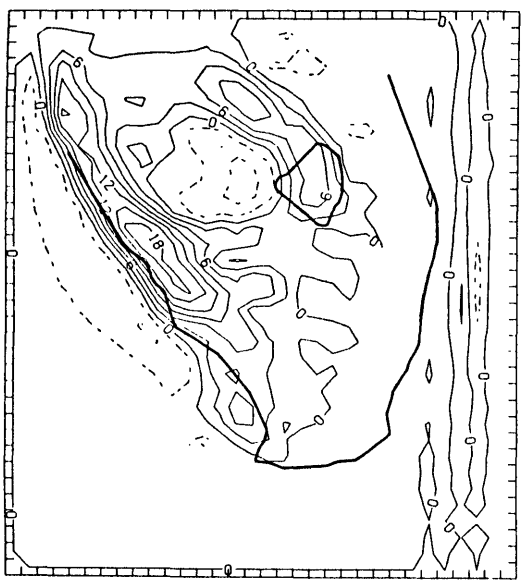

(c)

HØUR = 14.3 GEØSTRØPHIC WIND IS .3M/SEC FRØM 150. DEG
VERTICAL VELØCITY 6 LEVEL

(d)

Figure 5.21. Model-predicted moisture availability fields ($\theta_{es} - \theta_e$) at 500 m for (a) light southeast, (b) strong southeast, (c) strong east, and (d) very light and variable synoptic wind simulations at 1430 EST. Contour interval is 4°K.

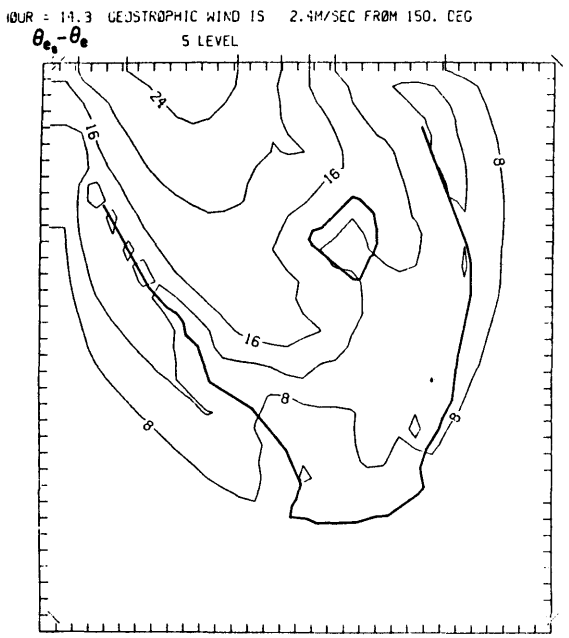
HOUR = 14.3 GEOSTROPHIC WIND IS 2.4M/SEC FROM 150. DEG
$\theta_{e_s}-\theta_e$
5 LEVEL
24
16
8

(a)

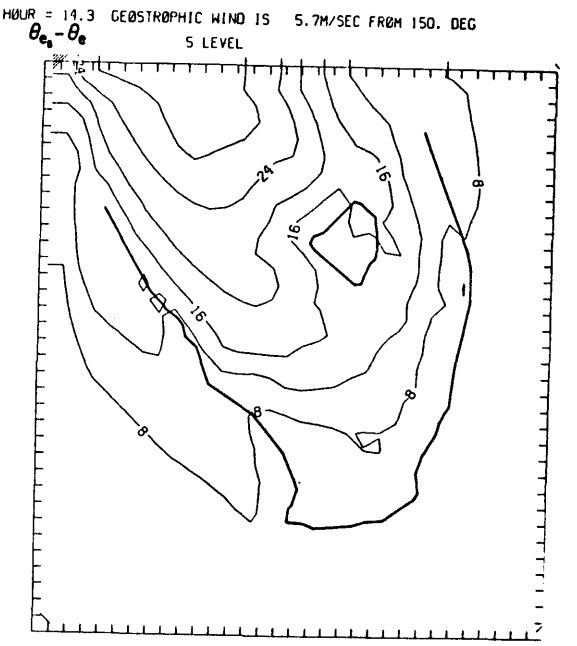
HOUR = 14.3 GEOSTROPHIC WIND IS 5.7M/SEC FROM 150. DEG
$\theta_{e_s}-\theta_e$
5 LEVEL
24
16
8

(b)

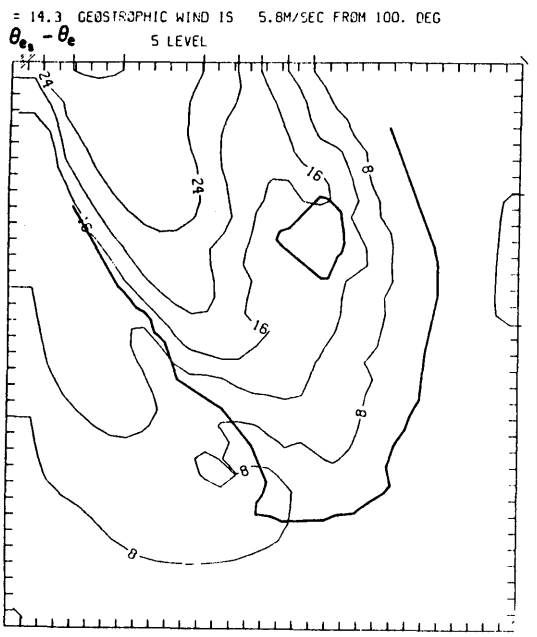
= 14.3 GEOSTROPHIC WIND IS 5.8M/SEC FROM 100. DEG
$\theta_{e_s}-\theta_e$
5 LEVEL
24
16
8

(c)

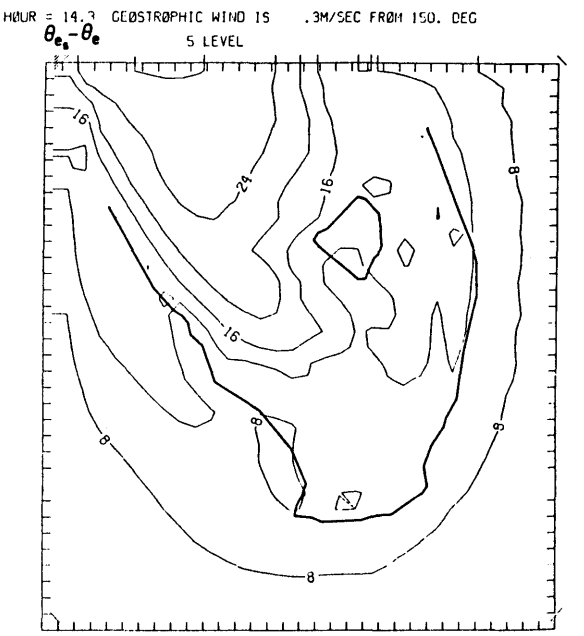
HOUR = 14.3 GEOSTROPHIC WIND IS .3M/SEC FROM 150. DEG
$\theta_{e_s}-\theta_e$
5 LEVEL
24
16
8

(d)

Figure 5.22. Model-predicted wind vectors at 25 m for (a) light southeast, (b) strong southeast, (c) strong east, and (d) very light and variable synoptic wind simulations at 1630 EST. A vector of one grid length equals 8 m/s.

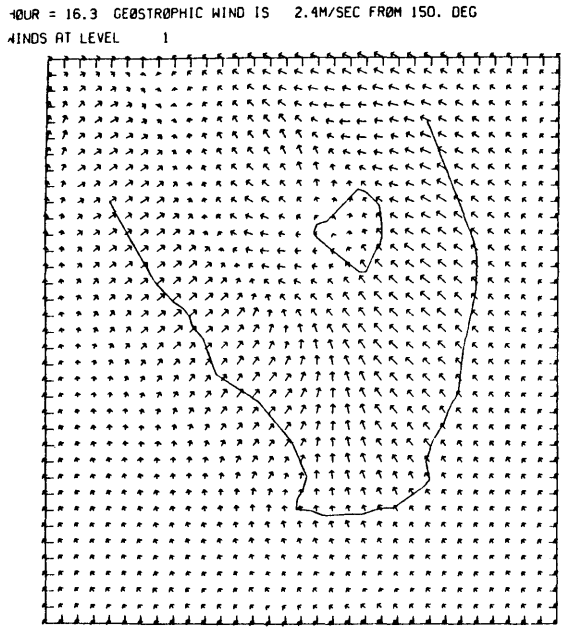
ØUR = 16.3 GEØSTRØPHIC WIND IS 2.4M/SEC FRØM 150. DEG
INDS AT LEVEL 1

(a)

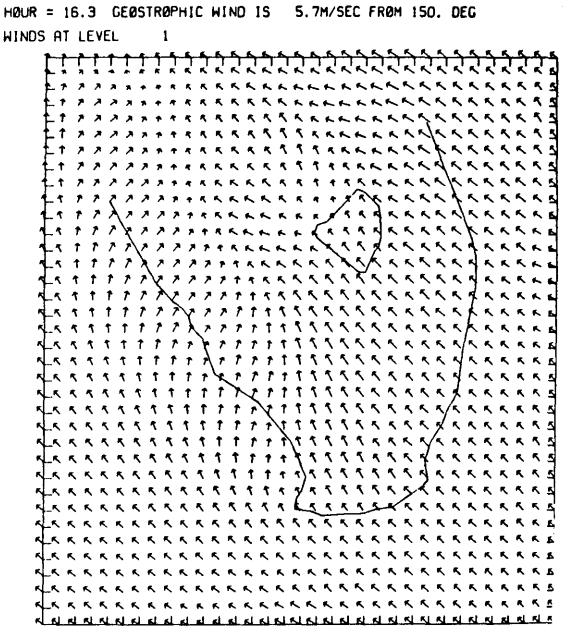
HØUR = 16.3 GEØSTRØPHIC WIND IS 5.7M/SEC FRØM 150. DEG
WINDS AT LEVEL 1

(b)

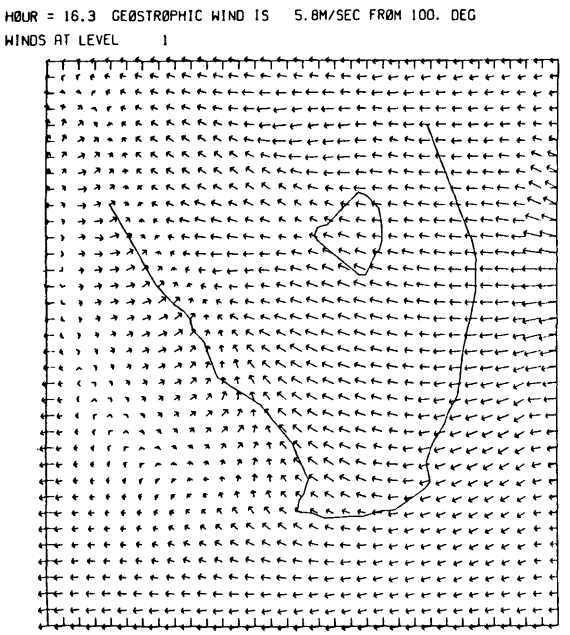
HØUR = 16.3 GEØSTRØPHIC WIND IS 5.8M/SEC FRØM 100. DEG
WINDS AT LEVEL 1

(c)

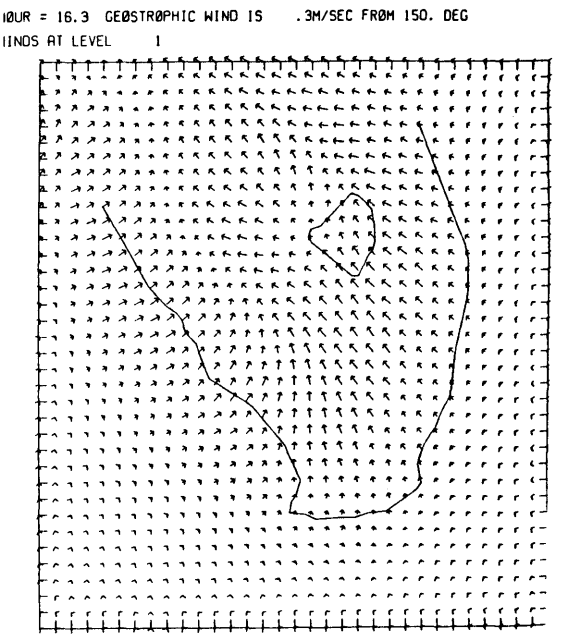
ØUR = 16.3 GEØSTRØPHIC WIND IS .3M/SEC FRØM 150. DEG
INDS AT LEVEL 1

(d)

Figure 5.23. Model-predicted vertical velocity fields in cm/s at 1 km for (a) light southeast, (b) strong southeast, (c) strong east, and (d) very light and variable synoptic wind simulations at 1630 EST. Contour interval is 3 cm/s.

ØUR = 16.3 GEØSTRØPHIC WIND IS 2.4M/SEC FRØM 150. DEG
ERTICAL VELØCITY 6 LEVEL

(a)

HØUR = 16.3 GEØSTRØPHIC WIND IS 5.7M/SEC FRØM 150. DEG
VERTICAL VELØCITY 6 LEVEL

(b)

R = 16.3 GEØSTRØPHIC WIND IS 5.8M/SEC FRØM 100. DEG
TICAL VELØCITY 6 LEVEL

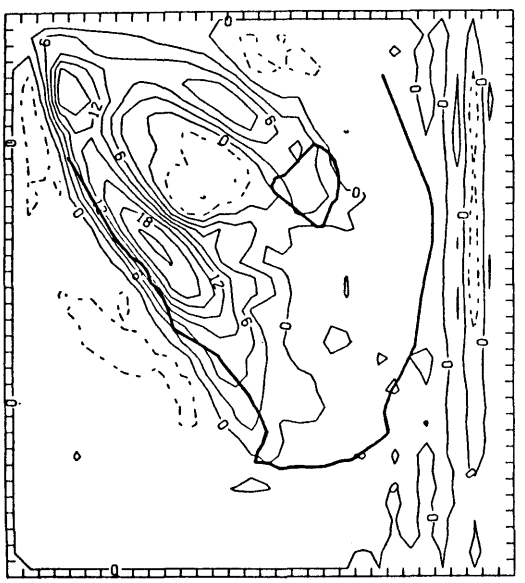

(c)

HØUR = 16.3 GEØSTRØPHIC WIND IS .3M/SEC FRØM 150. DEG
VERTICAL VELØCITY 6 LEVEL

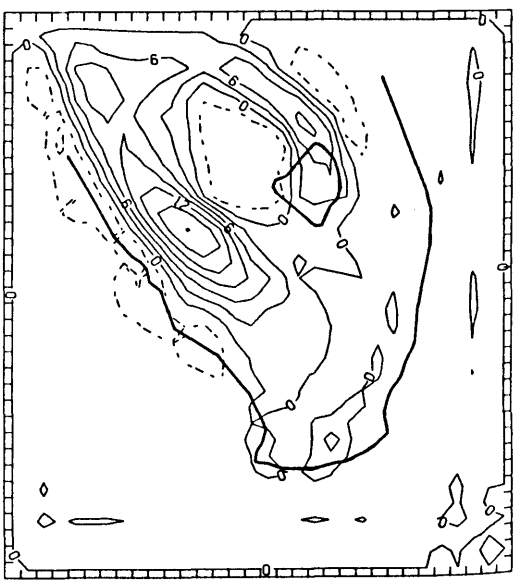

(d)

Figure 5.24. Model-predicted moisture availability fields ($\theta_{es} - \theta_e$) at 500 m for (a) light southeast, (b) strong southeast, (c) strong east, and (d) very light and variable synoptic wind simulations at 1630 EST. Contour interval is 4°K.

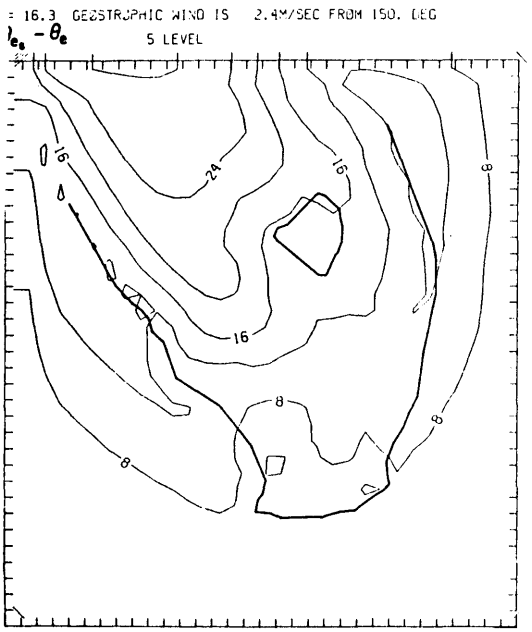
= 16.3 GEØSTRØPHIC WIND IS 2.4M/SEC FRØM 150. DEG
$\theta_{e_s} - \theta_e$
5 LEVEL
16
24
16
8
16
8
8
8

(a)

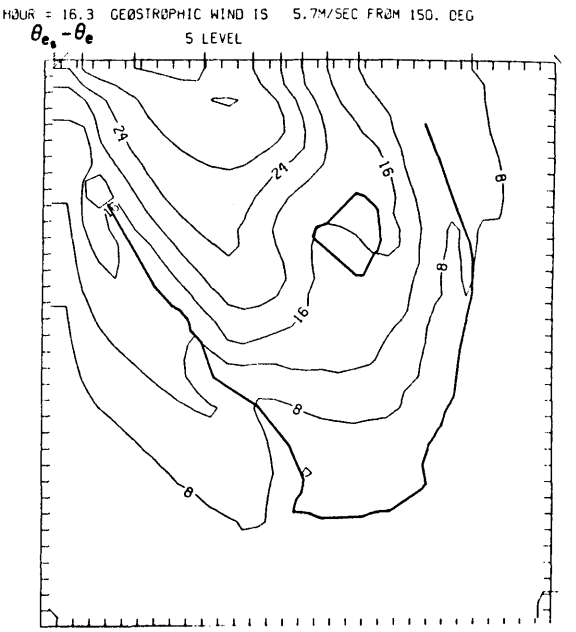
HØUR = 16.3 GEØSTRØPHIC WIND IS 5.7M/SEC FRØM 150. DEG
$\theta_{e_s} - \theta_e$
5 LEVEL
24
24
16
8
16
8
8

(b)

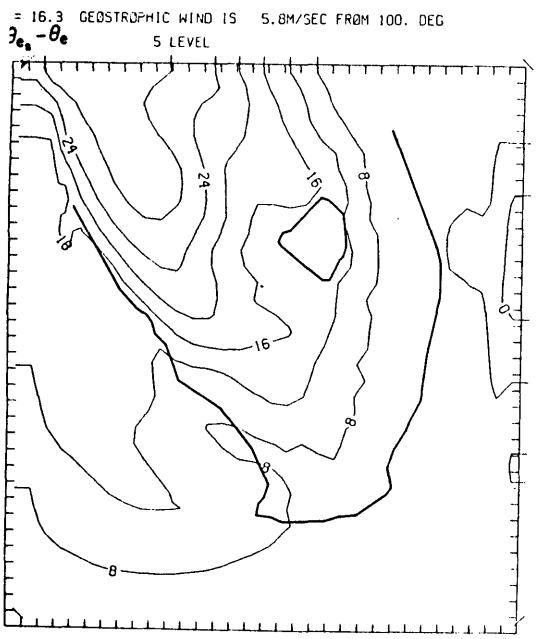
= 16.3 GEØSTRØPHIC WIND IS 5.8M/SEC FRØM 100. DEG
$\theta_{e_s} - \theta_e$
5 LEVEL
24
24
16
8
16
0
16
8
8
8

(c)

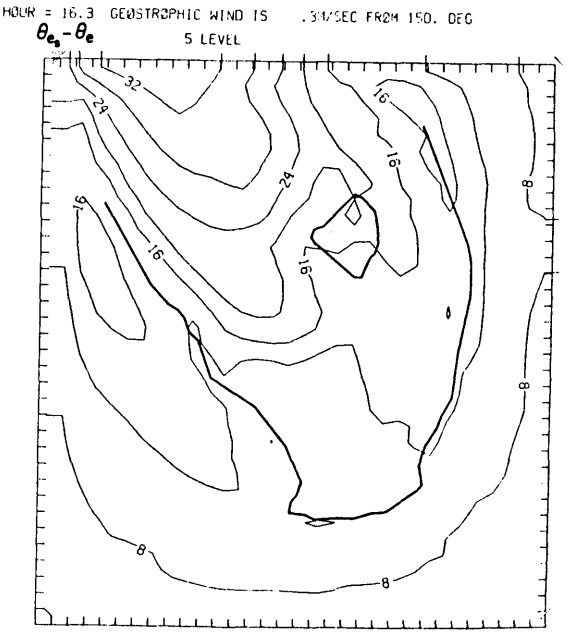
HØUR = 16.3 GEØSTRØPHIC WIND IS .3M/SEC FRØM 150. DEG
$\theta_{e_s} - \theta_e$
5 LEVEL
32
24
16
24
16
8
8
16
16
8
8

(d)

Figure 5.25. Model-predicted wind vectors at 25 m for (a) light southeast, (b) strong southeast, (c) strong east, and (d) very light and variable synoptic wind simulations at 1830 EST. A vector of one grid length equals 8 m/s.

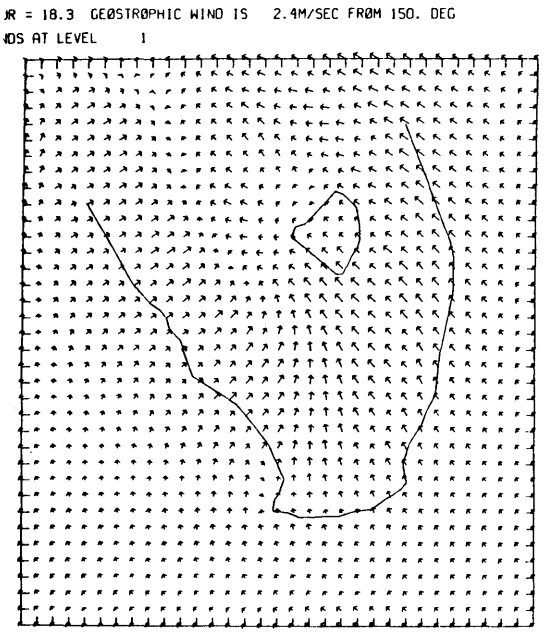
JR = 18.3 GEØSTRØPHIC WIND IS 2.4M/SEC FRØM 150. DEG
NDS AT LEVEL 1

(a)

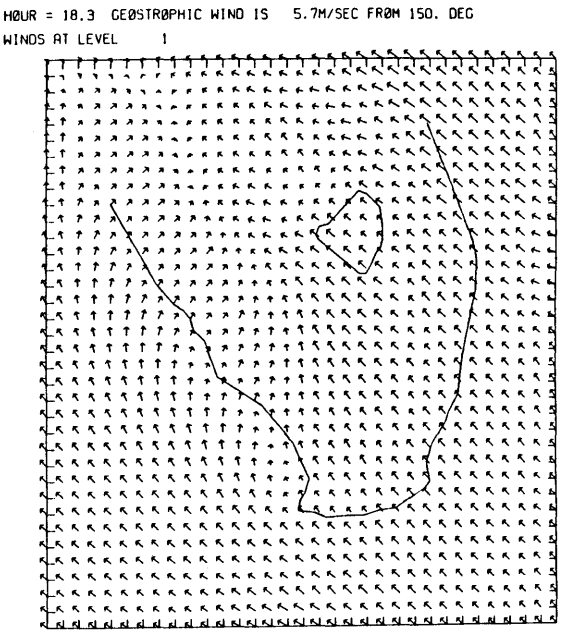
HØUR = 18.3 GEØSTRØPHIC WIND IS 5.7M/SEC FRØM 150. DEG
WINDS AT LEVEL 1

(b)

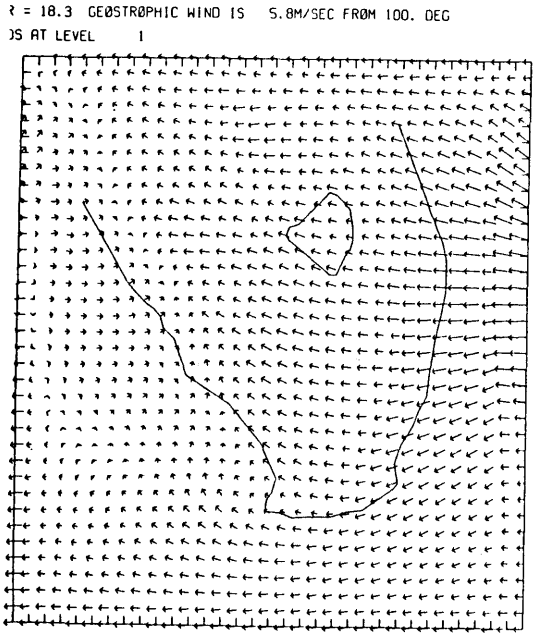
R = 18.3 GEØSTRØPHIC WIND IS 5.8M/SEC FRØM 100. DEG
DS AT LEVEL 1

(c)

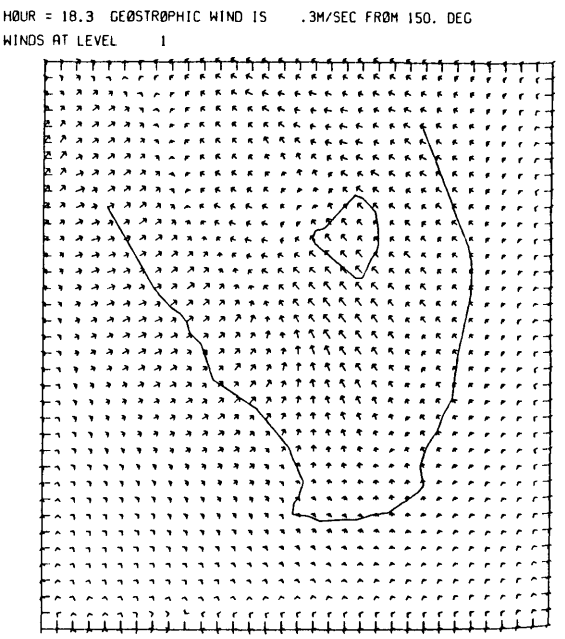
HØUR = 18.3 GEØSTRØPHIC WIND IS .3M/SEC FRØM 150. DEG
WINDS AT LEVEL 1

(d)

Figure 5.26. Model-predicted vertical velocity fields in cm/s at 1 km for (a) light southeast, (b) strong southeast, (c) strong east, and (d) very light and variable synoptic wind simulations at 1830 EST. Contour interval is 3 cm/s.

= 18.3 GEØSTRØPHIC WIND IS 2.4M/SEC FRØM 150. DEG
ICAL VELØCITY 6 LEVEL

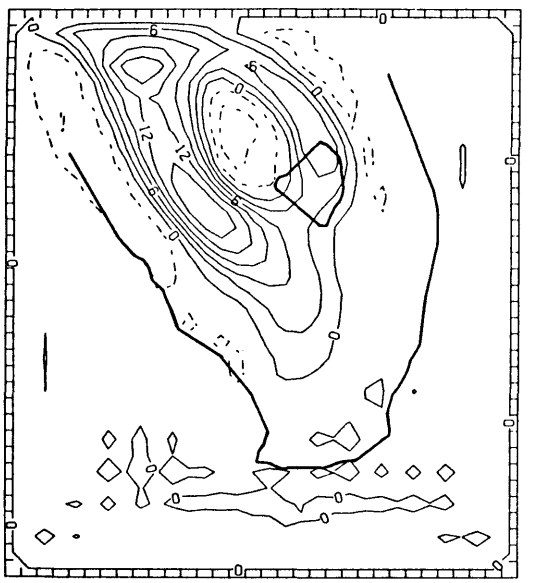

(a)

HØUR = 18.3 GEØSTRØPHIC WIND IS 5.7M/SEC FRØM 150. DEG
VERTICAL VELØCITY 6 LEVEL

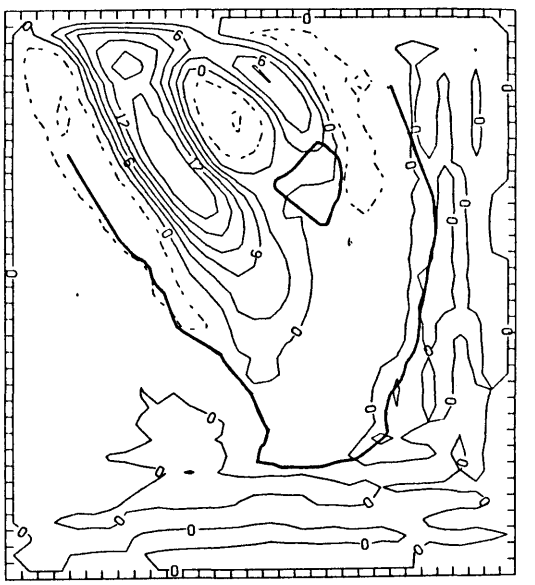

(b)

= 18.3 GEØSTRØPHIC WIND IS 5.8M/SEC FRØM 100. DEG
ICAL VELØCITY 6 LEVEL

(c)

HØUR = 18.3 GEØSTRØPHIC WIND IS .3M/SEC FRØM 150. DEG
VERTICAL VELØCITY 6 LEVEL

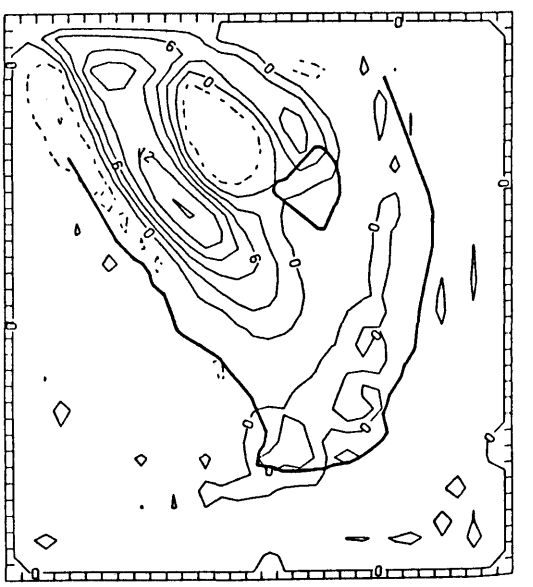

(d)

Figure 5.27. Model-predicted moisture availability fields ($\theta_{es} - \theta_e$) at 500 m for (a) light southeast, (b) strong southeast, (c) strong east, and (d) very light and variable synoptic wind simulations at 1830 EST. Contour interval is 4°K.

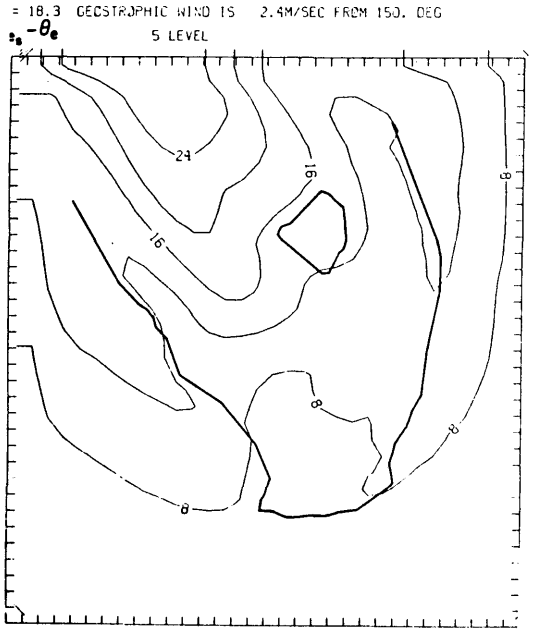
= 18.3 GEOSTROPHIC WIND IS 2.4M/SEC FROM 150. DEG
$\theta_{e_s} - \theta_e$
5 LEVEL
24
16
8
16
8
8
8

(a)

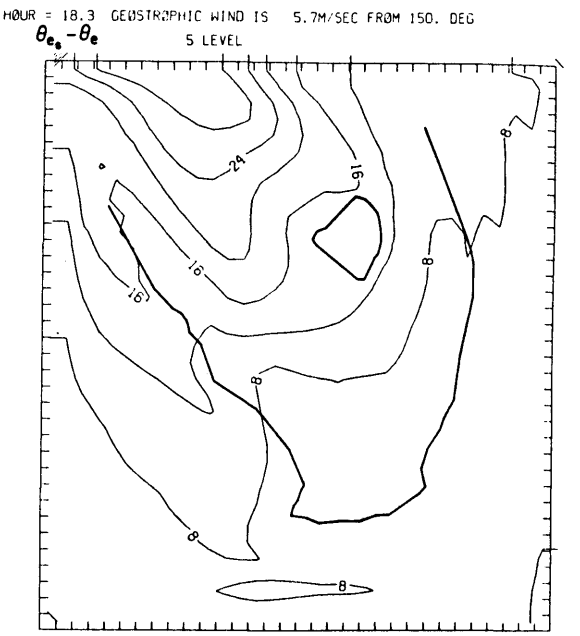
HOUR = 18.3 GEOSTROPHIC WIND IS 5.7M/SEC FROM 150. DEG
$\theta_{e_s} - \theta_e$
5 LEVEL
24
16
16
8
8
8
8

(b)

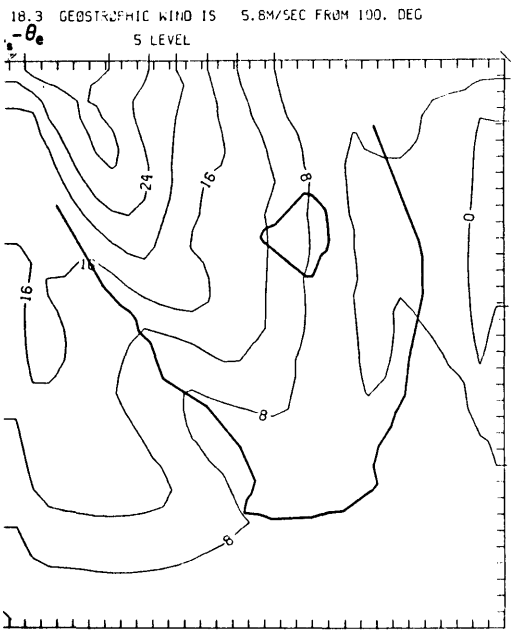
18.3 GEOSTROPHIC WIND IS 5.8M/SEC FROM 100. DEG
$\theta_{e_s} - \theta_e$
5 LEVEL
24
16
8
0
16
16
8
8

(c)

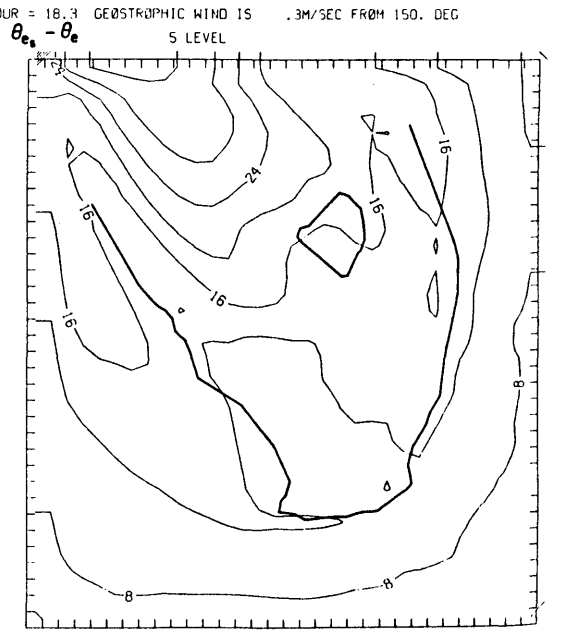
HOUR = 18.3 GEOSTROPHIC WIND IS .3M/SEC FROM 150. DEG
$\theta_{e_s} - \theta_e$
5 LEVEL
24
16
16
16
16
16
8
8
8

(d)

Figure 5.28. Model-predicted wind vectors at 25 m for the strong southwest synoptic wind simulation at (a) 1230 EST, (b) 1430 EST, (c) 1630 EST, and (d) 1830 EST. A vector of one grid length equals 8 m/s.

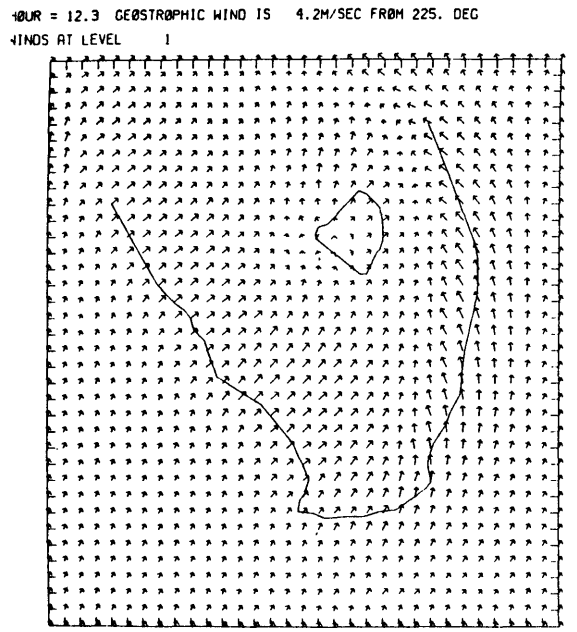
HØUR = 12.3 GEØSTRØPHIC WIND IS 4.2M/SEC FRØM 225. DEG
WINDS AT LEVEL 1

(a)

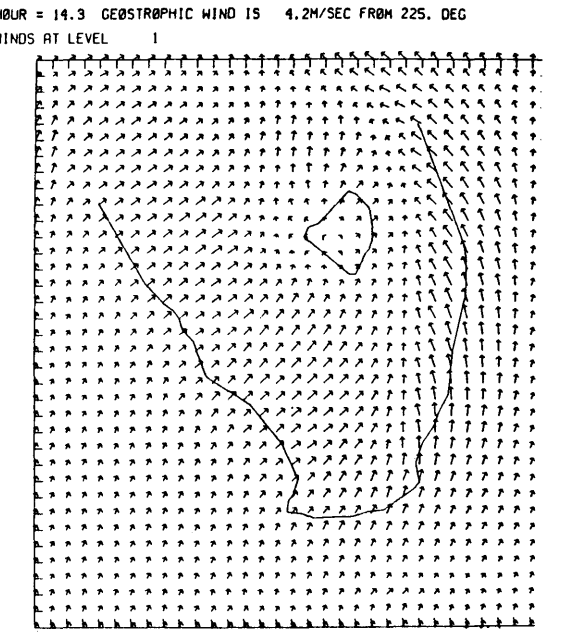
HØUR = 14.3 GEØSTRØPHIC WIND IS 4.2M/SEC FRØM 225. DEG
WINDS AT LEVEL 1

(b)

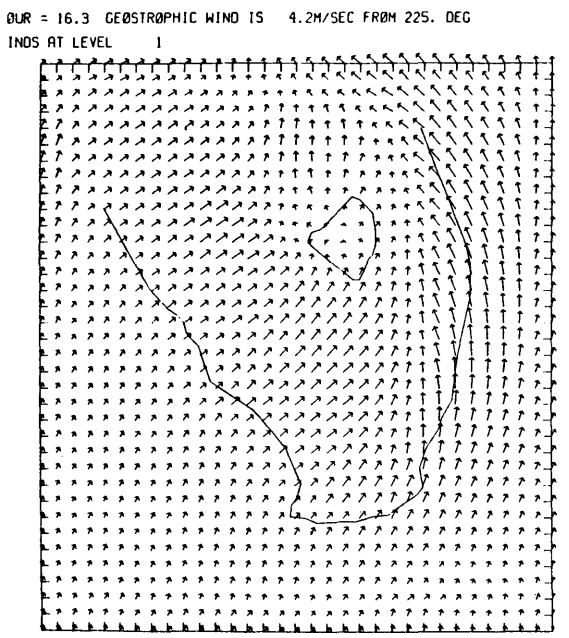
ØUR = 16.3 GEØSTRØPHIC WIND IS 4.2M/SEC FRØM 225. DEG
INDS AT LEVEL 1

(c)

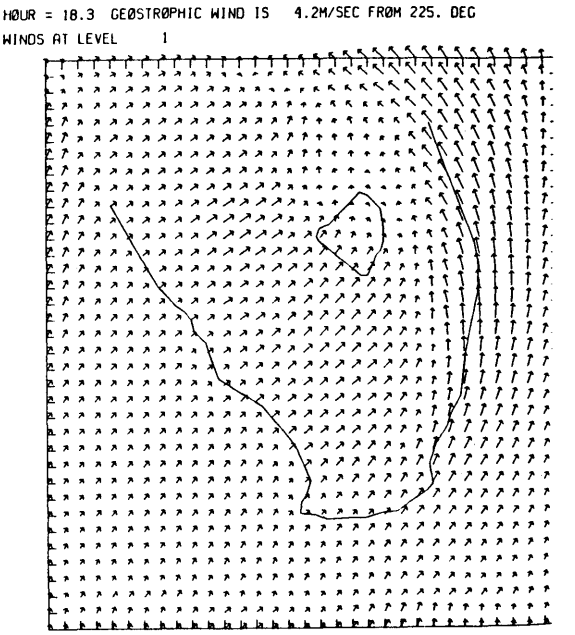
HØUR = 18.3 GEØSTRØPHIC WIND IS 4.2M/SEC FRØM 225. DEG
WINDS AT LEVEL 1

(d)

Figure 5.29. Model-predicted vertical velocity fields in cm/s at 1 km for the strong southwest synoptic wind simulation at (a) 1230 EST, (b) 1430 EST, (c) 1630 EST, and (d) 1830 EST. Contour interval is 3 cm/s.

= 12.3 GEØSTRØPHIC WIND IS 4.2M/SEC FRØM 225. DEG
CAL VELØCITY 6 LEVEL

(a)

HØUR = 14.3 GEØSTRØPHIC WIND IS 4.2M/SEC FRØM 225. DEG
VERTICAL VELØCITY 6 LEVEL

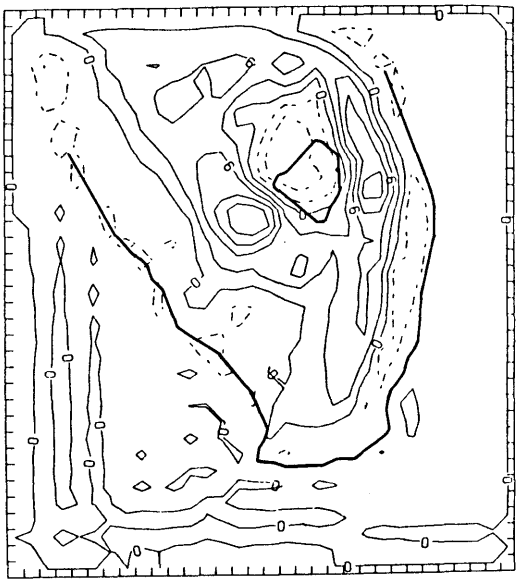

(b)

= 16.3 GEØSTRØPHIC WIND IS 4.2M/SEC FRØM 225. DEG
ICAL VELØCITY 6 LEVEL

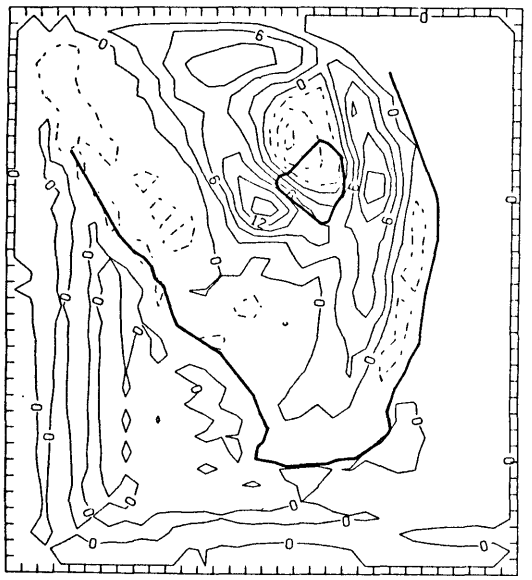

(c)

HØUR = 18.3 GEØSTRØPHIC WIND IS 4.2M/SEC FRØM 225. DEG
VERTICAL VELØCITY 6 LEVEL

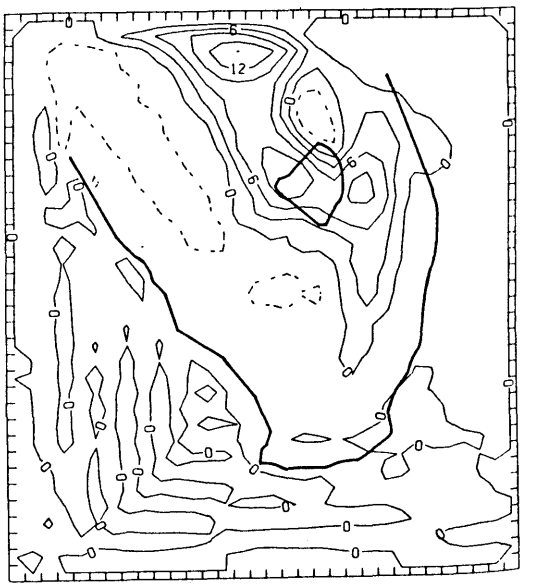

(d)

Figure 5.30. Model-predicted moisture availability fields ($\theta_{es}-\theta_{e}$) at 500 m for the strong southwest synoptic wind simulation at (a) 1230 EST, (b) 1430 EST, (c) 1630 EST, and (d) 1830 EST. Contour interval is 4°K.

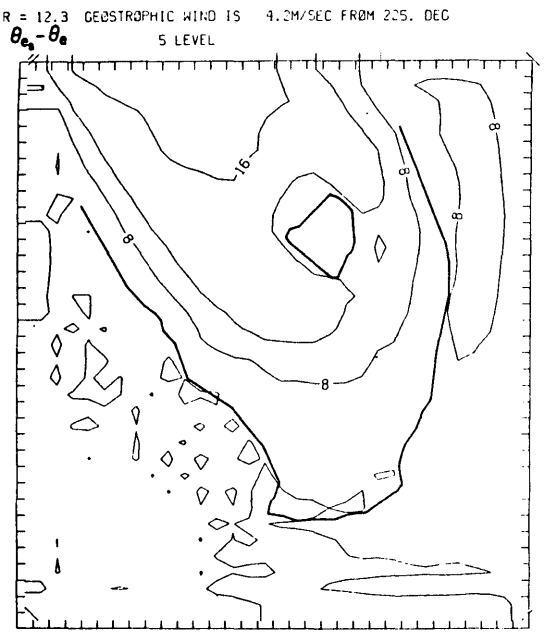
R = 12.3 GEØSTRØPHIC WIND IS 4.2M/SEC FRØM 225. DEG
$\theta_{e_s}-\theta_e$
5 LEVEL
16
8
8
8
8
8

(a)

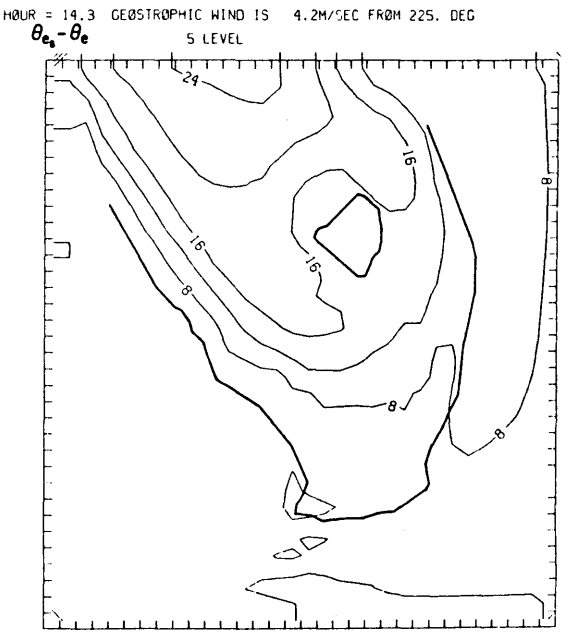
HØUR = 14.3 GEØSTRØPHIC WIND IS 4.2M/SEC FRØM 225. DEG
$\theta_{e_s}-\theta_e$
5 LEVEL
24
16
16
16
8
8
8

(b)

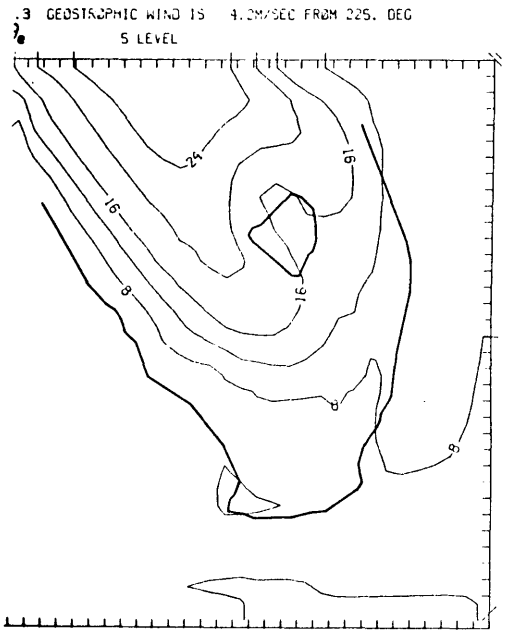
.3 GEØSTRØPHIC WIND IS 4.2M/SEC FRØM 225. DEG
5 LEVEL
24
16
16
16
8
8

(c)

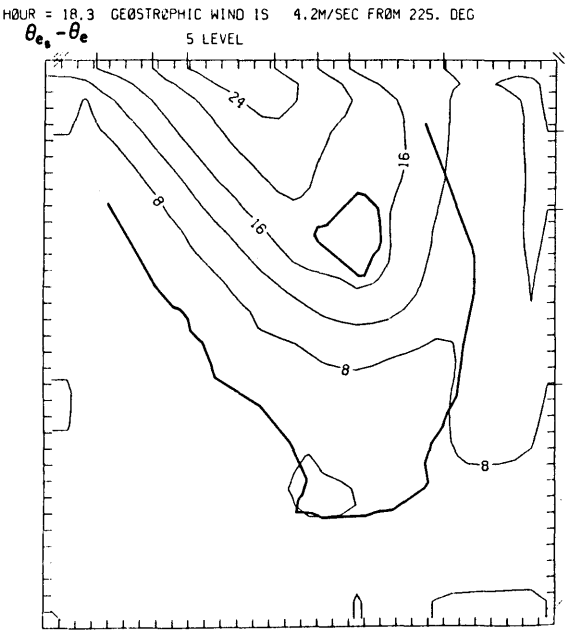
HØUR = 18.3 GEØSTRØPHIC WIND IS 4.2M/SEC FRØM 225. DEG
$\theta_{e_s}-\theta_e$
5 LEVEL
24
16
8
16
8
8

(d)

greatest vertical velocities just east of Lake Okeechobee where the east coast sea breeze meets the lake breeze. Subsidence over Lake Okeechobee is advected downwind and north of the lake for the cases presented in Figures 5.16 and 5.17. For strong easterly flow, the east coast sea breeze is further inland with the maximum convergence over the lake. The west coast sea breeze is strongest for the strong easterly simulation and covers a large area of the coast. With only light synoptic winds to oppose the onshore west coast sea breeze, the predicted convergence is weakest for the light and variable class.

The observed cloud patterns for light and strong southeast flow, as shown in Figure 5.3, do exhibit some cloudiness east of Lake Okeechobee at this time, as the model has predicted. However, along the west coast for both cases, deep convective cloudiness activity has developed to the south of the model predicted maximum vertical velocities. A plot of model-predicted moisture availability given at 1230 EST in Fig. 5.18 helps to explain the discrepancy. These figures indicate a moister low-level environment along the southern tip of the peninsula with drier air to the north. This may imply that the low-level moisture may not be sufficient to produce significant convective cloudiness along the northwest coast in the model predicted maximum convergence zone. To the south the moisture is greater due to the moister soils. As shown in Figure 5.13, wet soils such as marshes and peats dominate the soil type along the southern peninsula while dry sand is found in the northwest.

McCumber (1980) found from his model simulations that mesoscale convergence was greatest when the thermal contrast was large. Along the west coast this would explain why the maximum predicted

convergence is located to the north in the location of the drier soils. Drier soils would result in more heating at the surface than wetter soils, and therefore would be expected to create a greater thermal contrast between land and sea.

Also shown in Fig. 5.18 are moist tongues along both sea breezes due to convergence of moist marine air at the front.

For strong easterly flow at 1230 EST, there is a secondary model-predicted maxima in vertical velocities along the southwest coast. This result does agree with the satellite composite (Fig. 5.4a) at 1230 EST which shows a small area of preferred convection there. However, to the north no significant convective activity is shown by the satellite composite, apparently for the same reasons as explained for the southeasterly classes. The low-level moisture fields (Fig. 5.18c) are similar to the patterns predicted for the other flows. The model-predicted moisture fields at 25 m (not shown) remain well correlated with the surface soil types (Fig. 5.13), as the moistest air near the ground is found over the moistest soils. The moisture fields at 500 m are a reflection of the effects from the ground surface moisture.

For the light and variable class, the weak sea breeze convergence combined with the dry low-level environment for this class provides unfavorable conditions for convective cloudiness. Thus, as seen in the satellite image composite for this case, at this time no convection was found over the peninsula.

At 1400 EST, as shown in Figures 5.19 and 5.20 for both southeasterly cases, the maximum convergence region produced by the east coast sea breeze interacting with the divergent flow over Lake

Okeechobee has moved downwind and inland as compared with the 1200 EST results. This zone moves further north and west for the strong southeast simulation. The satellite composite for the strong southeast class at this time (Fig. 5.5b) does show a preferred region of deep convective cloudiness to the north of Lake Okeechobee near the model predicted convergence maximum. For the light southeast class, preferred convective cloudiness is located midway between Lake Okeechobee and the east coast. This zone is slightly east of the model predicted maximum convergence zone.

Along the west coast for both southeasterly synoptic flows, the maximum predicted convergence is found where the onshore sea breeze winds meet the divergent winds associated with the lake breeze to the west of Lake Okeechobee. Also, the west coast sea breeze convergence moves further inland along the convex curved portion of the coastline just to the west-southwest of the lake. Convex curvature, as noted by McPherson (1970) and Pielke (1974), enhances convergence along a coast. Along such a convex curved line of coast, a stronger sea breeze can develop which could advance inland earlier than on other parts of the coast. The lighter opposing winds for light southeast flow allow the west coast sea breeze to travel further inland than for strong southeast flow. Cloudiness patterns are seen to agree with the model predictions near the convex curved coastline for the southeasterly classes.

For light southeasterly flow, the larger convective cloud frequencies along the northern portions of the west coast sea breeze correlate well with the model-predicted vertical velocity fields. For strong southeast flow, preferred cloudiness is found just south of the

predicted maximum vertical velocities along the west coast. However, unlike the light southeast case, for strong southeast flow a minimum in convective cloudiness activity occurs further north where the dry sands are located. Convective clouds could be more favored for this region for light southeast flow since the large-scale environment was found to be somewhat moister as concluded in Chapter 4. Also, as depicted in Figs. 5.21a and 5.21b, $\theta_{es}-\theta_{e}$ over the sands on the northern part of the study area is, in general, 4 ° lower for the light southeasterly simulations than for the values over the same areas for the strong southeast class results. Therefore, low-level moisture is also greater on the mesoscale for the light southeast class. Greater convergence is needed for the strong southeasterly class in order to concentrate enough moisture along the sea breeze convergence zone to allow towering cumulus to develop.

The strong easterly model output fields at 1400 EST show the east coast sea breeze to move further inland than any other model run presented in Figure 5.19. For this case also, the maximum vertical velocities along the east coast sea breeze appear where the east coast sea breeze and the Lake Okeechobee divergence area meet. As of 1400 EST, the northern edge of the model-predicted maximum convergence is still cloud-free, as seen in Figure 5.6a. The southern edge of the maximum predicted convergence, however, is associated with an area of preferred convective cloudiness activity. Clouds near the southern maxima could have been aided by the added moisture available from Lake Okeechobee while clouds are suppressed near the northern convergence maximum because of a lack of moisture since it lies over a dry sand ground surface and is further away from the lake moisture source.

The area of convective cloudiness to the south also lies on the eastern edge of a line of high predicted vertical velocities extending perpendicular to the west coast sea breeze. The clouds also are located along a tongue of moisture extending from the southwest coast and inland to just north of Lake Okeechobee, as predicted by the model. This moist tongue is very visible for plots at 25 m (not shown). This line of convergence lies along a boundary between dry sands and wetter soils which produced a gradient in the low-level moisture field (Fig. 5.21c) and would also be responsible for the creation of a horizontal thermal gradient.

The west coast sea breeze for the strong easterly flow class is stronger than any other class at this time. Maximum convergence lies near a northern preferred region of convection as shown in Figure 5.6a. The southern convective cloud activity along the west coast is coincident with a secondary maximum in vertical velocity as predicted by the model at 1430 EST.

For the very light and variable wind class, vertical motions and convergence are predicted to be the weakest of all the classes and the low amount of convective cloud activity as seen in Figure 5.6b corresponds well with the model results.

The moisture availability fields at 500 m have been advected only slightly downwind for all simulations. The largest amounts of low-level moisture are still anchored near the moistest soils. The available moisture at 500 and 25 m (not shown) has decreased over the whole peninsula, especially over the northern part for all the simulations.

The model-predicted horizontal wind and vertical velocity fields at 1630 EST are shown in Figures 5.22 and 5.23. For both southeasterly

flows, the model-predicted convergence zone patterns are similar. The maximum vertical velocities along the west coast are 18 cm/s for light synoptic southeasterly flow but slightly less at 15 cm/s for strong southeasterly flow. When comparing these fields to the satellite composites shown in Figure 5.7, the northern region of preferred cloud activity along the west coast for light southeasterly synoptic flow closely matches the model-predicted maximum vertical velocities associated with the west coast sea breeze. The southern preferred area in deep convective cloud activity along the west coast sea breeze does lie along the model-predicted sea breeze band but the predicted vertical velocities are small in this area, only reaching 5 cm/s.

For strong southeasterly flow, as was noted in Section 5.1, much of the peninsula is covered with cloudiness by 1600 EST. Most of the convective activity is concentrated further north. The largest convergence within the model-predicted west coast sea breeze for this case (Fig. 5.23b) is located along a region of 60 percent deep convective cloud frequencies (Fig. 5.7b).

Along the east coast at 1630 EST, the model predicts a strong convergence zone north and east of Lake Okeechobee for both southeasterly cases. However, for light southeasterly flow, clouds which appeared in this area at 1400 EST have dissipated or moved further west with relation to the simulated east coast sea breeze convergence zone. Convective scale processes may be acting to produce the discrepancies. The deep cumulus clouds, for instance, could be simply advected downwind from the convergence zone, still retaining their identity.

For strong southeasterly flow at 1600 EST, 60 percent cloud frequencies are well correlated with the model-predicted maximum convergence near the lake. However, a region of 60 percent cloud frequencies also lies to the southeast of Lake Okeechobee parallel to the east coast. The model predicts no convergent flow in this area. The disagreement might be explained by convective scale downdrafts from the storms found south of this region at 1400 and 1600 EST, which created a convergent zone to the north.

For the strong easterly class, the model-predicted west coast sea breeze line at 1630 EST extends along most of the west coast at this time and remains closer to the coast than for any of the other simulations. Vertical velocities have increased to a maximum of 21 cm/s. The two areas of preferred convective cloud activity shown in Figure 5.8a do lie along this line. The northern preferred cumulus convection area corresponds very well with the maximum predicted vertical velocities. The southern preferred area lies along a region of weaker predicted vertical motion. However, as noted previously, and as shown in Fig. 5.24c, the atmosphere is moister in the low levels in the south, and therefore more abundant amounts of moisture are available for cloud formation.

As noted previously from the strong easterly composite image (Fig. 5.8a), a region of 50 percent deep convective cloud frequencies extends from the preferred region of convection along the west coast to the west side of Lake Okeechobee. This line is near a region of upward vertical motions indicated by the model output fields at 1600 EST. Convergence in this area may be enhanced by the convective downdrafts from the cloudiness indicated along the west coast sea

breeze. The area of cloudiness also lies along the western boundary of the model-predicted moist tongue which is shown in Fig. 5.24c at this time.

The model-predicted east coast sea breeze for the strong easterly simulations has advanced further inland than for any of the other model runs. From the satellite composites for this class, a region of 30 percent cloud frequencies is found to the west of this simulated convergence zone. It appears that either the model prediction is slow in advancing the east coast sea breeze or cumulus clouds, once initiated, are advected by the low-level wind at a speed greater than the inland propagation velocity of the sea breeze convergence zone.

A secondary vertical velocity maximum is located to the north of the primary west coast sea breeze maximum at 1630 EST for the strong easterly simulation. However, no deep convective clouds have developed over that region at this time, perhaps as a result of the drier low-level atmosphere in that location.

The light and variable simulation indicates a weaker west coast sea breeze than for any of the other model simulations at 1630 EST. The maximum convergence zones are in similar positions as in the southeasterly model results. Convective cloudiness is less prevalent than any other class as shown in the satellite image composite (Fig. 5.8b). Deep convective clouds, however, were observed to have advanced inland less than predicted. The winds used to initialize the model may be overestimating the true effect of the synoptic flow. For this class, observed winds often were light and varied in direction throughout the day while the model large-scale winds are constant in

direction from the southeast throughout the day so that advection by the synoptic wind is possible.

The moisture fields at 500 m have been displaced slightly since 1430 EST for all simulations (Fig. 5.24). The moisture deficit for several of the wind categories is slightly larger over the dry sandy soils in the northern part of the study area as $\theta_{es}-\theta_{e}$ has increased since 1430 EST. Also, the moist tongue associated with the sea breezes is still present. For all synoptic flow results shown in Fig. 5.24, a dry tongue is seen over the ocean off the west coast. This is associated with the return flow downward vertical motion branch of the west coast sea breeze.

The 1830 EST model output fields are shown in Figures 5.25 through 5.27. For the southeasterly class simulations, stronger convergence and vertical velocities are found along the northern portion of the west coast sea breeze while the vertical velocity maximum to the south has decreased since 1630 EST. The strong convergence maximum to the north is produced by the west coast sea breeze interacting with the divergent flow from Lake Okeechobee which has advected north with the synoptic flow. The east coast sea breeze has moved to the north of Lake Okeechobee. Its vertical velocities are enhanced by the divergent flow from the lake meeting the onshore east coast sea breeze.

As shown in Fig. 5.9a and b, maximum cloud frequencies have diminished along the southern half of the peninsula for the southeasterly classes at 1800 EST. At this time, cloudiness is concentrated near the model-predicted east coast sea breeze to the north of Lake Okeechobee. This area was cloud free at 1600 EST.

At 1830 EST for the strong easterly model simulations, the southwest coast maximum in vertical velocity has also decreased in size slightly while the northern maxima has increased from 15 to 21 cm/s in two hours. The east coast sea breeze is further west than for any of the other classes.

The maximum cloud frequencies for the strong easterly synoptic flow class shown in Figure 5.10a are associated with the stronger model-predicted vertical velocity maximum in the north. To the south, deep convective activity has diminished at 1800 EST as has the peninsula scale convergence predicted by the model in this region. However, as was mentioned earlier, another possible cause for storms to die out is a result of the cirrus created earlier from the deep convective clouds which covered the peninsula. This cirrus would reduce the incoming solar radiation and resultant surface thermal contrast. Along the weaker model-predicted east coast sea breeze, little convection is noted.

For the light and variable class, some convection is noted along an area of maximum predicted convergence where the lake divergent flow and the east coast sea breeze flow meet. The convective cloud region which developed earlier due east of Lake Okeechobee is dissipating at 1800 EST in an area of low model-predicted convergence.

At 1830 EST, little difference is noted in the model-predicted moisture fields (Fig. 5.27) from 1630 EST. $\theta_{es}-\theta_{e}$ at 500 m is in general slightly higher over the north-central portion of the peninsula. The moist tongue associated with the west coast sea breeze has also extended further north for all cases.

The strong southwest class model-predicted wind and vertical velocity fields are depicted in Figures 5.28 and 5.29, while the moisture fields at 500 m are shown in Figure 5.30. Enhanced convergent regions at 1200 EST are found in the east coast sea breeze and just west of Lake Okeechobee where the lake breeze and west coast sea breeze meet. As was the case for the easterly flow class simulations, convergence is strongest on the downwind coast (in this case, the east coast) through most of the afternoon.

The satellite composite for 1200 EST shown in Figure 5.11b reveals deep convective clouds to form first along the west coast near the convex curved coastline. This is near where the model maximum predicted convergence is at this time. These clouds also lie along the boundary between drier and moister air as shown in Fig. 5.30a. Along the east coast, as shown in Fig. 5.11b, only shallow clouds, which are probably convective, are seen paralleling the model-predicted east coast sea breeze.

By 1600 EST, deep convective clouds are found along the model-predicted maximum convergence along the east coast sea breeze, southeast of Lake Okeechobee. The deep convective clouds are located south of the model-predicted maximum vertical velocities associated with the east coast sea breeze. The outflows from the storms which developed earlier to the north may have added convergence which allowed convection to grow in the moist environment along the southern tip of the peninsula.

A small area of deep convective cloudiness is also found well northwest of Lake Okeechobee at 1600 EST near an area of high vertical velocities predicted by the model. The convergence here is due to the

merger of the lake divergence flow with the onshore flows from both the east and west coast sea breezes.

At 1830 EST, the convergence zone well north of Lake Okeechobee has continued to intensify. Near that area a large band of deep convective clouds were found (Fig. 5.12b). The model also correctly predicts two local maxima along the southern parts of the east sea breeze convergence zone which corresponds to two maxima in convective cloud frequencies.

## 5.3 Discussion

With the results of the satellite image composites, spatial and temporal characteristics of deep convective cloud patterns and their variation with synoptic flow have been described. The results from the numerical model have helped offer explanations for the observed patterns.

To summarize for each synoptic flow class: first, for light southeasterly flow, deep convective clouds developed along the east coast sea breeze and along the southern tip of Florida early in the day. By mid-afternoon convection formed along the west coast sea breeze convergence zone and moved inland. Convection was highly organized along both sea breeze convergence zones with the most preferred regions of convective activity located near the convex curved coastline along the west coast and east of Lake Okeechobee where the east coast sea breeze convergence was enhanced by the lake breeze flow. By late afternoon, convection in the south had advanced further west in the direction of the low-level flow. The east coast sea breeze convection to the east of the lake had dissipated. By early evening, clouds in the southern peninsula had dissipated with new

development forming just north of Lake Okeechobee where the east coast sea breeze flow interacted with the divergent flow which formed over the lake but has been advected to the northwest.

For strong southeast flow, convection moved further inland from the east coast than for light southeasterly flow. Convection developed later on the west coast with preferred regions found along the southwest coastline. Another preferred region in the afternoon was found north of Lake Okeechobee along the intersection of the east coast sea breeze and lake breeze. By evening this region was translated further north by the prevailing flow. The southern convective area dissipated by evening. This class illustrated less convective organization with more convection located over many portions of the peninsula than was the case for the light southeasterly composite.

For strong easterly flow, convective activity started later than for the southeasterly classes. By early afternoon, well pronounced convection was concentrated along the southwest coastline with no activity along the southeast coast. The model also predicted the strongest peninsula scale forcing by this time along the west coast. The most preferred regions of convective activity remained anchored along the west coast associated with sea breeze convergence and did not move inland. By late afternoon convective activity was also found along the east coast sea breeze convergence zone which had moved rapidly to west of Lake Okeechobee. By early evening preferred areas of convection were advected offshore and were found further north than earlier. The early evening convection was located along an enhanced convergence area where the west and east coast sea breeze and the lake breeze interacted, as predicted by the model.

Convective activity for light and variable days was very suppressed throughout the day. The model-predicted vertical velocities were less than the other classes as the weak synoptic flow did not substantially enhance the sea breeze convergence along the downwind coastline by opposing the onshore sea breeze flow. Some convection had formed in the east coast sea breeze convergence zone just east of Lake Okeechobee and along the southwest coast. By early evening, the southern convective areas had dissipated while some spotty deep convection had developed to the north, where the east coast sea breeze had advanced inland.

For the strong southwesterly class, only one satellite case was available. Early in the afternoon the strongest convection had formed along the convex curved part of the southwest coast with shallow convection along the east coast sea breeze convergence region. The west coast convective clouds had moved inland with the sea breeze convergence by late afternoon. Widespread deep convection had also developed along the southern extent of the peninsula. In the early evening, cirrus created by the southern convective clouds appeared to have developed over the convection and reduced the convective activity there. Well north and inland where the east and west coast sea breezes met, convection had developed by the end of the day.

The results of the satellite climatology do compare well with previous radar-derived climatologies for South Florida. Frank et al. (1967) classified the synoptic flow by only two wind directions: easterly or westerly winds greater than 6 kts. Their radar echo frequency charts for the easterly wind regime at 1300 indicated maximum frequencies mainly along the southwest coast with minimal activity

to the north. This agreed well with the 1200 and 1400 EST southeasterly and easterly satellite image composites. Frank et al. also found a secondary maximum in radar frequency just east of Lake Okeechobee at 1300 EST. This was shown in the early afternoon easterly wind deep convection satellite image composites.

Blanchard and Lopez (1984) also found for days which typically were under light southeast synoptic flow that the most intense radar echoes were most often located along the southwest coast along the west coast sea breeze early in the afternoon. The 1400 to 1700 radar echo composite revealed more widespread convection over the entire southern peninsula except near the east coast. The most intense echoes were found along the west coast sea breeze near the bulge in the coastline. This pattern was also found at 1600 EST in the east wind regime in radar frequency composites of Frank et al. (1967) and in the 1600 EST light southeasterly wind satellite image composites.

Blanchard and Lopez (1984) also presented a radar echo composite in which the winds were primarily strong and out of the east. The patterns noted closely followed what was observed in the strong easterly flow satellite image composites with convection developing later in the day and then remaining on the west coast and finally moving offshore and dissipating.

The results of the numerical model and the satellite cloud composites have shown the importance of the low-level synoptic flow in developing sea breeze convergence patterns, and, therefore, in controlling the onset and subsequent position of deep convective clouds. These model calculations have illustrated the variation of

the peninsula scale flow as a result of its interaction with the most frequent summertime synoptic flows found over South Florida.

The importance of the synoptic flow in controlling the spatial and temporal variations in the cumulus cloud and sea breeze forcing over South Florida has been previously noted from the radar climatologies of Frank et al. (1967), Blanchard and Lopez (1984), and the numerical modelling studies of Pielke (1974). For the study presented here, deep convective clouds were mainly found along the model-predicted sea and lake breeze convergence zones. Enhanced regions of convective activity and model-predicted vertical velocities early in the day were located near the convex coastline along the southwest coast. The effect of convex coastline curvature in enhancing convergence has been noted by McPhearson (1970), Smith (1970), and Pielke (1974). Other areas of enhanced convective activity and strong model-predicted convergence were found where the coastal sea breeze converged with the lake breeze flow which was advected downwind off Lake Okeechobee during the day.

One area, however, where the model-predicted wind convergence had consistently disagreed with the observed convective cloud activity during the early afternoon was over the southern tip of the peninsula where a strong preference for convective clouds was found. As discussed by McCumber (1980), the model predicts less convergence over South Florida in the west and south coast sea breezes where marshes and wet soils are located. In these regions the ground will remain cooler and, therefore, the thermal contrast between land and sea will be less resulting in a smaller horizontal pressure gradient. The model predicted stronger convergence to the north, however, where dry,

warmer sands are located, with a resultant larger heat contrast between sea and land.

Despite the fact that the predicted peninsula scale convergence is smaller in the southern tip, the lower tropospheric environment for convective clouds would be favored along the southern coast if the environment had higher amounts of low-level moisture due to the wetter soils. The available buoyant energy for cumulus convection would, therefore, be greater. As shown from the plots of $\theta_{es}-\theta_{e}$, a significantly moister environment was predicted by the model in the south where the maximum of convective activity was found. As shown in Chapter 4 from the statistical results of this study and by other works, low-level moisture was the only statistically significant positively correlated large-scale thermodynamic variable which is related to the 1400 EST averaged percentage of deep convective clouds. Over the drier soils to the north, despite the warmer low-level temperatures which created a greater thermal contrast between sea and land, the low-level moisture supply was insufficient to fuel deep convection in the early afternoon.

To aid cumulus development over the southern tip of the peninsula, in addition to convergence from the peninsula scale forcing, some convergence may be due to convective scale processes. Cooper et al. (1982) found that convergence due to convective scale and peninsula scale processes both reached their maximum near local noon. Throughout the rest of the afternoon, peninsula scale convergence decreases rapidly while convergence on the convective scale continues. The outflows from the deep cumulus in the south would be

better able to initiate subsequent cumulus convection because the low-level atmosphere is moister.

The degree of organization of convection along the sea and lake breezes decreased from 1400 EST to 1600 EST as seen from the satellite image composites. Some convective clouds began to move away from the sea breeze convergence regions by 1600 EST. This result is supportive of the results of Cooper et al. in which there was a decrease in peninsula scale forcing but an increase in development forced by the convective scale downdrafts. The decrease in the first forcing may be accelerated by the cloud shading effect (e.g. Gannon, 1978; Segal et al., 1984).

Despite the increase in convective scale forcing, however, most of the cumulus convection still remained near their initiation regions along the sea breeze convergent zone. This tendency for cumulus clouds to remain anchored near the sea breeze convergence zones appears to be a result of the preconditioning and enrichment of the atmosphere by the convergence of moisture and heat by the sea breeze. In addition, mergers of cumulus clouds, with the resultant larger rainfalls and longer lifetimes (Simpson et al., 1980), would be favored by the low-level convergence in the sea breeze convergence zones.

The variations of the ground surface characteristics were also found to be responsible for the creation of substantial horizontal temperature and moisture gradients. These gradients resulted in additional wind convergence zones in the model results which appear to be associated with enhanced cumulus cloudiness as seen from the satellite composites in those areas. In addition, the character of

the surface was responsible for suppressing cloud growth due to lack of moisture in some areas where the soils are dry as well as to enhance preferred areas of cumulus convection by adding more moisture in the wetter soil regions.

# CHAPTER 6

## SUMMARY AND CONCLUSIONS

This study has described the deep convective cloud patterns over South Florida on synoptically undisturbed days. This was accomplished by processing visible and IR satellite images so that only cumulonimbus clouds remained. The reprocessed images were stratified according to the surface synoptic geostrophic flow direction and speed over the peninsula in the morning. The use of a subjective categorization to classify the synoptic flow condition was found to agree well with single station wind results, as shown in Section 4.1.

Composites for the four most common flow types in the collected data were presented. These were light southeast, strong southeast, strong east, and very light and variable synoptic geostrophic flow. Also included was a composite in which the images for all available undisturbed days were included as well as the images from one day in which surface geostrophic winds were strong southwesterly. Image composites were created for every other hour for six times of the day.

To help determine some of the controls on the amount of convective activity over the peninsula, the amount of deep convective clouds was calculated for each synoptic class and compared to the synoptic environments in which the convection formed. As found in previous studies in which different data analysis techniques were used (Frank and Smith, 1968; Pielke et al., 1977; Burpee and Lahiff, 1984), the most important large-scale variable in controlling the amount of

deep convection was the availability of moisture in the lower and middle troposphere. This was shown from a regressional analysis and also from noting the suppressed amount of deep convection over the Florida peninsula associated with the very dry lower troposphere for the very light and variable synoptic class. The large-scale subsidence from the Atlantic high pressure ridge which was stationed near Florida for the light and variable flow was believed responsible for the drying and warming of the lower troposphere.

The low-level winds were found to only weakly control the percent of deep convection over the peninsula on undisturbed days. This result agreed with the findings of Blanchard and Lopez (1984).

Results of a regression analysis using synoptically undisturbed days demonstrated that the amount of deep convection present over the surrounding waters at 0800 EST was strongly positively correlated with the afternoon percentage of deep convective clouds over land. The percent of deep convection at 1000 EST over the peninsula was also strongly correlated with the afternoon convective activity over South Florida. Both the 0800 EST deep convective cloud activity over water and the 1000 EST deep convection over land were, therefore, effective indicators of how favorable the large-scale environment in the afternoon was for deep convection--a result which would be expected if the synoptic environment was changing only slowly with time.

While the surface geostrophic wind was not a major influence on controlling the amount of convection over the peninsula (except for light and variable flow), it strongly forced the locations of the preferred areas of convection as shown from the comparisons between the different satellite image composites. To help explain the

important processes controlling the areas of preferential development of deep convection as a function of the surface geostrophic flow, a dry three-dimensional mesoscale model was utilized to simulate sea breezes along the coast, the lake breeze near Lake Okeechobee, and local circulations due to sub-peninsula variations in the ground surface characteristics. From the model results, as found in earlier studies (e.g., Pielke, 1974; Pielke and Mahrer, 1978), different geostrophic flow resulted in variations in the pattern of the sea and lake breeze convergence zones. By comparison to the satellite composites, these convergence zones were found to be well correlated with areas of deep convection. The convex curvature of the coastline, and resultant enhanced sea breeze convergence was shown to be particularly important in creating preferred areas of convection. Well-defined preferred areas of convection were also found where the Lake Okeechobee breeze met the inland penetrating sea breeze for all the synoptic flow categories. Past studies have examined the relation between sea breeze convergence and subsequent convective activity on a case-by-case basis. This report has helped show the importance of sea breeze convergence and the synoptic flow in controlling the convective patterns on a climatological basis over South Florida.

Model-predicted wind convergence zones, however, consistently failed to agree with the observed preferred convective cloud activity over the southern tip of the peninsula. In addition, along the northwest coast during the early afternoon for most simulations, strong sea breeze induced upward vertical motions were predicted, although little convective activity was present there at the corresponding times. These discrepancies between model-predicted convergence and the

satellite image composites appear to be explained by the dramatic differences in the predicted low-level moisture fields between the northwest coast and the southern peninsula. The model predicted a very dry lower troposphere along the northwest coast of South Florida as compared to areas further south. The variations in moisture were attributed to the differences in soil type since the southern part of the peninsula is underlain by moist soils such as marshes and peats, while the northwest soils are mainly dry sands. In the early afternoon, then, despite the stronger mesoscale wind convergence in the north due to a greater thermal contrast between sea and land, the low-level environment was still too dry to support moist convection. In the south, however, despite the weaker sea breeze convergence, the environment was more supportive of cumulus cloud formation. Therefore, while convection was found mainly along the sea breeze front, the most preferred activity was located where the mesoscale supply of moisture was higher. This suggested that, along with the synoptic scale moisture supply, which was found to control the average percentage of deep cumulus over the whole peninsula, the availability of moisture on the mesoscale was critical in the patterning of this convective cloud activity.

Convective scale processes were hypothesized to play a role in convective cloud formation, especially later in the day. As shown by the satellite composites, the organization of convection in the mesoscale convergence zones decreased from 1400 EST to 1600 EST. This result agreed with findings by Cooper et al. (1982) that sea breeze scale convergence decreased while convective scale processes became more dominant toward the late afternoon. Outflow from convective

clouds which intersected outflow from other convection or with the sea breeze was shown to be an important mechanism in the development of subsequent strong thunderstorms over South Florida by Simpson et al. (1980) and Cunning et al. (1982). It was postulated that these processes were at work in the data presented for this study since, in some cases, convective clouds were preferred in areas where the model-predicted convergence and moisture fields did not indicate development.

Finally, the complementary use of a mesoscale climatology from satellite data and a mesoscale numerical model as a tool for short-range forecasting (6-18 hours) of terrain-induced mesoscale systems has been proposed previously (Krietzberg, 1976; Pielke, 1976, 1982). The successful utilization of these tools was argued for terrain-mesoscale induced systems since the surface forcing is very similar from day to day. The same local weather patterns will occur frequently varying only as a function of synoptic conditions, which, it is suggested, can be classified into a few types.

It was suggested that a mesoscale model could be integrated only a few times for each of the synoptic categories found to be most prevalent over an area. This report has presented the results from a small sample of satellite image-composites and mesoscale model simulations for typical synoptic flow conditions over South Florida in order to examine the validity of this approach. It was demonstrated that cumulus convection over South Florida is closely associated with convergence due to thermally-forced mesoscale systems. Thus the practicality of the proposals by Krietzberg and Pielke appear to have been established. This report has shown that recurrent convective

cloud patterns do occur over South Florida, with the mesoscale model moisture and convergent wind fields agreeing to a large extent with the average deep cumulus cloud positions as determined from the satellite climatology. These interpretations of the model results should be useful to forecasters when analyzing satellite data in real time.

Future research suggestions include adding to the amount of data which made up the satellite composites for this report. Also, the incorporation of convective scale processes into the model physics should better explain some of the convective patterns observed. Without these additions, however, much insight has still been gained concerning the role of physical forcings of various scales on convective cloud patterns in South Florida.

## REFERENCES


Atwater, M. A., and Brown, P., Jr. (1974). Numerical calculations of the latitudinal variation of solar radiation for an atmosphere of varying opacity. J. Appl. Meteorol, 13, 289-297.

Betts, A. K. (1974). Thermodynamic classification of tropical convective soundings. Mon. Weather Rev, 102, 760-764.

Blanchard, D. O., and López, R. E. (1984). Variability of the convective field pattern in south Florida and its relationship to the synoptic flow. NOAA Tech. Memo. ERL ESG-4. U.S. Dept. of Commerce, Boulder, Colorado 80303. 77 pp.

Burpee, R. W. (1979). Peninsula-scale convergence in the south Florida sea breeze. Mon. Weather Rev., 107, 852-860.

Burpee, R. W., and Lahiff, L. N. (1984). Area averaged rainfall variations on sea-breeze days in south Florida. Mon. Weather Rev, 112, 520-534.

Businger, J. A. (1973). Turbulent transfer in the atmosphere surface layer. "Workshop in Micrometeorology," Chapter 2. Am. Meteorol. Soc., Boston, Massachusetts.

Byers, H. R. and Rodebush, H. R. (1948). Causes of thunderstorms of the Florida peninsula. J. Meteor., 5, 275-280.

Clapp, R., and Hornberger, G. (1978). Empirical equations for some soil hydraulic properties. Water Resour. Res. 14, 601-604.

Cooper, H. J.; Garstang, M.; and Simpson, J. (1982). The diurnal interaction between convection and peninsular-scale forcing over south Florida. Mon. Weather Rev., 110, 486-503.

Cotton, W. R.; Gannon, P. T.; and Pielke, R. A. (1976). Numerical experiments on the influence of the mesoscale circulations on the cumulus scale. Journ. Atmos. Sci., 33, 225-261.

Cunning, J. B.; Holle, R. L.; Gannon, P. T., Sr.; and Watson, A. I. (1982). Convective evolution and merger in the FACE experimental area: Mesoscale convection and boundary layer interactions. J. Appl. Meteorol., 21, 953-977.

Day, S. (1953). Horizontal convergence and the occurrence of summer shower precipitation at Miami, Florida. Mon. Weather Rev., 81, 155-161.

Deardorff, J. W. (1974). Three-dimensional numerical study of the height and mean structure of a heated planetary boundary layer. Bound. Layer Meteorol., 7, 81-106.

Deardorff, J. W. (1978). Efficient prediction of ground surface temperature and moisture, with inclusion of a layer of vegetation. J. Geophys. Res., 83 (C4), 1889-1903.

Frank, N. L. and Smith, D. L. (1968). On the correlation of radar echoes over Florida with various meteorological parameters. J. Appl. Meteor., 7, 712-714.

Frank, N. L.; Moore, P. L.; and Fisher, G. E. (1967). Summer shower distribution over the Florida peninsula as deduced from digitized radar data. J. Appl. Meteor., 6, 309-316.

Gannon, P. T., Sr. (1978). Influence of earth surface and cloud properties on the south Florida sea breeze. NOAA Tech. Rep. ERL 402 - NHEML 2. U.S. Dept. of Commerce, Boulder, Colorado 80303. 91 p.

Gentry, R. C. and Moore, P. L. (1954). Relation of local and general wind interaction near the sea coast to time and location of air-mass showers. J. Meteor., 11, 507-511.

Kessler, R. C.; Eppel, D.; Pielke, R. A.; and McQueen, J. (1985). A numerical study of the effects of a large sandbar upon sea breeze development. Arch. Met. Geoph. Biocl., Series A, 34, 3-26.

Klitch, M. A.; Weaver, J. F.; Kelly, F. P.; and Vonderhaar, T. H. (1985). Convective cloud climatologies constructed from satellite imagery. Mon. Wea. Rev., 113, 326-337.

Kreitzberg, C. W. (1976). Interactive applications of satellite observations and mesoscale numerical models. Bull. Am. Meteorol Soc., 57, 679-685.

López, R. E.; Gannon, P. T., Sr.; Blanchard, D. O; and Blach, C. C. (1984). Synoptic and regional circulation parameters associated with the degree of convective shower activity in south Florida. Mon. Weather Rev., 112, 686-703.

Mahrer, Y. and Pielke, R. A. (1975). The numerical study of the air flow over mountains using the University of Virginia mesoscale mode. Journ. Atmos. Sci., 32, 2144-2155.

Mahrer, Y. and Pielke, R. A. (1977). A numerical study of the airflow over irregular terrain. Beitrage zur Physik der Atmosphare, 50, 98-113.

Mahrer, Y. and Pielke, R. A. (1978). A test of an upstream spline interpolation technique for the advective terms in a numerical mesoscale model. Mon. Weather Rev., 106, 818-830.

Maier, L. M.; Krider, E. P.; and Maier, M. W. (1984). Average diurnal variation of summer lightning over the Florida peninsula. Mon. Weather Rev., 112, 1134-1140.

McCumber, M. C. (1980). A numerical simulation of the influence of heat and moisture fluxes upon mesoscale circulations. Ph.D. dissertation, Dept. of Environmental Sciences, The University of Virginia, Charlottesville. 255 p.

McCumber, M. C. and Pielke, R. A. (1981). Simulation of the effects of surface fluxes of heat and moisture in a mesoscale numerical model. Part I: Soil layer. Journ. of Geophys. Res., 86, 9929-9938.

McNider, R. T. and Pielke, R. A. (1981). Diurnal boundary-layer development over sloping terrain. J. Atmos. Sci., 38, 2198-2212.

McPherson, R. D. (1970). A numerical study of the effect of a coastal irregularity on the sea breeze. J. Appl. Meteor., 9, 767-777.

O'Brien, J. J. (1970). A note on the vertical structure of the eddy exchange coefficient in the planetary boundary layer. J. Atmos. Sci, 27, 1213-1215.

Paegle, J.; Zdunkowski, W. G.; and Welch, R. M. (1976). Implicit differencing of predictive equations of the boundary layer. Mon. Weather Rev., 104, 1321-1324.

Pielke, R. A. (1973). An observational study of cumulus convective patterns in relation to the sea breeze over south Florida. NOAA Tech. Memo. ERL OD16, U.S. Dept. of Commerce, Boulder, Colorado 80303. 81 p.

Pielke, R. A. (1974). A three-dimensional numerical model of the sea breezes over south Florida. Mon. Weather Rev., 102, 115-139.

Pielke, R. A. (1976). Use of model results and satellite imagery to improve local weather forecasts over south Florida during the summer. Preprint Volume, Sixth AMS Conference on Weather Forecasting and Analysis, May 10-13, Albany, New York, pp. 28-33.

Pielke, R. A. (1982). The role of mesoscale numerical models in very-short-range forecasting. In Nowcasting (Ed. K. Browning), Academic Press, New York, N.Y., pp. 207-221.

Pielke, R. A. (1984). Mesoscale meteorological modeling, Academic Press, New York, N.Y., 612 p.

Pielke, R. A. and Mahrer, R. (1978). Verification analysis of the University of Virginia three-dimensional mesoscale model prediction over south Florida for 1 July 1973. Mon. Weather Rev., 106, 1568-1589.

Pielke, R. A.; Biondini, R.; and Mullen, G. (1977). Rainfall in the EML (Experimental Meteorology Laboratory) Target Area as a function of synoptic parameters. Conference Preprint Volume of Fifth Conference on Probability and Statistics in Atmospheric Sciences, November 15-18, Las Vegas, Nevada, pp. 196-200.

Reynolds, D. W.; Brown, M. L.; Smith, E. A.; and Vonderhaar, T. H. (1978). Cloud type separation by spectral differencing of image pairs. Mon. Weather Rev., 106, 1214-1218.

Segal, M. and Pielke, R. A. (1981). Numerical model simulation of human biometeorological heat load conditions--summer day case study for the Chesapeake Bay area. J. Appl. Meteor., 20, 735-749.

Segal, M., R. A. Pielke and Y. Mahrer (1984). Evaluation of Surface Sensible Heat Flux Effects on Generation and Modification of Mesoscale Circulations. Proceedings of the Second International Symposium on Nowcasting, European Space Agency, Norrköping, Sweden, 3-7 Sept., 263-269.

Simpson, J. S.; Wescott, N. E.; Clerman, R. J.; and Pielke, R. A. (1980). On cumulus mergers. Arch. Meteor. Geophys., Bioklimatol., Ser. A, 29, 1-40.

Smith, D. L. (1970). The application of digitized radar data to the prediction of summertime convective activity in coastal regions. Preprints, 14th Radar Meteorology Conference, 347-352. American Meteorological Society, Boston, Mass.

Tripoli, G. J. and Cotton, W. R. (1980). A numerical investigation of several factors contributing to the observed variable intensity of deep convection over south Florida. J. Appl. Meteorol., 19, 1037-1063.

Tunick, A. D. (1984). A first-order closure model of the atmospheric boundary layer: comparison with observation and theory. M.S. thesis, Department of Atmospheric Science, Colorado State University, Fort Collins, Colorado 80523. 95 p.

Weaver, J. F. and Kelly, F. P. (1982). A mesoscale, climatologically-based forecast technique for Colorado. AMS Proceedings, Ninth Conference on Weather Forecasting and Analysis, Seattle, Washington, June 28-July 1, 1982, 277-280.

## APPENDIX A

## LIST OF SYMBOLS

| Symbol | Description |
|---|---|
| A | Root extraction term for soil moisture |
| a | Total albedo ($a_z + a_s + a_f$) |
| $a_f$ | Foliage albedo |
| $a_G$ | Total albedo of the ground surface |
| $a_s$ | Soil albedo (function of soil moisture) |
| $a_z$ | Dependence of albedo on zenith angle |
| b | Soil moisture exponent (function of USDA soil textural class) |
| C | Volumetric heat capacity of soil |
| $c_f$ | Non-dimensional transfer coefficient for foliage |
| $c_G$ | Non-dimensional transfer coefficient used to compute wind speed within a plant canopy and for energy fluxes computed beneath the canopy |
| $c_i$ | Dry soil volumetric heat capacity for soil type i |
| $c_p$ | Specific heat at constant pressure for dry air |
| $c_w$ | Heat capacity for water |
| D | Zero-plane displacement height for a plant canopy |
| $D_\eta$ | Diffusivity for soil moisture |
| $D_{\eta_s}$ | Saturation diffusivity for soil moisture |
| $e_s$ | Saturation vapor pressure of air |
| $E_{tr}$ | Transpiration rate per unit area from foliage |
| f | Coriolis parameter |

| Symbol | Description |
|---|---|
| $f'$ | Fraction of potential evaporation from foliage |
| $g$ | Gravitational constant |
| $G$ | Soil heat flux |
| $h$ | Relative humidity of the soil surface |
| $H$ | Sensible heat flux |
| $H_c$ | Mean canopy height |
| $H_s$ | Vertical sensible heat flux within soil |
| $I_1$ | Stability function used to compute friction velocity |
| $I_2$ | Stability function used to compute friction temperature and friction specific humidity |
| $K_H$ | Horizontal exchange coefficient |
| $K_z^m$ | Exchange coefficient for mass used for computing vertical diffusion |
| $K_z^\theta$ | Exchange coefficient for potential temperature and specific humidity used to compute vertical diffusion |
| $K_\eta$ | Hydraulic conductivity |
| $K_{\eta_s}$ | Saturation hydraulic conductivity |
| $k_o$ | von Karman's constant (0.35) |
| $L_c$ | Latent heat of condensation |
| $L_A$ | Leaf area index |
| $L_*$ | Monin-Obukhov mixing length weighted between bare soil and soil overlain by a plant canopy |
| LE | Latent heat flux |
| P | Atmospheric pressure (unscaled) |
| $P_{SEAS}$ | Function of the time of year |
| $P_{oo}$ | Reference atmospheric pressure (usually 1000 mb) |
| q | Atmospheric specific humidity |

| Symbol | Description |
|---|---|
| $q_{af}$ | Specific humidity of the air within a canopy |
| $q_f$ | Foliage specific humidity |
| $q_G$ | Soil surface specific humidity |
| $q_s$ | Saturation specific humidity |
| $q_*$ | Friction specific humidity |
| $q'_*$ | Friction specific humidity weighted between bare soil and soil overlain by a plant canopy |
| r | Depth of the root zone |
| $r_a$ | Resistance of the air |
| $r_c$ | Surface resistance of a canopy to losses of water |
| $r_s$ | Stomatal resistance |
| R | Gas constant for dry air |
| R(z) (3.35) | Root distribution function for vertical profile |
| $R_{Lw}$ | Longwave radiation |
| $R_{sw}$ | Shortwave radiation |
| $R^v_{Lw}$ | Longwave radiation within the canopy |
| $R^v_{sw}$ | Shortwave radiation within the canopy |
| $(R_{sw})_{MAX}$ | Maximum solar radiation for a clear sky |
| $R_v$ | Gas constant for water vapoe |
| t | Time |
| $T_A$ | Free air temperature |
| $T_{af}$ | Air temperature within a plant canopy |
| $T_f$ | Foliage temperature |
| $T_G$ | Temperature of the ground surface |
| $T_s$ | Soil temperature |

| Symbol | Description |
|---|---|
| $u$ | East-West component of velocity |
| $u_a$ | Free air speed just above the canopy |
| $u_{af}$ | Windspeed within a plant canopy |
| $u_g$ | East-West geostrophic wind component |
| $u_*$ | Friction velocity |
| $u_*'$ | Friction velocity weighted between bare soil and soil overlain by a plant canopy |
| $v$ | North-South component of velocity |
| $v_g$ (2.10) | Total geostrophic wind |
| $v_g$ (3.1) | North-South geostrophic wind component |
| $W_a$ | Turbulent atmospheric moisture flux |
| $W_I$ | Maximum interception storage as a depth per unit leaf area |
| $W_L$ | Actual liquid water depth per unit leaf area |
| $W_s$ | Soil moisture flux |
| $w$ | Vertical velocity |
| $x$ | East-West horizontal coordinate |
| $y$ | North-South horizontal coordinate |
| $z$ | Cartesian vertical coordinate |
| $Z$ (3.39) | Zenith angle |
| $z_o$ | Turbulent roughness height |
| $\alpha$ | Constant used to determine the horizontal exchange coefficient |
| $\delta$ | Weighting function |
| $\delta_w$ | Is 0 if condensation is occurring onto a leaf; otherwise it equals 1. |
| $\Delta N_x$ | One grid length in the x direction |
| $\Delta N_y$ | One grid length in the y direction |

| Symbol | Description |
|---|---|
| $\Delta p$ | Depth of convective instability |
| $\overline{\Delta\theta_e}$ | The magnitude of convective instability |
| $\varepsilon_G$ | Ground surface emissivity |
| $\varepsilon_f$ | Foliage emissivity |
| $\eta$ | Soil volumetric moisture |
| $\eta_{ROOT}$ | Minimum soil moisture in the root zone |
| $\eta_s$ | Soil porosity |
| $\eta_{WILT}$ | Permanent wilting soil moisture (15 bar) |
| $\theta$ | Atmospheric potential temperature |
| $\theta_e$ | Equivalent potential temperature |
| $\theta_{es}$ | Saturated potential temperature |
| $\overline{\theta_{es}-\theta_e}$ | Magnitude of moisture deficiency in the layer of convective instability |
| $\theta_*$ | Friction potential temperature weighted between bare soil and soil overlain by a canopy |
| $\lambda$ | Soil thermal conductivity |
| $\pi$ | Scaled pressure (Exner function) |
| $\rho$ | Air density |
| $\rho_s$ | Soil Density |
| $\rho_w$ | Water density |
| $\sigma$ | Stefan-Boltzman constant ($1.38 \times 10^{-12}$ cal/cm$^2$/sec/°C) |
| $\sigma_f$ | Foliage shielding factor |
| $\psi$ | Soil moisture potential (suction) |
| $\psi_G$ | Surface moisture potential |
| $\psi_s$ | Saturated moisture potential |

Subscripts

| | |
|---|---|
| BARE | Bare soil |
| c | Canopy top |
| G | Ground surface |
| h | Canopy height |
| MAX | Maximum |
| $\eta$ | Function of soil moisture |

Superscripts

| | |
|---|---|
| v | Within the canopy |
| c | Canopy top |